

Metal-Polymer Interfaces Studied with Adsorption Microcalorimetry and Photoelectron Spectroscopy

Untersuchungen von Metall-Polymer Grenz-
flächen mittels Adsorptions-Mikrokalorimetrie
und Photoelektronenspektroskopie

Der Naturwissenschaftlichen Fakultät der
Friedrich-Alexander-Universität Erlangen-Nürnberg

zur Erlangung des Doktorgrades Dr. rer. nat.

vorgelegt von
Fabian Bebensee
aus Gelsenkirchen

Als Dissertation genehmigt
durch die Naturwissenschaftliche Fakultät
der Friedrich-Alexander-Universität Erlangen-Nürnberg

Tag der mündlichen Prüfung: 21.06.2010

Vorsitzender der Promotionskommission: Prof. Dr. Eberhard Bänsch
Erstberichterstatter: Prof. Dr. Hans-Peter Steinrück
Zweitberichterstatter: Prof. Dr. Rainer Fink

Abbreviations

\tilde{x}	Reduced Form of x	IMFP	Inelastic Mean Free Path
$ x $	Absolute Value of x	IR	Infra Red
$\langle x \rangle$	Expected Value of x	LEED	Low Energy Electron Diffraction
$\frac{d}{dx}$	Derivation with Respect to x	LEIS	Low Energy Ion Scattering Spectroscopy
$\frac{\partial}{\partial x}$	Partial Derivation with Respect to x	NMR	Nuclear Magnetic Resonance
\times	Cross Product	NEXAFS	Near-Edge X-Ray Absorption Spectroscopy
\cdot	(Dot-)Product	OLED	Organic Light Emitting Diode
exp	Exponential Funktion	P3HT	Poly(3-Hexylthiophene)
ln	Natural Logarithm	PI	Polyimide
Å	Ångström	PMMA	Poly(Methyl Methacrylate)
∞	Infinity	PPV	Poly-(p-Phenylene Vinylene)
°	Arc Degree	PVDF	Polyvinylidene Fluoride
\int	Integral	QCM	Quartz Crystal Microbalance
AES	Auger Electron Spectroscopy	QMS	Quadrupole Mass Spectrometer
AFM	Atomic Force Microscopy	rms	root mean square
DAAD	Deutscher Akademischer Austauschdienst	SIMS	Secondary Ion Mass Spectrometry
DFT	Density Functional Theory	TEM	Transmission Electron Microscopy
ESCA	Electron Spectroscopy for Chemical Analysis	TFT	Thin Film Transistors
HREELS	High Resolution Electron Energy Loss Spectroscopy	TPD	Thermal Programmed Desorption
HRV	Heating Rate Variation	TPS	Thermal Desorption Spectroscopy
HR-XPS	High Resolution XPS	UHV	Ultra High Vacuum
		UPS	Ultraviolet Photoelectron Spectroscopy
		UV	Ultraviolet

XPS	X-Ray Photoelectron Spectroscopy	h	Planck Constant
		k_B	Boltzmann Constant
XSW	X-Ray Standing Wave	R	Gas Constant
$^{\circ}\text{C}$	Degree Celsius	a	Coefficient
eV	Elektronvolt	A	Absorptance
J	Joule	b	Coefficient
K	Kelvin	d	Thickness
m	Meter	D	Diffusion Coefficient
ML	Monolayer	E	Energy
MLE	Monolayer Equivalents	h	Molar Enthalpy
mol	mole	H	Enthalpy
s	Second	I	Intensity
		m	Mass
C	Carbon	n	Parameter
Ca	Calcium	n	Amount of Substance
N	Nitrogen	N	Number of Electrons
O	Oxygen	p	Pressure
S	Sulfur	q	Molar Heat
		Q	Heat
act	Index Activation	R	Reflectivity
ads	Index Adsorption	R	Rate
B	Index Binding	s	Molar Entropy
c	Index Compression	S	Entropy
des	Index Desorption	t	time
exp	Index Experimental	T	Temperatur
f	Index Final State	u	Molar Inner Energy
gas	Index Gas Phase	U	Inner Energy
i	Index Initial State	v	Molar Volume
K	Index Koopmans	v	Velocity
m	Index Measured	V	Volume
m	Index Metal	x	Spatial Coordinate
max	Index Maximum	z	Spatial Coordinate
mo	Index Metal Oxide		
vac	Index Vacuum	β	Crystalline Phase

δ	Energy Correction	μ	Chemical Potential
Δ	Difference Operator	ν	Frequency
θ	Coverage	τ	Residence Time
ϑ	Detection/Emission Angle	Φ	Work Function
λ	Wavelength		
λ	Inelastic Mean Free Path		

Contents

1	Introduction	1
1.1	Enthalpy of Adsorption	3
1.2	Desorption Kinetics	6
1.3	Adsorption-Desorption Equilibria	10
1.4	Calorimetry	13
1.4.1	The Original Wire Calorimeter	14
1.4.2	Beeck's Calorimeter	16
1.4.3	Microcalorimetry on Single Crystals	20
2	Experimental	26
2.1	Calorimetry Apparatus	26
2.1.1	The Calorimeter	26
2.1.2	The Metal Atom Beam Source	29
2.1.3	Calorimeter Calibration	32
2.1.4	Beam Flux Measurements	34
2.1.5	In-situ Determination of the Sticking Probability	34
2.1.6	Relating the Measured Heat to the Adsorption Energy	37
2.2	The X-ray Photoelectron Spectrometer	39
2.2.1	Fundamentals of Photoelectron Spectroscopy	41
2.2.2	Layer Thickness Determination Using XPS	44
2.3	Materials	46
2.3.1	Poly(3-hexylthiophene)	47
2.3.2	CN-MEH-PPV	50
3	Design of a Novel SCAC	53
3.1	The Calorimeter Chamber	53
3.2	The Beam Chopper	55
3.3	The Beam Source	58
3.4	Thermal Design of the Calorimeter	60

4	Metal-Polymer Interfaces	63
5	Calcium Adsorption on Unmodified P3HT	67
5.1	Results	68
5.1.1	Sticking Probability	68
5.1.2	Low-energy Ion Scattering (LEIS)	69
5.1.3	Heats of Adsorption	70
5.1.4	X-ray Photoelectron Spectroscopy	73
5.2	Discussion	74
5.2.1	Growth Model of Ca on P3HT	76
5.2.2	Chemical Reaction between Ca and P3HT	76
5.2.3	Depth Range of Ca Diffusion and Reaction	81
5.2.4	Comparison to Ca Adsorption on Other Polymers	85
5.3	Conclusions	87
6	Calcium Adsorption on Electron-Irradiated P3HT	88
6.1	Results	89
6.1.1	X-ray Photoelectron Spectroscopy	89
6.1.2	Low-energy ion scattering (LEIS)	94
6.1.3	Sticking Probability	95
6.1.4	Heats of Adsorption	98
6.2	Discussion	99
6.3	Conclusions	103
7	Calcium Adsorption on P3HT at Low Temperature	105
7.1	Results and Discussion	107
7.2	Conclusions	114
8	Ca Adsorption on CN-MEH-PPV	115
8.1	Results and Discussion	115
8.1.1	LEIS	115
8.1.2	Heats of Adsorption	117
8.1.3	Sticking Probability	119
8.1.4	X-ray Photoelectron spectroscopy	121
8.2	Conclusions	123

9 Summary and Outlook	124
9.1 Summary	124
9.2 Outlook	127
10 Zusammenfassung und Ausblick	128
10.1 Zusammenfassung	128
10.2 Ausblick	132
11 Danksagung	133
List of Figures	135
Bibliography	137

1 Introduction

The formation of chemical bonds at the surface or at interfaces has been recognized as a fundamentally important process. A detailed understanding of the interface formation is not a purely academic one, aiming solely at a gain in knowledge, but has a tremendous impact on improving working devices in a smart, that is a directed and cost efficient, way. Surface nanocalorimetry was employed in combination with photoelectron spectroscopy to investigate the interface formation between π -conjugated, semiconducting organic molecules and calcium as a low work function metal, which is a technologically very relevant case.

π -Conjugated molecular semiconductors play an increasingly important role in organo electronic devices (OEDs) such as organic light emitting diodes (OLEDs), organic field-effect transistors (OFETs), and organic solar cells.^[1-3] Especially with respect to “printable electronics”, organic semiconductors have a very promising future. The large number of applications, which includes flexible OLED displays (already available in mobile phones, cameras, MP3 players, etc.), e-paper, organic thin-film photovoltaic (OTFPV) devices, and radio frequency identification (RFID) tags, may suffice to illustrate the tremendous economic and ecological importance of this technological sector.^[4]

Interfaces between π -conjugated polymers and low work function metals, such as Li or Ca, occur at the electron-injecting electrodes of organic semiconductor devices, for example OLEDs. The metals are oftentimes evaporated onto the polymer (vapor deposition) at moderately low rates. This route is generally thought to show enhanced diffusion compared with other techniques. Such interfaces are expected to have a high structural and chemical complexity necessitating extensive spectroscopic investigation along with the calorimetric measurements. It is commonly accepted that the properties of interfaces between the organic semiconductors and (metal) electrodes are decisive for the performance of organic electronic devices.

A related field is the study of organic molecular materials, like pentacene, and metals. For certain systems, it has been found that the first monolayer of an adsorbed organic molecules can act as a template and thus influence the structure of the further

layers. In addition, the overlap of wave functions at the metal/organic interface (i.e., the chemical bond) can lead to new electronic states which can modify the charge injection rates.^[5] Therefore, extensive research efforts have been directed towards the understanding of the geometric and electronic structure of the first molecular layers on well-defined metal surfaces. In this context, the strength of the chemical bond between molecule and surface is an important, yet largely unexplored issue. The reasons for this issue being unexplored lie on both the experimental and the theoretical side. On the one hand, conventional experimental techniques cannot be used because of the non-reversible adsorption of the molecules. On the other hand, the methods of theoretical chemistry, especially density functional theory (DFT), are not able to predict accurate adsorption enthalpies with sufficiently small error bars (or other parameters such as surface-adsorbate bond distances) for large organic molecules, mainly because of the size of the systems and fundamental problems in treating van-der-Waals interactions, especially dispersion interactions. For these reasons, such a fundamental parameter as the total strength of the adsorbate-substrate bond is unknown for most large organic molecules. The bond strength also gives insight into the character of the bond (physisorption vs. chemisorption) and how the balance between these contributions depends on the molecular structure and the type of substrate. Up to now, such questions are often discussed on the basis of indirect information such as photoelectron and vibrational spectra, which show adsorption-induced changes of the electronic structure or the vibrational frequencies, as well as adsorbate-substrate bond distances, measured by the X-ray standing wave technique (XSW). In the past years, the group of Dr. Gottfried at the Chair of Physical Chemistry II (Prof. Steinrück) has applied photoelectron spectroscopy and XSW to adsorbed phthalocyanines, porphyrins and other π -conjugated molecules and some of their metal complexes. In agreement with previous and parallel studies on adsorbed π -conjugated molecules, it could be shown that chemisorptive contributions are present, especially in the case of metal complexes, but it is completely unknown how much they contribute to the total binding energy between molecule and surface. At this point, surface nanocalorimetry, in combination with photoelectron spectroscopy, is the only technique that can provide answers.

1.1 Enthalpy of Adsorption

In an adsorption calorimetry experiment, the temperature change of a sample caused by adsorption of a pulse of molecules or atoms is recorded as a function of coverage, i.e., for a number of successive pulses. The fundamental thermodynamics inherent to this experiment are easiest to capture by considering the effect of a single pulse and its impact on the sample surface.

It is very helpful to notice that several quantities may be considered constant for the duration of an experimental run. Among these are the area on the sample where adsorption takes place and the sample temperature is restored via a thermal reservoir just before a new pulse of atoms reaches the surface. The gas to be adsorbed, or adsorptive, is generally treated like an ideal gas, a system for which the enthalpy is well known. In the experiment, a transition from the gaseous state (index “gas”) to the adsorbed state (index “ads”) occurs. The respective enthalpies can be expressed as:

$$H_{\text{gas}} = U_{\text{gas}} + p_{\text{gas}} \cdot V_{\text{gas}} = U_{\text{gas}} + n \cdot R \cdot T \iff h_{\text{gas}} = u_{\text{gas}} + R \cdot T \quad (1.1)$$

$$H_{\text{ads}} = U_{\text{ads}} + \underbrace{p_{\text{ads}} \cdot V_{\text{ads}}}_{\approx 0} \iff h_{\text{ads}} = u_{\text{ads}} \quad (1.2)$$

where H_{gas} is the enthalpy of the gas, U_{gas} its internal energy, p_{gas} the pressure, V_{gas} the volume occupied, and n the number of moles. H_{ads} , U_{ads} , p_{ads} and V_{ads} are the respective quantities in the adsorbed phase. Here and throughout this work, upper case letters refer to extensive and lower case letters to molar quantities. The term $p_{\text{ads}} \cdot V_{\text{ads}}$ drops out of Equation (1.2), because the volume in the adsorbed phase it is negligibly small. It is important to keep in mind that u_{ads} includes the internal energy of the atom on the surface itself as well as the interaction energy between the atom and the substrate (adsorbate binding energy) and potentially a change in the free energy of the surface which might be altered by the adsorption of a species. The change in molar enthalpy for the phase transition is simply the difference between the two molar enthalpies given above:

$$\Delta h = (h_{\text{gas}} - h_{\text{ads}}) = \underbrace{u_{\text{gas}} - u_{\text{ads}}}_{=q_{\text{ads}}} + \underbrace{R \cdot T}_{=q_{\text{c}}} \quad (1.3)$$

q_{ads} denotes the so-called differential heat of adsorption, the sought after quantity in calorimetric experiments. The differential heat of adsorption is the change in

internal energy during the adsorption process along a path on which no work is performed. q_c is the heat of compression, stemming from the transformation of the finite volume in the gas phase into the approximately zero-volume adsorbate layer. In the above equation, q_c is calculated assuming that all atoms from the pulse adsorb on the surface. This helps to keep the complexity as low as possible, but can easily be corrected for by multiplying the term with the fraction of molecules/atoms that do indeed adsorb, the so-called sticking coefficient.

For the relationship between the heat of adsorption $q_{\text{ads}}(\theta)$ and the heat detected by the calorimeter $q_{\text{m}}(\theta)$, which may both depend on the coverage, one finds:

$$q_{\text{ads}}(\theta) = q_{\text{m}}(\theta) - q_c(\theta) \quad (1.4)$$

where θ is the coverage. Up to now, the heat of adsorption was always expressed as the differential heat of adsorption, i.e., the internal energy change of the adsorbed species due to adsorption of an infinitesimal small amount of gas. This quantity is very similar with and easily comparable to isosteric heats obtained from adsorption isosteres discussed below.

Another interesting quantity is the integral heat of adsorption, which accounts for the total amount of energy released by adsorption from zero coverage to a given coverage θ and thus provides an average heat of adsorption up to this coverage. Integral (Δh_{int}) and differential (Δh) heat of adsorption are mathematically related via the following expression:

$$\Delta h_{\text{int}} = \frac{\int_0^\theta \Delta h d\theta'}{\int_0^\theta d\theta'} \quad (1.5)$$

Usually, the term “heat of adsorption” (Q_{ads}) is used synonymously with “enthalpy of adsorption”. However, they are defined such that their signs are opposite and their mathematical relationship therefore reads:

$$-\Delta H_{\text{ads}} = Q_{\text{ads}} \quad (1.6)$$

A number of effects may contribute to the heat adsorption, rendering it a truly complex quantity: the energy of the surface bond, changes in degrees of freedom of the atoms/molecules, the energy of interaction between the adspecies, surface relaxations or rearrangements, as well as changes in the electronic structure of the adsorbate. Due to this complexity, the combination of heat of adsorption measurements

with other experimental techniques is often highly desirable, if not mandatory.^[6] Determination of the heat of chemisorption from the (integral) heat of adsorption is not as straight forward as it may seem: only the average of the binding energies of all different sites weighted with their respective relative coverage is accessible. This is particularly problematic for polycrystalline samples, where a variety of adsorption sites is intrinsically present. Nevertheless, also single crystals do not provide energetically completely homogeneous surfaces. Therefore, the integral heat of adsorption is of little significance on its own.^[7,8] Choosing favorable conditions and applying complementary techniques may lead in numerous cases to the desired gain in knowledge of the system under investigation. Within this work, high-resolution X-ray photoelectron spectroscopy (HR-XPS) is used as the complementary technique providing insight into the nature and relative coverage of different adsorption sites. If coverage regimes are found, where only one specific site is significantly populated, the corresponding heat of adsorption reflects the heat of chemisorption of this site. Even in this idealized case, adsorbate-adsorbate interactions may lead to complications in the analysis of such systems via coverage-dependent heat of adsorption values.

Despite experimental difficulties in gathering adsorption enthalpies, they constitute an important and thus sought after thermodynamic quantity in the study of gas phase/solid interactions. Adsorption enthalpies are especially useful in the field of heterogeneous catalysis, where they provide a glimpse at the thermodynamics of interesting systems. In this way, they may aid in the design of improved catalysts.^[9-11] Furthermore, the heat of adsorption represents an experimentally accessible observable, while remaining a fundamental result of theoretical considerations.^[6,12,13] In this sense, accurate calorimetric measurements may be used to benchmark calculated adsorption energies from various computational methods.^[14]

Essentially, three different approaches for the experimental determination of enthalpies of adsorption exist: evaluation of adsorption equilibria, e.g., adsorption isosteres, desorption kinetics, e.g., temperature programmed desorption (TPD), and calorimetric measurements. The three routes have distinct advantages and disadvantages depending on the particular system under investigation. All of them certainly have their limitations with respect to their scope of application. A further complication arises from the fact that the data obtained using different techniques are not directly comparable “as measured”, as Stuckless et al. have pointed out.^[11] In the following, the three methods for determining enthalpies of adsorption shall

be introduced. The discussion of these methods will be completed by a historical overview over the most important developments in adsorption microcalorimetry, e.g., calorimetric measurements on small surface area samples.

1.2 Desorption Kinetics

Measurements of desorption kinetics allow, as mentioned above, the determination of adsorption enthalpies. The most suitable experimental procedure, namely temperature-programmed desorption (TPD) or thermal desorption spectroscopy (TDS), was introduced by I. Langmuir.^[15] The technique became widely used in surface science and catalysis^[16-21] as it grants experimentally undemanding access to such important parameters like activation energies and frequency factors of desorption. With the help of an appropriate kinetic model, one can calculate frequency factors and desorption activation energies E_{des} , which are closely related to adsorption entropies and enthalpies, respectively.

The adsorption enthalpy describes the energetic difference between the adsorbed atom or molecule to the case of the atom or molecule being in the gas phase including all effects based on phase changes, changes in the free energy of the surface or adsorbate system, respectively, and the energy released due to bonding of the atom/molecule on the surface. The adsorbate binding energy, in contrast, only accounts for the difference in potential energy, i.e., the energy stored in the bond formed as the result of the adsorption process. They may still be related to one another, such that results from techniques yielding desorption or adsorption energies may well be compared with those from measurements of heats of adsorption, most prominently isosteric heats of adsorption. As theoretical calculations usually yield adsorbate binding energies rather than heats of adsorption, the relationship between these two quantities effectively establishes the link between calorimetry experiments and theory.

In a TPD experiment, the adsorbate precovered sample is heated with a defined heating rate $\beta = dT/dt$ in a temperature range including the desorption temperature. Simultaneously, the mass spectrometer signal, which is proportional to the partial pressures of the desorbing species, is recorded. Plots of the measured mass spectrometer signal versus temperature yield the thermal desorption spectrum (see Figure 1.1 for a set of sample TPD spectra). Frequently, the Polanyi-Wigner equation^[23] is

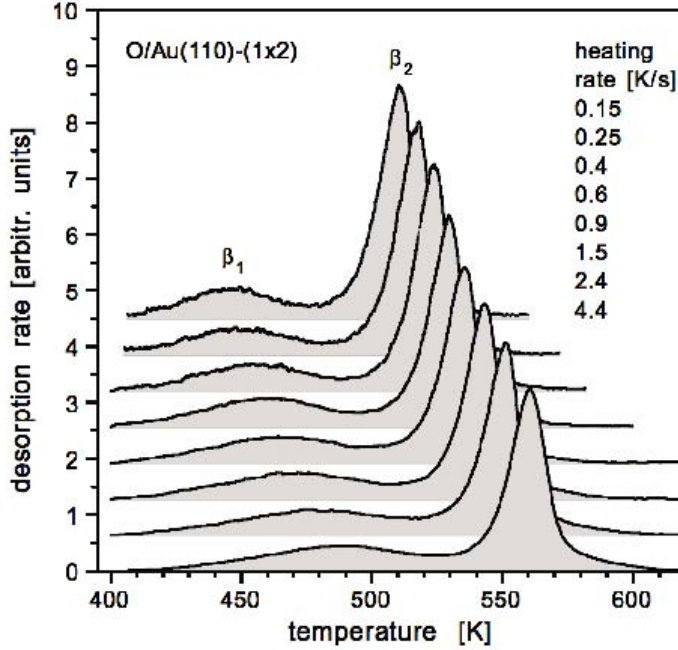


Figure 1.1: Set of exemplary TPD spectra of oxygen on Au(110)-(1 × 2) with initial coverages of 1.45 ML for different heating rates β (from reference [22]).

employed as the basis for the evaluation of TPD experiments:

$$R_{\text{des}} = -\frac{d\theta}{dt} = -\frac{d\theta}{dT} \underbrace{\frac{dT}{dt}}_{=\beta} = -\frac{d\theta}{dT} \cdot \beta = \nu_n \cdot \theta^n \exp\left(-\frac{E_{\text{des}}}{R \cdot T}\right) \quad (1.7)$$

Here, R_{des} denotes the rate of desorption, θ the temperature dependent coverage, t the time, T the temperature, β the heating rate, ν_n the frequency factor of desorption, E_{des} the desorption activation energy and R the universal gas constant.

Among a number of different methods for the extraction of the activation parameters, most importantly E_{des} , only the method commonly referred to as “heating rate variation” (HRV) will be discussed below. For further information and a critical comparison of the different methods, the reader is kindly referred to the article by de Jong and coworkers. [24]

Using the HRV formalism, the temperature T_{max} at which the highest desorption rate is observed, as a function of the heating rate β allows the determination of E_{des} and ν_n , in cases, where the desorption order n is known. Typically, TPD spectra display the mass spectrometer signal at a certain mass. Under favorable conditions, this signal is proportional to the desorption rate $-d\theta/dT$ as a function of temperature.

The corresponding form of the Polanyi-Wigner equation reads:

$$R_{\text{des}}^{\text{exp}} = -\frac{d\theta}{dT} = \frac{\nu_n}{\beta} \cdot \theta^n \exp\left(-\frac{E_{\text{des}}}{R \cdot T}\right) \quad (1.8)$$

In this equation, $R_{\text{des}}^{\text{exp}}$ denotes the rate of desorption with respect to the temperature. At T_{max} , the temperature at which the desorption rate is the highest, Equation (1.8) must obviously exhibit a local maximum. The mathematical translation of this is simply that differentiation with respect to the temperature T yields an expression that must be equal to zero:

$$\begin{aligned} \frac{dR_{\text{des}}^{\text{exp}}}{dT} &= \frac{d}{dT} \left(\frac{\nu_n}{\beta} \cdot \theta^n \cdot \exp\left(-\frac{E_{\text{des}}}{R \cdot T}\right) \right) \Big|_{T=T_{\text{max}}} \\ &= \frac{\nu_n}{\beta} \cdot \theta^n \cdot \frac{E_{\text{des}}}{R \cdot T_{\text{max}}^2} \cdot \exp\left(-\frac{E_{\text{des}}}{R \cdot T_{\text{max}}}\right) \\ &\quad + \exp\left(-\frac{E_{\text{des}}}{R \cdot T_{\text{max}}}\right) \cdot \frac{\nu_n}{\beta} \cdot n \cdot \theta^{n-1} \frac{d\theta}{dT} \\ &= 0 \end{aligned} \quad (1.9)$$

and hence

$$\frac{E_{\text{des}}}{R \cdot T_{\text{max}}^2} = \frac{\nu_n}{\beta} \cdot n \cdot \theta^{n-1} \cdot \exp\left(-\frac{E_{\text{des}}}{R \cdot T_{\text{max}}}\right) \quad (1.10)$$

Rearranging and taking the natural logarithm leads to the following form of Equation (1.10), with the tilde expressing that the respective quantity is to be divided by an appropriate quantity so as to allow application of the logarithm:

$$\ln\left(\frac{\tilde{T}_{\text{max}}^2}{\tilde{\beta}}\right) = \frac{E_{\text{des}}}{R \cdot T_{\text{max}}} + \ln\left(\frac{\tilde{E}_{\text{des}}}{\tilde{\nu}_n \cdot \tilde{R} \cdot n}\right) + (1-n) \cdot \ln(\tilde{\theta}_{\text{max}}) \quad (1.11)$$

Plots of $\ln\left(\tilde{T}_{\text{max}}^2/\tilde{\beta}\right)$ versus $1/T_{\text{max}}$ are linear for cases in which the desorption behavior is adequately described by the Polanyi-Wigner equation and the activation parameters are constant. In these cases, the desorption activation energy and the frequency factor are readily available from the slope and the intercept with the ordinate, respectively. This method is particularly convenient in cases with the desorption order n equal to one (first order desorption), because then the coverage dependent term on the right hand side of Equation (1.11) vanishes. One of the drawbacks of this analysis method is that a number of TPD spectra must be recorded for the same initial coverage but varying heating rates β . Thus, it is rather

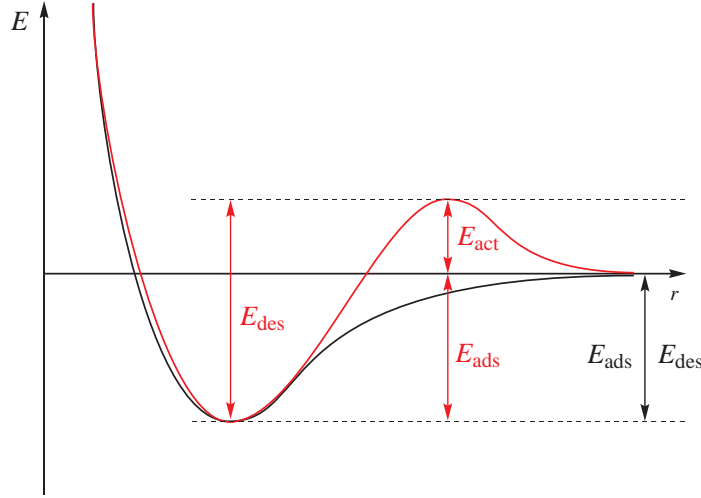


Figure 1.2: Potential energy curves for activated (red curve) and non-activated (black curve) desorption. Here, E denotes the potential energy, E_{des} the desorption energy, E_{act} the energetic barrier in activated desorption, and E_{ads} the adsorption energy.

uneconomical with respect to the data material that needs to be collected.

A method for estimating the desorption energies from individual TPD traces and thus circumventing the aforementioned problem, was proposed by Redhead. ^[25] One can simply solve Equation (1.11) for E_{des} assuming first order desorption:

$$E_{\text{des}} = R \cdot T_{\text{max}} \cdot \left[\ln \left(\frac{\nu_1 \cdot T_{\text{max}}}{\beta} \right) - \ln \left(\frac{E_{\text{des}}}{R \cdot T_{\text{max}}} \right) \right] \quad (1.12)$$

Redhead demonstrates that variation of the ratio ν_1/β in the range 10^8 K^{-1} to 10^{13} K^{-1} leads only to small errors ($<1.5\%$) and that the approximation

$$\ln (E_{\text{des}}/R \cdot T_{\text{max}}) \approx 3.64 \quad (1.13)$$

works satisfactorily. This leads finally to the Redhead equation, which relates the desorption energy directly to the temperature at which the maximum desorption rate is observed:

$$E_{\text{des}} = R \cdot T_{\text{max}} \cdot \left[\ln \left(\frac{\nu_i \cdot T_{\text{max}}}{\beta} \right) - 3.64 \right] \quad (1.14)$$

In this equation ν_1 is often assumed to be on the order of 10^{13} s^{-1} . Consequently, for reasonable heating rates β , the ratio ν_1/β falls within the considered range.

Provided that the desorption process is non-activated or the activation barrier is small, the desorption energy is equal or sufficiently close to the adsorption energy,

which is the quantity of primary interest in this work. A schematic presentation of the relationships between desorption energy E_{des} , adsorption energy E_{ads} and adsorption activation energy E_{act} is presented in Figure 1.2.

However, one fundamental problem is inherent to desorption based techniques with respect to the determination of the adsorption energy: the system must be thermally robust, i.e., no alteration of the adsorbate system (except desorption) may be caused by heating the sample up to the desorption temperature.

1.3 Adsorption-Desorption Equilibria

The Clausius-Clapeyron equation, which describes the temperature-dependence of the adsorption/desorption equilibrium pressure, defines different isothermal heats of adsorption depending on the parameter which is kept constant. Keeping the coverage θ , i.e., the number of adsorption sites within a monolayer divided by the number of filled adsorption sites, constant is experimentally convenient. The differential equilibrium conditions for such a situation reads:

$$d\mu_{\text{gas}} = d\mu_{\text{ads}} \quad (1.15)$$

with the chemical potential μ and the indices gas and ads referring to the gas phase and the condensed phase, respectively. As the chemical potential in the gas phase depends on temperature T and pressure p , while the chemical potential of the condensed phase additionally depends on the coverage θ , the total differential reads:

$$\left(\frac{\partial\mu_{\text{gas}}}{\partial T}\right)_p \cdot dT + \left(\frac{\partial\mu_{\text{gas}}}{\partial p}\right)_T \cdot dp = \left(\frac{\partial\mu_{\text{ads}}}{\partial T}\right)_{p,\theta} \cdot dT + \left(\frac{\partial\mu_{\text{ads}}}{\partial p}\right)_{T,\theta} \cdot dp + \left(\frac{\partial\mu_{\text{ads}}}{\partial\theta}\right)_{p,T} \cdot d\theta \quad (1.16)$$

In the above equation, one assumes that the number of adsorption sites in one monolayer does not change. Taking into account that under isosteric conditions the last term in Equation (1.11) vanishes and substituting the appropriate molar entropy s and partial molar volume v for the partial differentials, one arrives at:

$$-s_{\text{gas}} \cdot dT + v_{\text{gas}} \cdot dp = -s_{\text{ads}} \cdot dT + v_{\text{ads}} \cdot dp \quad (1.17)$$

wich can be written as

$$\left(\frac{dp}{dT}\right)_\theta = \frac{s_{\text{gas}} - s_{\text{ads}}}{v_{\text{gas}} - v_{\text{ads}}} = \frac{h_{\text{gas}} - h_{\text{ads}}}{T \cdot (v_{\text{gas}} - v_{\text{ads}})} \quad (1.18)$$

Exploiting that the molar volume of the gas phase is considerably larger than that of the condensed phase and using furthermore the ideal gas law to express the molar volume of the gas phase, Equation (1.18) yields:

$$\left(\frac{dp}{dT}\right)_\theta = \frac{p \cdot \overbrace{(h_{\text{gas}} - h_{\text{ads}})}^{=\Delta_{\text{ads}}h}}{\text{R} \cdot T^2} = -\frac{p \cdot \Delta_{\text{ads}}h}{\text{R} \cdot T^2} \quad (1.19)$$

Rearranging this equation finally leads to an expression that readily gives access to the molar heat of adsorption $\Delta_{\text{ads}}h$:

$$\left(\frac{\partial \ln(p)}{\partial 1/T}\right)_\theta = -\frac{\Delta_{\text{ads}}h}{\text{R}} = \frac{q_{\text{st}}}{\text{R}} \quad (1.20)$$

Equation (1.20) describes adsorption isosteres and thus defines the isosteric heat of adsorption, q_{st} . This is related to the molar adsorption enthalpy via:

$$\Delta_{\text{ads}}h \equiv \left(\frac{\partial \Delta_{\text{ads}}H}{\partial n}\right)_{p,T} = h_{\text{ads}} - h_{\text{gas}} \equiv \left(\frac{\partial H_{\text{ads}}}{\partial n}\right)_{p,T} - \left(\frac{\partial H_{\text{gas}}}{\partial n}\right)_{p,T} = -q_{\text{st}} \quad (1.21)$$

In this equation, h_{gas} and h_{ads} stand for the partial molar enthalpies of the gas phase and the adsorbed phase, respectively, and $\Delta_{\text{ads}}h = h_{\text{ads}} - h_{\text{gas}}$ for the molar adsorption enthalpy.

One can utilize Equation (1.20) to determine q_{st} as a function of coverage from experimental data. A typical experiment for the determination of the isosteric heat of adsorption proceeds as follows: while keeping the partial pressure constant, the sample temperature is slowly varied and the equilibrium coverages are constantly monitored. The equilibrium coverages can be extracted from continuously measuring the work function change, for example. Collecting data for various equilibrium pressures results in data triplets (p, T, θ) , which can be used to create plots of $\ln(p)$ versus $1/T$ at a fixed coverage θ . Making use of Equation (1.20) readily gives q_{st} from this plot for this coverage.

It is desirable and in many cases even mandatory to determine the same quantity using different approaches in order to fully characterize a system. A comparison of data obtained from TPD experiments and adsorption isosteres requires a link between the two respectively measured quantities, i.e., between the adsorbate bind-

ing energy E_0 (TPD) and the isosteric heat of adsorption q_{st} (adsorption isosteres). This relation between q_{st} and the adsorbate binding energy E_0 can be derived from equipartition considerations. E_0 represents nothing else, but the adsorption energy E_{ads} per mol (see Figure 1.2), which is identical to the desorption activation energy E_{des} for non-activated desorption. Thus, the relation between the E_0 and q_{st} is the key in order to compare isosteric heats with results of TPD experiments. One finds that two limiting cases need to be distinguished for this relation: mobile adsorption and localized adsorption. For a monatomic ideal gas, the enthalpy in the gas phase H_{gas} is:

$$H_{\text{gas}} = U_{\text{gas}} + \underbrace{p \cdot V_{\text{gas}}}_{=n \cdot R \cdot T} = \frac{5}{2} \cdot R \cdot T \iff h_{\text{gas}} = \frac{5}{2} \cdot R \cdot T \quad (1.22)$$

Considering mobile adsorption, the adsorbed phase retains two degrees of translational freedom and one vibrational degree of freedom perpendicular to the surface. Thus, the enthalpy of the condensed phase h_{ads} amounts to:

$$h_{\text{ads}} = u_{\text{ads}} = 2 \cdot R \cdot T - |E_0| \quad (1.23)$$

Using Equation (1.21), one finds for mobile adsorption of a monatomic gas

$$q_{\text{st}} = h_{\text{gas}} - h_{\text{ads}} = \frac{1}{2} \cdot R \cdot T + |E_0| \quad (1.24)$$

Similarly, one arrives at:

$$q_{\text{st}} = -\frac{1}{2} \cdot R \cdot T + |E_0| \quad \text{for localized adsorption of a monatomic gas} \quad (1.25)$$

$$q_{\text{st}} = |E_0| \quad \text{for mobile adsorption of a diatomic molecule} \quad (1.26)$$

$$q_{\text{st}} = -\frac{3}{2} \cdot R \cdot T + |E_0| \quad \text{for localized adsorption of a diatomic molecule} \quad (1.27)$$

Obviously, q_{st} is always reasonably close to the adsorbate binding energy $|E_0|$ (in the case of non-activated desorption: E_{des} per mol) under the assumption that all adsorbate-substrate vibrations are fully excited.

Instead of keeping the partial pressure constant and varying the temperature, one may as well fix the temperature and vary the partial pressure. In this way, adsorption isotherms are obtained, which may be evaluated to yield the isosteric heat of adsorption, too. In any case, one problem is common in deducing heats of adsorption from adsorption-desorption equilibria and desorption kinetic measurements: both rely on the adsorption being fully reversible and thus are not applicable for a huge

number of systems. ^[26,27]

1.4 Calorimetry

Calorimetry was introduced by J. Black, who observed that melting ice takes up heat without changing its temperature in 1761. ^[28] This observation laid the foundation of thermodynamics, a very important discipline within chemistry.

The word calorimetry stems from the Latin expression “calor” meaning heat and the Greek word for measure, “metron”, readily defining its task: measuring the heat of chemical reactions or physical changes (e.g., phase changes). Within this work, emphasis is put on the heat released as a species is adsorbed onto a solid substrate and its subsequent reactions, the heat of adsorption/reaction. The experimental implementation appears rather simple: the rise in temperature as a result of dosing a reagent (i.e., a gas) is measured. Due to its nature, calorimetric determination of the heats of adsorption does not require any model or theoretical framework to arrive at the heat of adsorption, which is directly measured. This, furthermore, lends calorimetry the advantage over the two other principal ways to measure heats of adsorption discussed above: it is applicable for reversible adsorption as well as for irreversible adsorption, as it directly measures the heat released upon adsorption and does not rely on desorption. Another advantage over the other two methods is that calorimetric experiments are conducted at a fixed temperature, a condition that is much easier to control compared to defined changes in temperature needed for the other methods. In addition to the relative experimental simplicity, the state of the adsorbate is always well defined in such experiments, in contrast to TPD experiments, for example, where the adsorbate structure is disturbed in the course of the experiment.

Despite these profound advantages, adsorption calorimetry has only recently entered the field of surface science, where low specific surface samples are considered – calorimetry on high surface samples, i.e., powders, is well established. The explanation for this fact is twofold: firstly, ultrathin single crystals as adsorbents with low heat capacities were only accessible recently ^[29–32] and secondly, the early calorimeters (wire or Beeck’s type calorimeter) were only suitable for cases, where the heat of adsorption was deposited sufficiently fast in the sample. ^[6,11,32] The problem of slow deposition of heat in an adsorption experiment is essentially a problem with low sticking probability of the adsorptive: in such cases, it takes a large amount

of time after admittance of the gas dose, until the adsorption equilibrium is established. Besides the very general problem that this renders the observed temperature rise void of meaning with respect to the total amount of heat deposited, it may well be that the heat deposited may be removed by only transiently adsorbed atoms or molecules.

The historical development of adsorption calorimetry on low surface area samples shall be briefly outlined below.

1.4.1 The Original Wire Calorimeter

To make full use of his theoretical treatments of the heat of adsorption on homogeneous surfaces and the influence of adparticles surrounding a filled adsorption site thereon, J. K. Roberts was in need of experimental data to compare his expressions derived for mobile and localized adsorption.^[6,33,34] To this end, he devised a calorimeter that allowed the determination of the heat of adsorption created by the adsorption of incremental gas doses on thin metal wires, which simultaneously served as the adsorbent and resistive thermometer. The wires could be flashed to high temperatures (up to 2000 K) allowing the study of adsorption starting from a bare surface.

Problems encountered with this type of experiment include a low surface to volume ratio of the wires used as the sensing element: it was 28 cm long and 6.6 μm in diameter, yielding a surface area of 0.58 cm^2 . Its heat capacity of 2.5 $\text{J}\cdot\text{K}^{-1}$ was large compared to the relatively low number of sites for adsorption the wire provided. Also, the use of a polycrystalline adsorbent encompasses the disadvantages that it remains essentially unknown what specific sites contribute to what extent to the measured heat of adsorption. It also provides only a rather small coverage resolution.^[6] Nevertheless, the results Roberts achieved for the adsorption of hydrogen on tungsten yielded results comparing very well against measurements undertaken some forty years later.^[6,35]

In 1959, P. Kisliuk revived the calorimetric experiments pioneered by Roberts. The use of ribbons instead of wires led to a significant increase in the surface-to-volume ratio and thus to an increase in sensitivity. He also used a second ribbon as a source for dosing nitrogen via flash desorption. Overall, these improvements enabled him to collect a higher number of data points of the heat of adsorption curve. At the same time, he was able to lower the level of contamination.^[36] However, due to the polycrystalline nature of the ribbon, the measured heat of adsorption values

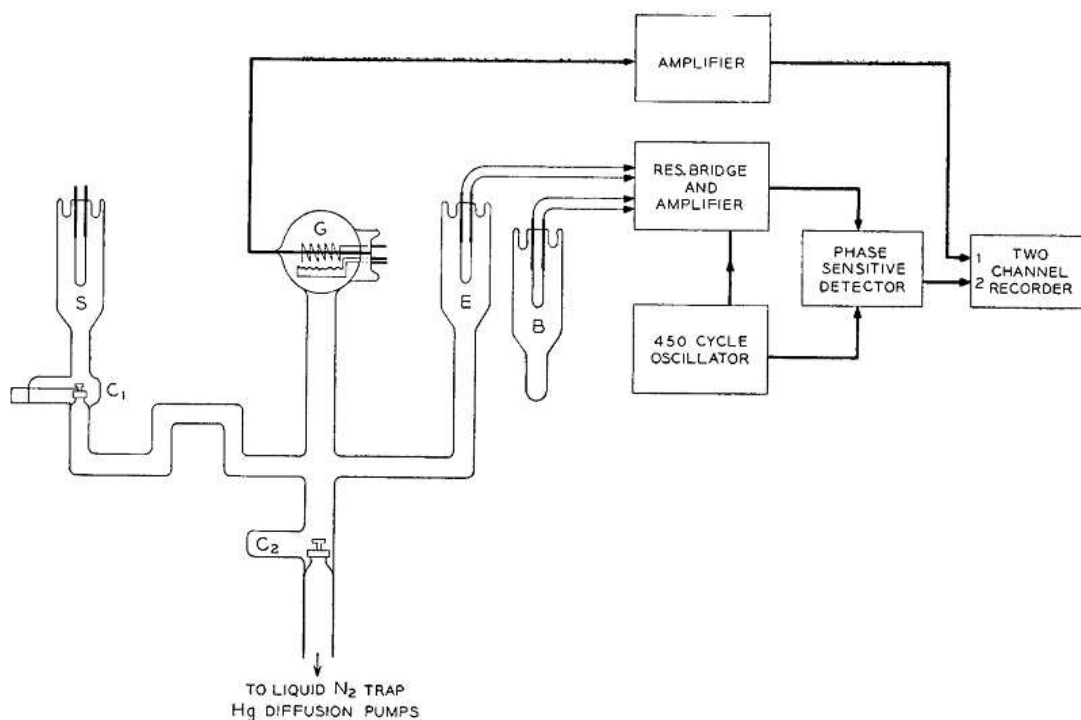


Figure 1.3: Simplified sketch of the apparatus used by Kisliuk (from [36])

deviated between different ribbons considerably at high coverages. This fact seeded doubts about the validity of the low coverage data as well and inspired the idea of using single crystals (i.e., single crystal ribbons) to solve the problem of low reproducibility. The measurements on such ribbons, as proposed by Kisliuk, were never published. [6] The first measurements on a single crystal surface were reported 27 years later.

Several refinements of the general approach were introduced later on without leading to a breakthrough. Calorimetrically well studied were the H_2/W [33,37-40] and N_2/W [36,39,41] systems, but data were also published for O_2/W [33,34] and H_2 and N_2 on different metals (see References [6] and [42] for more references).

Although quite impressive results could be obtained, the limitations of such experiments were quite obvious:

- The choice of the adsorbent is limited to metals which can be annealed without loss of their structural stability or similar disadvantageous side effects of annealing, for example segregation of impurities to the surface.
- The requirement of fast heat deposition limits calorimetry to systems with a

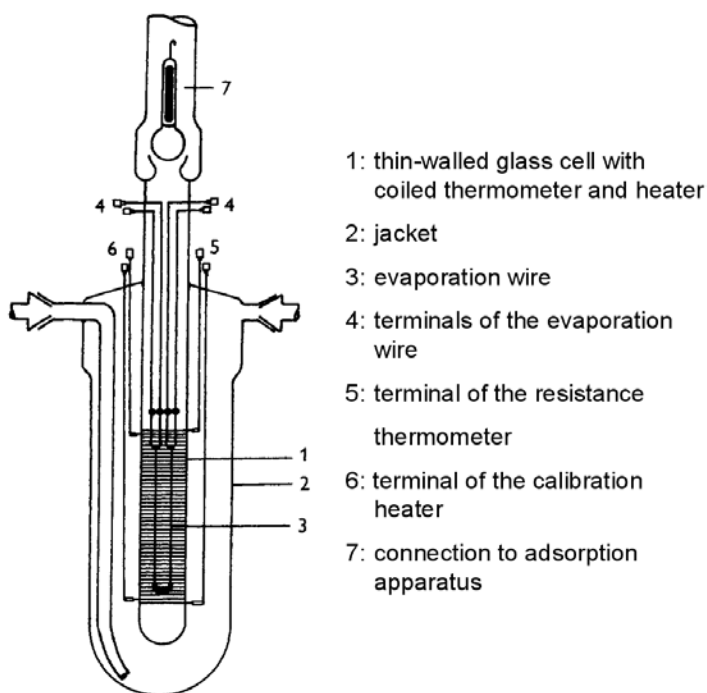


Figure 1.4: Schematic sketch of a Beeck-type calorimeter (from Reference [6])

high sticking probability, where the dosed gas is adsorbed (almost) completely.

- While extremely thin wires were advantageous in the sense that their high resistance allowed for a higher sensitivity, they entailed disadvantages in their structural properties, especially when heated or exposed to gas.
- Determination of the absolute surface coverage of the wires suffered from uncertain assumptions (nature of planes exposed, roughness, surface area occupied by single adparticle, etc.).
- Due to the small number of individually built experiments, comparability of results is further limited (beyond limitations set by the adsorbent).

1.4.2 Beeck's Calorimeter

In the later 1930s, interest in thin films of transition metals and their catalytic qualities was sparked by Leypunski, ^[43,44] de Boer ^[45] and Beeck. ^[46,47] As the elucidation of the reaction mechanisms called for heat of adsorption measurements, O. Beeck devised a calorimeter capable of determining the heat of adsorption on such thin films in 1940. It was not until 1945, that a brief description and first results were

published.^[47] The calorimeter, a sketch is shown in Figure 1.4, consisted of a wire (hairpin-shaped) in a thin-walled glass tube. A resistance thermometer was wound around the glass capsule and the whole assembly was mounted in a glass jacket that could be evacuated and immersed in a liquid (ice water or liquid air) to stabilize the temperature of the calorimeter. In an experiment, a thin film (typically film thicknesses on the order of 10 nm were used by Wedler^[48–53]) was evaporated from the metal wire on the inside of the glass capsule and pulses of gases were admitted. The temperature change as evidenced from the change in resistance was then recorded and evaluated. For the data evaluation, the weight of the metal film after evaporation (from the weight of the wire before and after the experiment) and the heat capacity of the calorimeter had to be known. The latter was calculated from the masses and heat capacities of the individual components. As an alternative way to relate the data from the calorimeter with the amount of heat deposited during an experiment, an electric heater could be used for calibration.

This method, first introduced by Kisliuk for the original wire calorimeters, was already incorporated into the experimental setup shown in Figure 1.4. Its accuracy was initially viewed rather critically. However, Kisliuk's results were confirmed later and Wedler used this method of calibration very successfully.^[54,55]

Even from this brief description, the most critical points for this type of calorimeter are obvious^[6]:

- The walls of the glass capsule must be thin in order to guarantee ready and complete transfer of heat generated by adsorption/reaction to the detector.
- The walls must exhibit a uniform thickness so that the response of the systems remains comparable no matter on which part of the wall the adsorption occurs.
- The design (shape and dimension) of the vessel must ensure that each the gas admitted in every dose can reach the whole film, e.g., pressure gradients must be avoided.

Besides these issues, the temperature stability^[49,54,56–64], the morphology of the evaporated thin films^[49,50,60,65–75], the calibration of the calorimeter^[33,38,54,55,65,76] and the data evaluation methods^[57,60,61,65,77,78] were crucial points and discussed to great extent.

This original design by Beeck was improved and used until long after the death of its inventor in 1951. The most notable changes were introduced by G. Wedler and

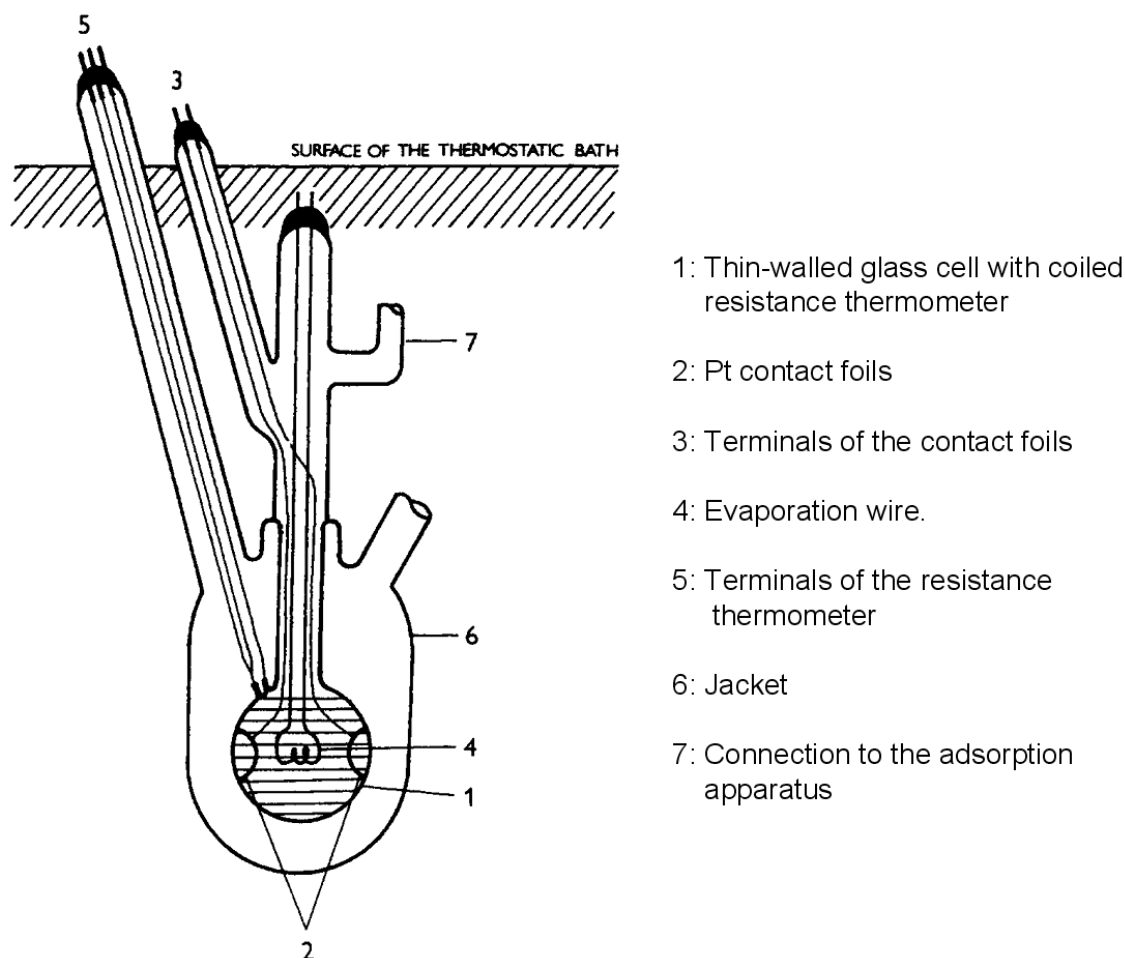


Figure 1.5: Wedler's calorimeter (from Reference [6])

S. Černý :

Wedler, who held the Chair of Physical Chemistry II at the University Erlangen-Nürnberg from 1966 until 1995, employed a spherical vessel (shown in Figure 1.5) in contrast to the cylindrical shape favored by Beek. This design minimized deviation in the film thickness. Another improvement was made by reducing the influence of electromagnetic fields using induction-free, twisted tungsten wires as a resistance thermometer and for heating. With this setup, Wedler and his coworkers studied the adsorption of gases (H_2 , CO , CO_2 , H_2O) on various transition metals such as iron, nickel, and titanium. [48–50, 52, 53, 58, 61, 62, 67, 77, 79–83]

Černý extended the use of the Beek-type calorimeter to the adsorption of light hydrocarbons on platinum and molybdenum. [86–88] His group in Prague also investigated the adsorption of hydrogen, oxygen, carbon monoxide and light hydrocar-

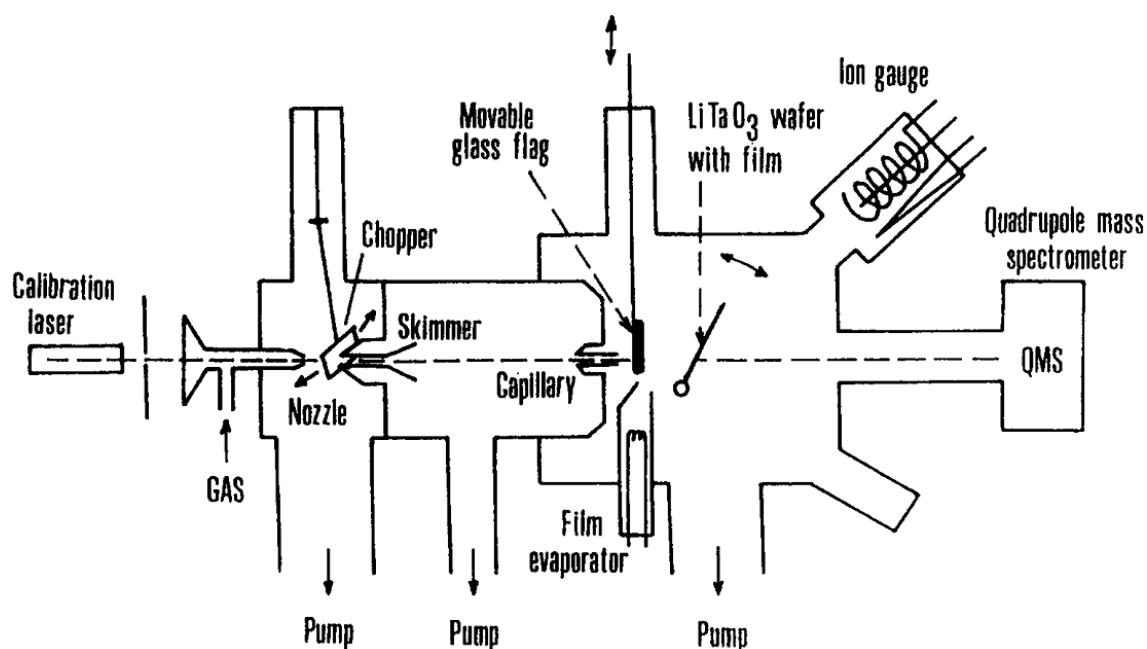


Figure 1.6: Adsorption calorimeter for polycrystalline films employing a pyroelectric temperature sensor. ^[84,85]

bons on lanthanides. ^[45,89–95] A very important contribution from this group was the introduction of a pyroelectric heat detector. ^[84,85] As this detector is sensitive to temperature changes, it easily allowed to measure the heat of adsorption from a pulsed molecular or atomic beam. This is a huge improvement over the previously described approaches in that it allows for collection of a comparably large number of data points within a reasonable time. A schematic sketch of an apparatus employing this type of detector is shown in Figure 1.6. The same type of detector was used many years after its introduction by Černý in single crystal calorimetry. Hence, Černý must be viewed as a pioneer in this field, too. Great progress was achieved

Time Period	Number of Publications
1945 — 1950	3
1951 — 1960	7
1961 — 1970	10
1971 — 1980	18
1981 — 1990	11
1991 — 1995	5

Table 1.1: Number of original publications including experimental results from polycrystalline film calorimeters (from [6])

applying these refined calorimetry experiments: higher reproducibility, precision and accuracy led to relevant new insights and calorimetry was established as a valuable tool. However, major problems could still not be resolved. Among these issues, the experimental limitations to systems exhibiting a fast heat release upon adsorption and the lack of control over the cleanliness and structure of the sample (all the samples were polycrystalline) were the most severe ones. In addition, the complexity of the experimental set-ups, which were essentially home-made and the time-consuming nature of the experiments posed serious drawbacks. Together with the difficulties in the determination of the amount of gas that is adsorbed, the incompletely characterized and therefore not comparable films and problems arising from the calibration and data analysis procedures resulted in huge deviations in measurements on the same system in different laboratories. From the number of publications per year that contain calorimetry data from such apparatuses (see Table 1.1), one may conclude that the interest in such experiments and therefore their impact diminished over time as these problems became obvious. This did not lead to abolishment of the idea of obtaining calorimetric data from low surface area samples, but inspired new developments to overcome the problems encountered.

1.4.3 Microcalorimetry on Single Crystals

Despite the problems due to the polycrystallinity of the samples used in all previously described experimental approaches, it was not until 1986 that a calorimeter for studies of single crystals was devised (a schematic is shown in Figure 1.7) and first results were published by D. A. Kyser and R. J. Masel.^[97]

They performed adsorption experiments on a Pt(111) crystal disc with a diameter of 10 mm mounted on two thin tantalum wires. Two thermistors mounted in quartz capillaries in holes drilled through the crystal served as temperature sensor and heating elements for the calibration procedure. The crystal is housed in an UHV chamber which is also equipped for Auger Electron Spectroscopy (AES) measurements in order to ensure sample cleanliness and to determine adsorbate coverages. Temperature stabilization was achieved by a water bath and placing the whole assembly in a constant temperature room. The sample was heated in an oxygen atmosphere until no impurities could be detected with AES. However, this procedure required a long time for thermal equilibration before the actual experiment could be performed. Typically thermal equilibration took several hours. During this time, residual carbon monoxide could adsorb on the sample rendering

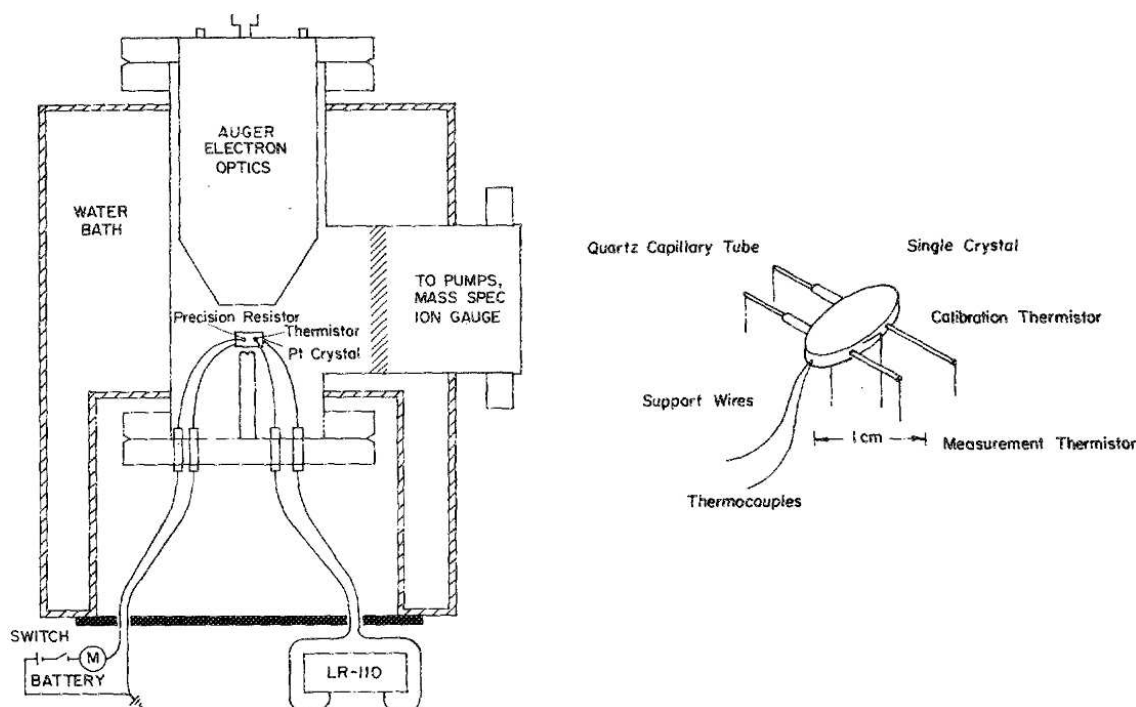


Figure 1.7: Schematics of the apparatus (left) and crystal mount (right) of the single crystal adsorption calorimeter developed by D. A. Kyser and coworkers (from [96]).

measurements in the low coverage regime impossible. Another problem was that the heating procedure caused irreversible changes in the thermistor, which thus had to be recalibrated for every single experiment. A considerable reduction of the heat capacity of the crystal, although impossible to achieve due to the way the calorimeter was assembled, would have increased the sensitivity and decreased the equilibration time. This way, the most pressing problems would have been solved. In the end, this approach was not developed further due to the mentioned problems, although reasonable results could be achieved for the adsorption of CO and C₂H₄ on platinum. Nevertheless, Kyser and Masel were the first to publish work on single crystals.

Sir D. A. King achieved a major breakthrough in this field, when he introduced a new strategy for adsorption calorimetry on single crystal surfaces in 1991: he used very thin (0.2 μm thick) single crystals. A prerequisite for this technique was a technical development at the University of Århus, where extremely thin single crystals could be prepared of many metals and of different orientations. Even stepped, thin crystals could be prepared. [98,99]

The heat delivered to the sample via adsorption is assumed to be lost mainly via

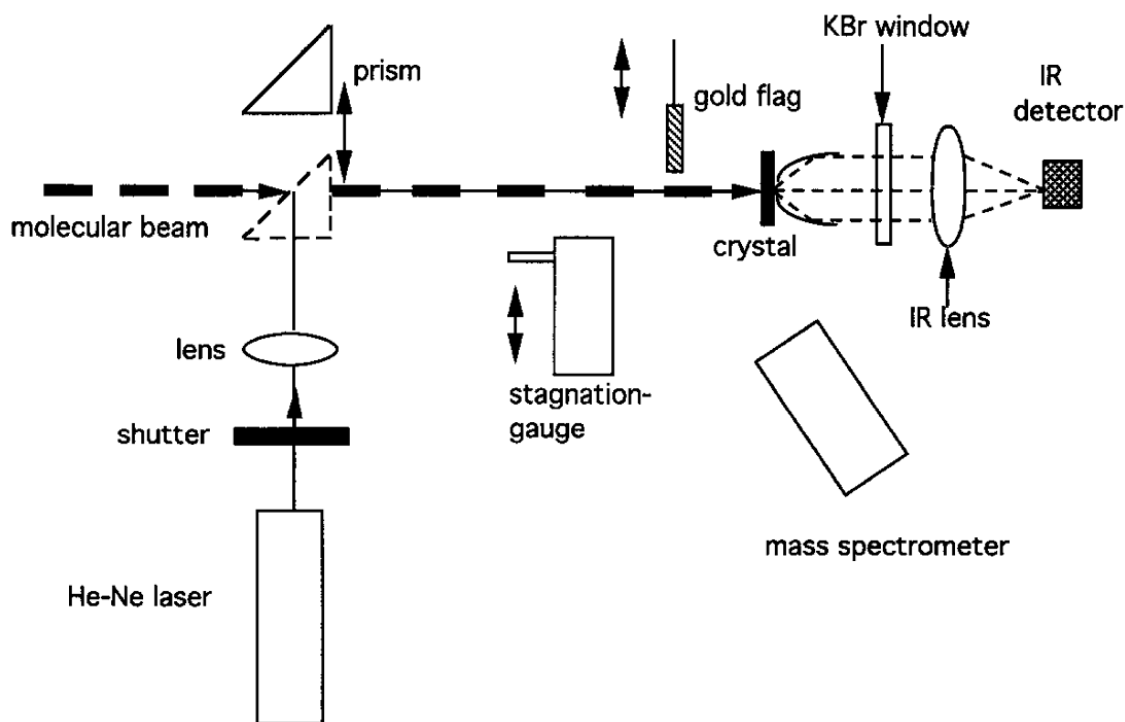


Figure 1.8: Single-crystal adsorption calorimeter using an IR detector for heat detection. ^[29]

radiation in an UHV environment. King used an IR detector (outside the chamber) to detect this radiation. The back face of the sample was blackened with carbon in order to increase the emissivity of the sample and thus the sensitivity of the set-up (a sketch is provided in Figure 1.8).

Low Energy Electron Diffraction (LEED) and AES were available to characterize the sample and ensure sample cleanliness. Knowledge of the impinging flux from the molecular beam onto the sample surface (via the stagnation gauge) and in-situ measurement of the sticking probability with the mass spectrometer (employing a modified King-Wells method) allow for a very accurate determination of the coverage without disturbing the calorimetric experiment. One of the difficulties connected with King's approach is that low temperatures are not accessible: according to the Stefan-Boltzmann law, the change of radiated power with temperature is proportional to $\Delta T \cdot T^3$ causing the signal to drop very fast at low temperatures. ^[76] Another problem is that in cases of low adsorption enthalpies, the number of molecules desorbing in between two gas pulses becomes equal to the number of molecules adsorbing during each pulse. In such cases, determination of the coverage is difficult,

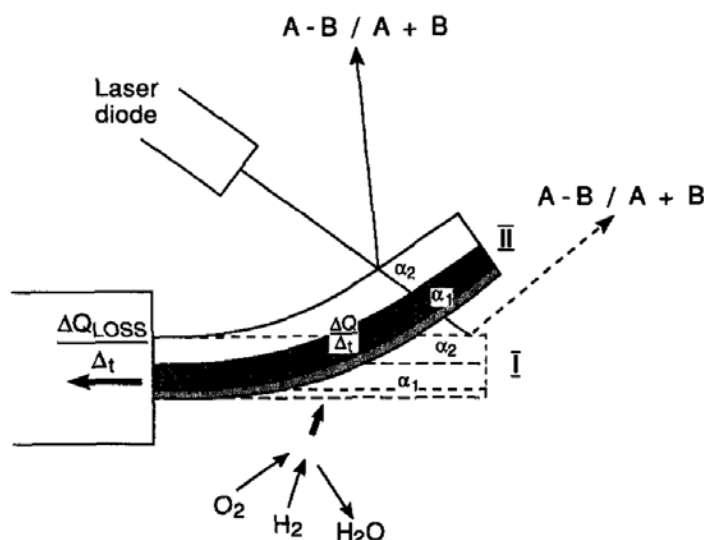


Figure 1.9: Schematic of the micromechanical sensor used by Gerber. ^[105]

as the measurements would falsely indicate an ever increasing coverage. ^[11,32,100–104] In order to overcome the problems connected with low temperature, the idea to use a pyroelectric material as the sensing element first proposed by Černý was revitalized. Use of such a detector in the calorimeter allowed for measurements at sample temperatures as low as 90 K and extremely small rises in temperature of only $2.5 \cdot 10^{-5}$ K could be detected. ^[29,32]

The experiments performed within the group around Sir D. A. King have contributed a lot towards a better understanding of the chemisorption of NO, CO and small hydrocarbons on different single-crystal surfaces. Certainly, their successful work on single-crystals has reestablished the use of calorimetric methods in modern surface science.

A different approach was taken by C. Gerber and his coworkers in 1994 by making use the different thermal expansion coefficients of different materials in a so-called micromechanical calorimeter. He used a bilayer cantilever (silicon/aluminum) as the temperature sensor ^[105–107]. Just like a bimetallic ribbon, this assembly is deformed as a result of a temperature change. The deformation of the cantilever due to a change in temperature can be detected in the same way as a deflection of a cantilever in atomic force microscopy (AFM): the reflection of a laser beam is analyzed with a position sensitive detector, in this case a two-segment photodiode.

This sensor (see Figure 1.9 for a schematic) proved to be extremely sensitive, such that heat fluxes in the nanowatt regime can be measured. A fast response time

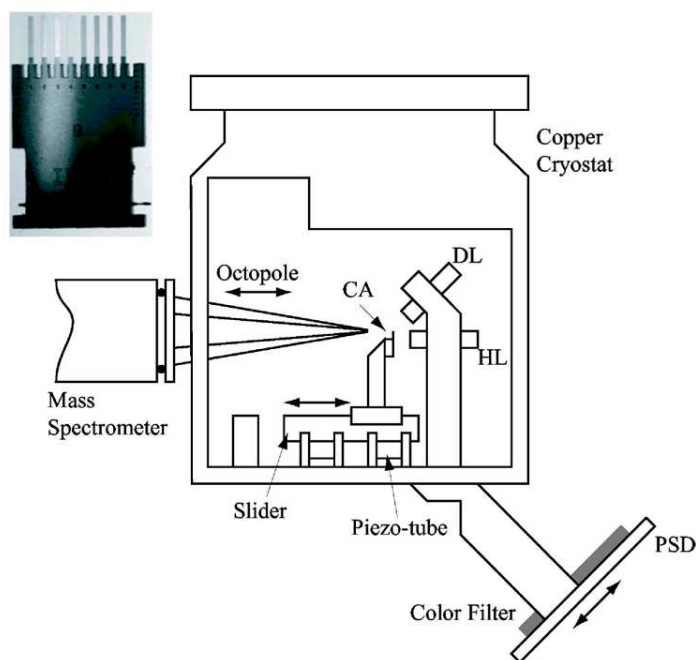


Figure 1.10: Schematic view of the apparatus used by Heiz (from [108]): PSD, position sensitive detector; DL, detection laser; HL, heating laser; CA, cantilever array. The inset shows a micrograph of the cantilever array.

of one millisecond sets the detection limit to $1 \cdot 10^{-12}$ J. These exceptional sensor characteristics are a direct result of its small heat capacity, which turned out to be a problem in many of the approaches attempted before. Gerber used this instrument to study the catalytic conversion of hydrogen and oxygen to water over a platinum surface. [105] One major issue in such miniature sensors is to determine the amounts that are adsorbed on the sample.

Heiz refined this concept and used cantilever arrays instead of single cantilevers as depicted in Figure 1.10. He studied the hydrogenation reaction of 1,3-butadiene on palladium clusters. [108] However, the problems connected with the determination of the amount adsorbed by the sample remained unsolved.

C. T. Campbell introduced a calorimeter in 1998 that used a pyroelectric heat detector. [14, 109] In contrast to the principally similar designs by Černý or King, his design (see Figures 1.11 and 2.1) incorporated a poled β -polyvinylidene fluoride (β -PVDF) ribbon as the heat detector. This design gives relatively good control over the substrate and allows even harsh cleaning procedures, as the detector can be retracted from the sample. At the same time, the heat capacity and the corresponding thermal equilibration time is still very low, such that experiments do not suffer from too

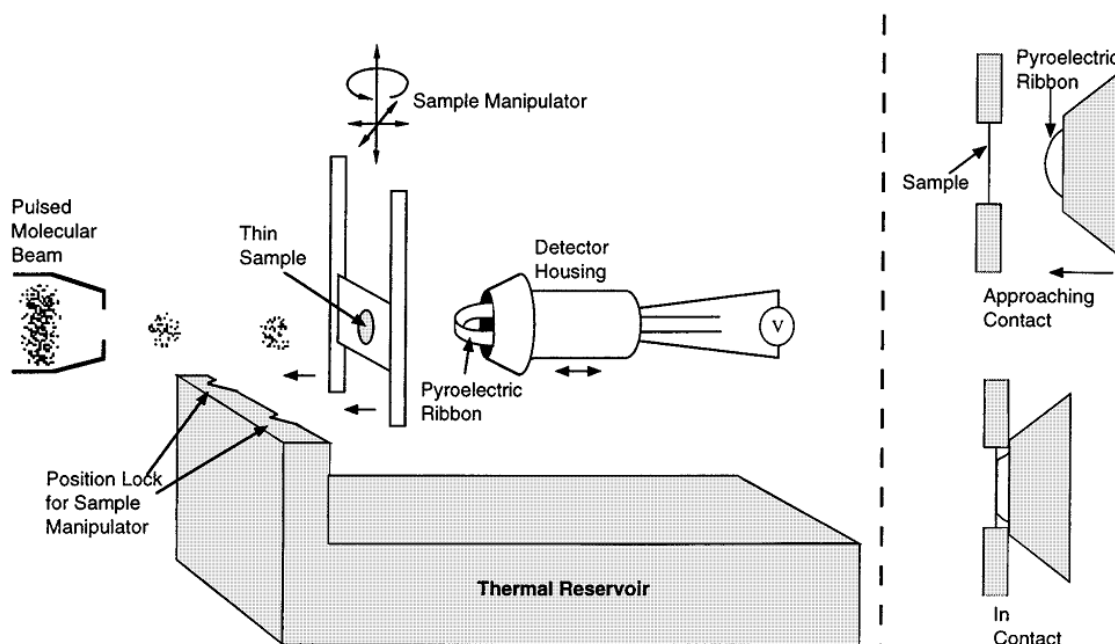


Figure 1.11: Schematic of the Campbell-Calorimeter from [14].

extensive preparation or equilibration times. Systems studied with this kind of set-up include metal adsorption on magnesium oxide, ^[110,111] adsorption of hydrocarbons on platinum surfaces ^[109,112–114] and even adsorption of metals on polymers. ^[115,116] This concept has been adopted and modified by three groups so far, although these groups have not published results yet (S. Schauer mann / H.-J. Freund, Fritz Haber Institut, Berlin; R. Schäfer, TU Darmstadt; J. M. Gottfried / H.-P. Steinrück, Universität Erlangen-Nürnberg). The development of a calorimeter of this type is an integral part of this dissertation and will be discussed in some detail within this work. The growing interest in adsorption calorimetry is also reflected in a growing number of publications: from 1996 to 2000, 23 papers containing adsorption calorimetry data were published, from 2001 until today the respective number amounts to 50. These numbers compare very favorably against the number of publications just before the breakthroughs by Campbell and King (see Table 1.1).

2 Experimental

The heat of adsorption data presented here were collected mainly by the author in Prof. C.T. Campbell's laboratory in Seattle within a cooperative project between the University of Erlangen and the University of Washington funded by the German Academic Exchange Service ("Deutscher Akademischer Austauschdienst" DAAD). These data are complemented by X-ray photoelectron spectroscopy (XPS) performed mainly in Erlangen.

In this section, the different experimental setups employed will be described along with the respective relevant techniques they provide. The systems discussed include the calorimetry chamber in Prof. Campbell's laboratory in Seattle and the Scienta SES-200 XPS spectrometer in Erlangen.

The preparation of the polymer samples and the qualities of the different polymers will be described at the end of the chapter.

2.1 Calorimetry Apparatus

The calorimeter, including the heat detector shown in Figure 1.11 in the introductory chapter, is housed in an ultrahigh vacuum (UHV) chamber with a base pressure of $1 \cdot 10^{-10}$ mbar shown in Figure 2.1. Besides the calorimeter, the following experimental tools are available: low-energy electron diffraction (LEED) optics, a hemispherical electron energy analyzer providing Auger electron spectroscopy (AES) with the electron gun of the LEED optics as the excitation source and low energy ion scattering spectroscopy (LEIS) employing a focused ion source, a quartz crystal microbalance (QCM), a quadrupole mass spectrometer (QMS) and a metal atom source.

2.1.1 The Calorimeter

A pyroelectric material, i.e., a material exhibiting a permanent polarization, is used as the detector material. The material used in the calorimeter in Seattle is poled β -polyvinylidene fluoride (β -PVDF) in the form of a sheet coated on both faces

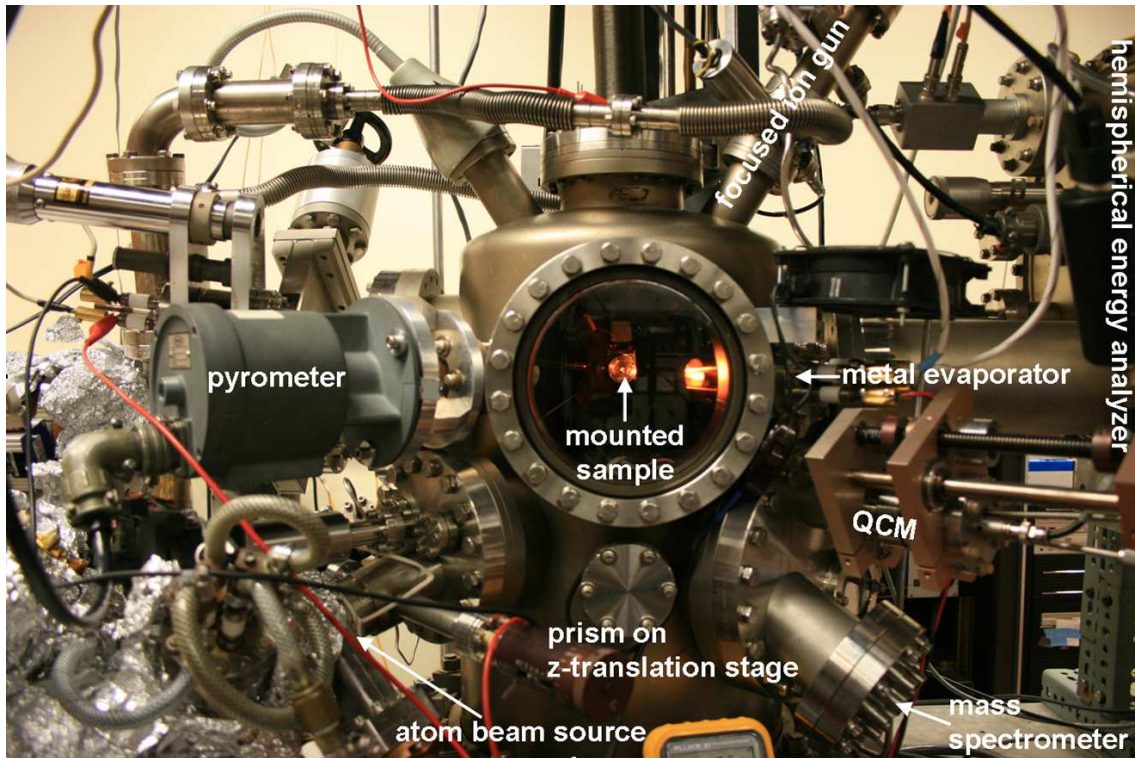


Figure 2.1: The calorimetry chamber in Professor Campbell's laboratory. The most important visible parts are labeled. (Picture by Jack H. Baricuatro)

with nickel aluminum. This metallic coating ensures that the polarization of the pyroelectric is compensated by free electrons in the metal coating, when the two faces are electrically connected. Heat input, for example from the adsorption of atoms, leads to thermal fluctuations within the pyroelectric and changes its polarization momentarily. This changed polarization is in turn compensated via a charge transfer between the two faces, i.e., a current. The current compensating the change in polarization is amplified and serves as the measure for the amount of heat deposited. For adsorption experiments using a polymer as the substrate, the detector geometry shown in Figure 2.2 is used: the metal coated poled β -PVDF sheet is held in place by a copper face plate screwed to the sample platen. This also connects the front face electrically to the outer portion of the assembly. The back face of the detector sheet is connected only to a signal bolt that is electrically insulated from the rest of the sample platen. Front and back face of the detector sheet or the signal bolt and the rest of the sample platen are electrically connected via the preamplifier serving to extract and amplify the current resulting from heat input.

The polymer film serving as the substrate for the calorimetry experiments can be

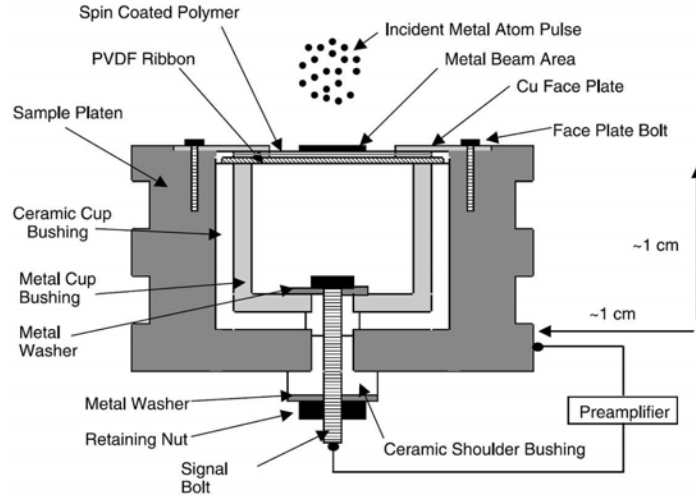


Figure 2.2: Schematic of the detector assembly for the study of adsorption on polymers from Reference [116].

deposited directly onto the detector sheet ensuring the best thermal contact between polymeric substrate and the pyroelectric detector possible. For the experiments reported here, the polymer films were spin coated onto the detector sheet. Spin coating, also referred to as spin casting, is a procedure to deposit films of a material on a substrate. A solution of the material to be deposited is squirted from a pipette in the center of the substrate, which is rotating at a constant speed. Due to the centrifugal force, the solution deposited in the center is accelerated towards the edge of the sample and a compact area is covered with the solution. Upon evaporation of the solvent, a film of the dissolved material remains on the substrate. This technique usually gives films of a fairly homogenous thickness. It furthermore allows control over the film thickness via the rotational speed of the substrate or the solvent used. Other techniques for the deposition of polymer films from solution include dip coating and drop casting. Dip coating refers to a procedure, where the substrate is immersed in a solution of the material to be deposited and pulled out of the solution, usually at a constant speed. Similar to spin coating, this technique allows some control over the deposited film morphology via the speed with which the substrate is removed from the solution or via the solvent itself. For drop casting, a solution of the material to be deposited is applied to the substrate, which in contrast to spin coating is not revolving. In contrast to the two other methods described above, this procedure generally does not result in uniform films and does not allow as much control over the film thickness.

The sample platen is held firmly in a sample fork which is connected to a thermal reservoir, a copper block, during measurement. The idea behind this is twofold: first, this configuration ensures thermal stability and second the firm mechanical contact minimizes vibrations. The latter point is of great importance, because every pyroelectric material is also piezoelectric. Therefore, mechanical vibrations constitute the main source of noise on the detector and must be suppressed. Amplification changes the signal from a current to a voltage, which is recorded using a computer with a digital interface card. A measure for the sensitivity of the sensor can be calculated by dividing the output signal by the total gain of the amplification. With the set-up described above, this sensitivity typically amounts to 450 V/J. ^[116]

On a side note, in experiments where a single crystal is used as the substrate, a slightly different setup is used: a ribbon made of β -PVDF is pressed against the back face of the crystal during measurements. Obviously, this method provides a far worse thermal contact between the sensing element and the sample and the typical sensitivity amounts to only 100 V/J. ^[14] Not surprisingly, the sensitivity value for polymer samples which are directly spin coated onto the detector compares quite favorably against the one for single crystalline samples. This in turn allows for more flexibility with other experimental parameters, for example the flux of the adsorptive.

2.1.2 The Metal Atom Beam Source

The metal beam source providing the metal flux for the adsorption experiments is shown in Figure 2.3. It incorporates a commercially available high-temperature, high-volume metal effusion cell (EPI-10-HT) with a 10 cm³ crucible. The metal (in this work: calcium) was evaporated from an alumina liner placed in a tungsten crucible at temperatures around 1000 K. ^[115] This alumina liner and limitations in the filling height of the liner caused by the almost horizontal orientation of the Knudsen cell reduced the filling capacity to around 2.5 cm³. The two beam defining apertures of 2 mm radius (108 mm and 303 mm downstream from the Knudsen cell) are shown in Figure 2.3, while another two, water-cooled apertures close to the mouth of the source are omitted from the sketch. The two water-cooled apertures mainly serve to prevent fast blocking of the beam defining apertures and must be cleaned regularly, usually upon every third calcium filling. The aperture set-up not only collimates the beam to give an umbra (region of constant flux) of 4 mm diameter in which 91 % of the atoms are deposited, but also shields the sample from non line-of-sight thermal

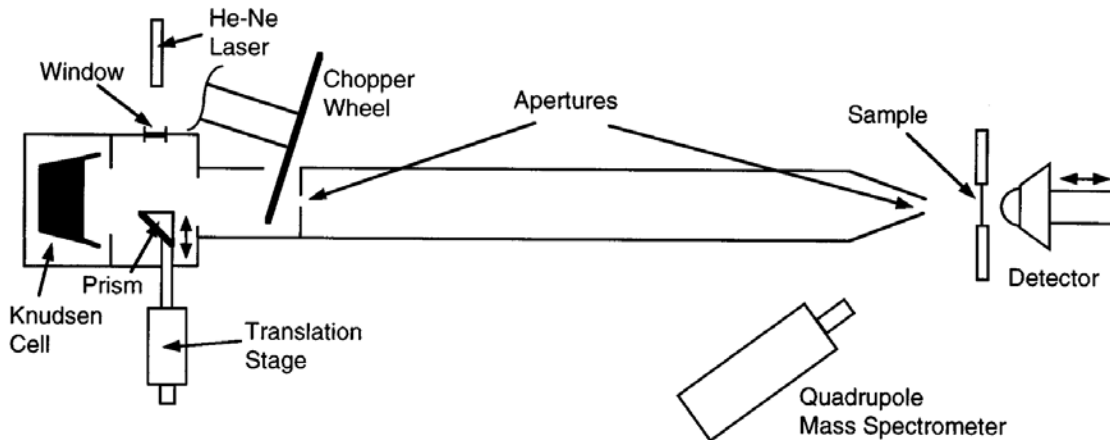


Figure 2.3: Schematic diagram of the Knudsen cell and associated atom beam path and optic elements used for laser calibration of the calorimeter from Reference [14] (not drawn to scale).

radiation from the oven. The complete beam path up to the last aperture is placed in a tapered snout allowing for efficient differential pumping of the beam source. The snout also prevents non line-of-sight atoms and stray light originating from the hot Knudsen cell from reaching the sample, as these are both adsorbed by its blackened inner walls. A mechanically driven chopper-wheel is installed in the beam path in order to transform the constant flux from the Knudsen cell into 100 ms long pulses with a repetition rate of 0.5 Hz. A turbomolecular pump placed near the mouth of the Knudsen cell allows for independent pumping of the molecular/atomic beam source. A gate valve downstream of the chopper wheel separates the main chamber from the beam source. Thus, the Knudsen cell may be refilled and degassed without breaking or degrading the vacuum in the main chamber. For the investigations involving adsorption of metal atoms on a sample surface a new problem arises. Opposite to the studies using volatile adsorptives like gases or light hydrocarbons, which both do not require a heated source, the radiation from the hot metal source is detected as a contribution to the heat signal, as part of it is absorbed by the sample. The metal atom beam is designed such that the heat contribution is low because of the large distance between the Knudsen cell and the sample (312 mm). As the radiance decreases with distance as $1/r^2$, this distance helps to minimize the radiative contribution to the measured heat signal. The flux, of course, also decreases with distance in the same way. Fortunately, this can be compensated by raising the temperature. However, as the flux increases exponentially (Arrhenius

law) and thus faster than the radiative energy (T^4 dependence, Stefan-Boltzmann law), a large distance indeed can be used to effectively lower the radiation impinging on the sample at a given flux. In order to account for the portion of the radiation still reaching the sample, a BaF_2 window can be placed between snout and sample. As BaF_2 transmits a large part of the radiation, but is impenetrable for metal atoms, this allows for measurement of the radiative contribution captured by the calorimeter. The material's specification imply that only $\sim 8\%$ of the radiation from a black body in the temperature range between 1130 K and 1660 K are not transmitted. Measurements with and without the window in the beam path thus directly yield the radiative contribution from the hot Knudsen cell within reasonable limits and the measured heats of adsorption can easily be corrected for it. It shall be noted that a number of factors complicated the exact determination and correction of the radiative contribution. First of all, the Knudsen cell is not strictly a black body and the temperatures used for the deposition of calcium are below 1130 K. As a result, the amount of heat not transmitted by the window is probably larger than 8%. Secondly, the transmittance of the window deteriorates with time in the beam path due to metal deposition. The helium-neon laser (also used for the laser calibration discussed below) can only probe the transmittance at a wavelength of 632.8 nm. This allows for correction of small changes in the window's transmittance. Of course, this test can not be used to correct for large changes caused by massive contaminations, as these most likely would also change the spectral characteristic of the window's transmission function. Whenever the test procedure with the laser indicates such a large contamination of the window, a clean spot on the window is used or the window is replaced. Another difficulty is that the absorbance of the sample may change as the experiment proceeds and the metal coverage is increased. In reasonable intervals, the changes in sample reflectivity can be determined using the procedure employed to determine the radiative contribution or alternatively by comparing the heat input caused by the calibration laser at different stages of the experiment. The latter procedure is much faster and is less invasive on the experiment, yet it probes the sample reflectivity only at one wavelength, which was mentioned as a problem above, already. Yet another limitation in the effort to account for the radiative contribution to the measured heat is that the radiative power incident on the sample is assumed to be constant, which is not necessarily the case. In reality, fluctuations and changes in the fill level of the cell for example may lead to small errors.

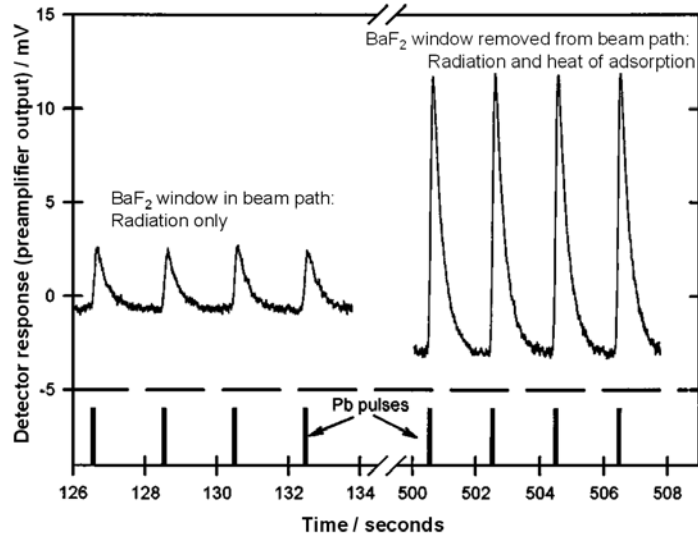


Figure 2.4: Detector response to pulses of lead atoms with and without the BaF_2 window in the beam path (from Reference [14]).

To demonstrate the approximate size of the heat signal generated by the radiation from the metal beam source, the detector response to pulses of lead atoms with and without the BaF_2 window in the beam path is shown in Figure 2.4. It is obvious that the effect mandates a correction as the signal due to radiation is approximately 20 % of the total amount of heat deposited in the sample by adsorption of lead atoms.

2.1.3 Calorimeter Calibration

The significance and difficulties related to the absolute calibration of adsorption calorimeters have already been pointed out. Similar to the approach by D. A. King, the Seattle group employs the same He-Ne laser for calibration of the detector and for checking the transmission of the BaF_2 window mentioned above. The laser beam is shone through a beam expander, which enlarges the illuminated area, and a window onto the prism in the beam chamber (see Figure 2.3). In its proper position for calibration, the prism redirects the incoming, expanded laser beam by 90° such that the laser light takes exactly the same path to the sample that metal atoms from the Knudsen cell would take. As it has to pass all beam defining apertures, the spot illuminated on the sample closely resembles the region in which metal atoms are deposited. The laser beam also passes the chopper and consequently the laser pulses arriving at the sample have the same spatio-temporal characteristic as

the metal atom pulses from the Knudsen cell. The heat inputs from both sources are directly comparable under the condition that the adsorption process and the connected deposition of heat in the sample are occurring on the same timescale and the signal shapes are very similar. This condition is considered to be fulfilled when the heat input is completed, e.g., the adsorbate finds its final configuration, on a timescale much smaller than the time constant of the detection system (usually 200 ms). Delayed heat input on a timescale comparable to the time constant of the detection system, for example caused by restructuring of the adsorbate or a delayed heat input due to diffusion processes, should appear as resolvable changes in the line shape. Although determination of the heat released in such slow processes is uncertain, a detailed analysis of the line shape, e.g., by deconvolution, can in principle be used to reveal the dynamics of the processes involved.

To this point, the procedure allows only ascertaining that the signals arising from adsorption of metal atoms and absorption of laser light may indeed be compared and can be related to each other. Absolute calibration calls for determination of the heat deposited into the sample by the laser in each pulse. That in turn requires knowledge of two quantities: the laser intensity at the sample position and the reflectance of the sample at the laser wavelength. A calibrated photodiode detector placed at the sample position for the respective measurements is employed to determine the first one. The latter one is measured using an integrating sphere. In the study involving polymeric substrates, each individual sample is measured. For metal single crystal samples, this procedure may be performed once and one assumes that the cleaned sample will always exhibit the same constant reflectivity. In any case, the literature value for the respective bulk material may be used in first approximation. With knowledge of the detector response, the laser intensity and the sample reflectance at the laser wavelength, the detector signal can readily be converted into an absolute amount of energy deposited in the sample via multiplying the laser power at the sample with the pulse length resulting in the pulse energy. Multiplication of this pulse energy with the absorbance of the sample then gives the amount of energy deposited, which can readily be related to the detector output to give the sensitivity of the set-up.

As the reflectivity measurements are so crucial for the accuracy of the data collected, some of the problems in this context shall be discussed. First of all, the choice of a suitable laser and its respective wave length is essential, because the measurements are more prone to errors when the reflectivity of the sample is too high. As the

reliability of the reflectivity measurement is about $\pm 1\%$ and the absorbance may be expressed as follows:

$$R = 1 - A \quad (2.1)$$

Here, A denotes the absorbance and R the reflectivity of the sample. Very high reflectivity values lead to large errors, because the error is of the same order as the quantity to be determined.

Proper calibration of the calorimeter calls for repetition of the described procedure for different amounts of energy deposited per laser pulse, which can be easily done via attenuation of the laser using neutral density filters. Proportionality of the detector response with respect to the amount of energy was demonstrated by correlating the detector signal with the amount of heat deposited in a range between $0.12\ \mu\text{J}$ and $12\ \mu\text{J}$ per pulse.^[14]

2.1.4 Beam Flux Measurements

A quartz crystal microbalance (QCM) that can be placed in front of the nozzle of the atom beam source is used to measure the beam flux absolutely so as to allow determination of heats of adsorption per adsorbed atom. As the deposition spot is much smaller than the active area of the crystal, a calibration of the QCM is mandatory, because the specified accuracy of the device applies to a uniform deposition on the whole active detector area. Furthermore, a calibration increases the accuracy in converting the readings to absolute amounts of metal dosed onto the detector. Calibration of the QCM is done via dissolving the metal from the quartz crystal in a known volume of acid. The solution is subsequently analyzed quantitatively for its metal content employing inductively coupled plasma atomic emission spectroscopy. This procedure is repeated after each series of experiments. As the deposition spot can be seen with the naked eye, correct positioning of the QCM can be checked at the same time.

2.1.5 In-situ Determination of the Sticking Probability

In order to relate the heat released to the number of atoms that contribute to this heat, one obviously needs knowledge of the number of atoms that adsorb on the sample. This measurement is done employing a modified King and Wells method.^[117] While the original King and Wells method employs a non line-of-sight mass spectrometer to measure the fraction of atoms/molecules that do not permanently adsorb

on the sample, a line-of-sight mass spectrometer is employed in the modified method. The original method is void of influences on the signal caused by the angular distribution and velocity of the atoms leaving the surface, which is highly desirable. However, the technique is only applicable in cases where the atoms/molecules do not stick to the chamber walls. In the case of metal deposition, the sticking coefficient at the walls is high, which makes the line-of-sight detection of the desorbing species mandatory. The metal atoms may desorb from the surface in a broad angular distribution, in many cases the variation in this distribution can be expressed as a $\cos^n(\theta)$ function, where θ is the angle to the surface normal and n is a parameter assuming values typically between one and nine.^[118,119] Problems arise when n changes with coverage, because then the measured mass spectrometer signal also depends on n . However, it has been shown that a “magic angle” for the mass spectrometer position relative to the surface normal of the sample exists, under which the dependence on n is smaller than under every other angle. This angle depends on the sample dimensions and the distance between sample and mass spectrometer. Typical values for this angle, also referred to as “magic angle for desorption” (see Reference [119]) are 34° to 42° .^[119] In Seattle, a QMS is placed at an angle of 35° to the surface normal, the “magic angle” for this setup. In order to obtain the sticking probability, e.g., the fraction of atoms that adsorb permanently on the sample, a so called “zero sticking reference” is needed. This reference is obtained via desorbing a known amount of metal from a tantalum foil located at the same position as the sample during calorimetric experiments. The foil is heated to high temperatures and the mass spectrometer signal is recorded.^[14,120,121] The recorded signal is corrected for the average velocity of the desorbing atoms: the mass spectrometer signal is proportional to the residence time of the impinging atoms within the ionization volume of the spectrometer. The proportionality of the residence time τ to the inverse velocity of the molecules/atoms is evident from the following relation:

$$\tau \propto v^{-1} = \left(\sqrt{\frac{2 \cdot E_{\text{kin}}}{m}} \right)^{-1} = \left(\sqrt{\frac{4 \cdot k_B \cdot T}{m}} \right)^{-1} \quad (2.2)$$

Here, m denotes the mass of the atom, E_{kin} its kinetic energy, k_B the Boltzmann constant and T the temperature and assuming for the kinetic energy of the atoms a value of $4/2 \cdot k_B \cdot T$, as the atoms desorbing from the surface into the detection volume of the mass spectrometer constitute a flux (see Reference [118]). Thus, the spectrometer response is proportional to $T^{-1/2}$.^[118] From the comparison of the

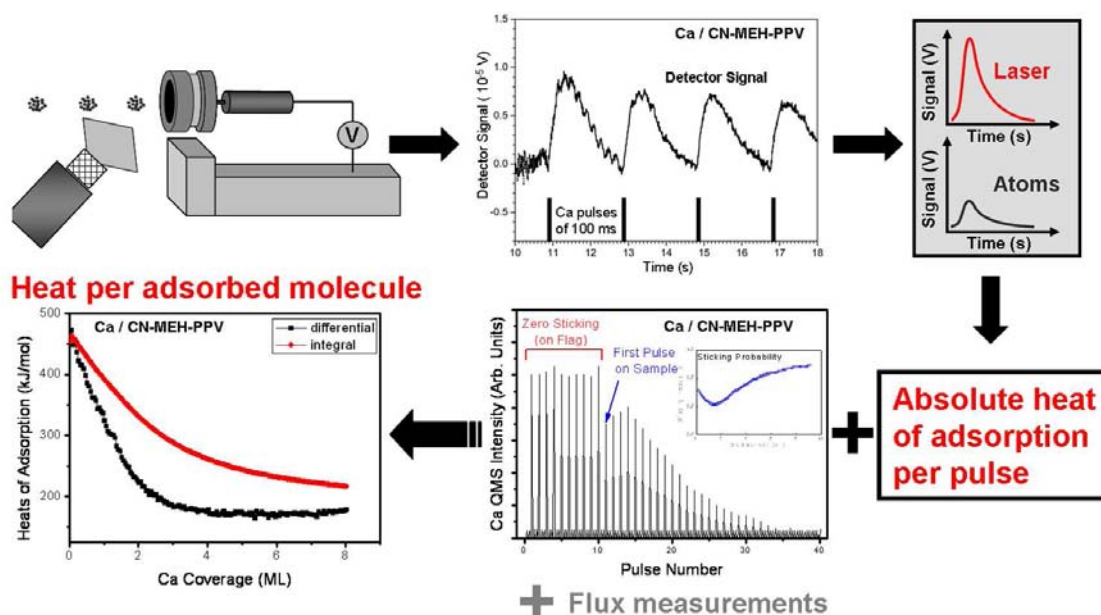


Figure 2.5: Graphical summary of the course of a calorimetric experiment and the data necessary to extract the experimental heat of adsorption values from an experiment.

QMS signal recorded during the experiment with the zero sticking reference, the fraction of desorbing atoms can be determined. From the desorbing fraction of atoms, the number of permanently adsorbed atoms may be calculated, as well. In the comparison of the two signals, one must take the flux used for the respective experiment into account, of course, so as to allow to adjust the height of the zero sticking reference to the number of atoms actually impinging on the sample. This way, the absolute amount of atoms deposited on the sample may be calculated by using combined sticking and QCM data.

All of the measurements discussed above – determination of the flux, zero-sticking reference and in-situ sticking probability measurements, laser calibration and the actual calorimetric experiment, e.g., dosing metal pulses on the sample and recording the detector output – must be conducted with high accuracy to finally yield the desired heat of adsorption, which is the primary objective of the investigation. A graphical summary of the complex experimental procedure is shown in Figure 2.5.

2.1.6 Relating the Measured Heat to the Adsorption Energy

As was alluded to in the introduction, heats of adsorption determined using the different methods may differ from each other. This obviously renders reported values void of meaning, if it is not explained what exactly the heat of adsorption is in the respective measurement. In the following, the heat of adsorption reported using nanocalorimetry will be well defined and its relation to the data will be explained. Deposition of a reactive metal such as calcium onto a polymer constitutes a complex situation and the adsorption process, i.e., the bonding of the calcium atom to the surface of the polymer, may be followed by diffusion into the surface near region and subsequently a reaction with a reactive group within the polymer. As these processes – diffusion and reaction – are occurring so fast that they are experimentally not distinguishable from the adsorption process, the definition of the adsorption energy E_{ads} shall be adapted to the situation at hand. Here, the adsorption energy is defined as the negative difference in internal energy $-\Delta U_{\text{ads}}$ between an initial state, a number of gaseous metal atoms and a solid surface, both at 300 K, and the final state, where a fraction of the dosed atoms is bonded to the substrate of the completely relaxed adsorption system. In this final state, calcium atoms may have diffused into the surface near bulk of the polymer and undergone a reaction there and do not necessarily form a true adsorbed phase. This way, the adsorption energy is independent of the structure the molecules assume in the final state.

The common definition of the adsorption energy uses the same initial state as in the definition above, but a different final state: there, the final state is that of the impinging atoms having bonded to the surface of the substrate, forming an adsorbed phase. No diffusion or reaction below the surface is allowed within this model. In any case, the two definitions of the adsorption energy are identical for systems, where a true adsorbed phase is formed by the impinging atoms/molecules in the calorimetric experiment.

The measured calorimetric heat Q_{cal} is the measured energy input per pulse of atoms referenced to the absolute laser calibration of the calorimeter discussed above. As the number of atoms in a given pulse is known, one can easily obtain the more meaningful molar heat of adsorption q_{cal} by dividing Q_{cal} by the number of moles of atoms in a pulse. This heat, of course, constitutes the difference between an initial and a final state. In the initial state, there is a pulse of atoms from a Knudsen cell at the source temperature T_{source} and a solid surface at its respective temperature, which is the room temperature in most cases. In the final state, all the atoms

dosed from the Knudsen cell are thermally equilibrated with the sample and the thermal reservoir. Hence, an adsorption/desorption mechanism is assumed for the non-sticking atoms instead of a bounce off mechanism. One should keep in mind that this is an assumption that is reasonable to make, but can lead to a small error, as there may well be a certain fraction of atoms that is not thermally equilibrated with the sample in the final state.

The difference between q_{cal} and E_{ads} as defined above is the difference between the kinetic energy of atoms in an effusive beam from a Knudsen cell ($\frac{4}{2} \cdot R \cdot T$)^[118] at the source temperature T_{source} and the kinetic energy of the same number of atoms in a Boltzmann distribution ($\frac{3}{2} \cdot R \cdot T$) at the sample temperature T_{sample} . This difference would be deposited in the sample irrespective of adsorption of atoms and must therefore be subtracted from the measured heat of adsorption in order to yield the adsorption energy^[14]:

$$E_{\text{ads}} = -\Delta U_{\text{ads}} = q_{\text{cal}} - \left(\frac{4}{2} \cdot R \cdot T_{\text{source}} - \frac{3}{2} \cdot R \cdot T_{\text{sample}} \right) \quad (2.3)$$

Here, it is assumed that all impinging atoms are completely thermally equilibrated after hitting the sample. This may not be exactly true for all systems, however the determination of the kinetic energy of the atoms leaving the surface is rather difficult. In addition, the error that may result from this assumption is small compared to typical heats of adsorption in the systems investigated within this work.

Similarly to the definition of the adsorption energy, the heat of adsorption Q_{ads} is defined as the negative of the change in standard enthalpy ΔH_{ads} for the same process whose energy of adsorption was derived above. ‘‘Standard’’ implies that all species are in their standard thermodynamic state corresponding to the standard pressure of one bar at standard temperature. The so defined heat of adsorption Q_{ads} is then directly comparable to standard enthalpy changes, for example standard enthalpy of sublimation with both phases at the same temperature. The only work done in an adsorption experiment is the gas-phase pressure-volume work, also quite descriptively in this context referred to as ‘‘work of compression’’. The pressure-volume work term as given below is well approximated by $-R \cdot T$:^[11]

$$p \cdot \frac{\Delta V_{\text{gas}}}{n_{\text{ads}}} \approx -R \cdot T_{\text{sample}} \quad (2.4)$$

Here, p refers to the gas-phase pressure, ΔV_{gas} to the change in the volume of the gas as a result of the adsorption process, and n_{ads} to the number of moles of adsorbate.

Accounting for the work of compression by adding $R \cdot T$ to the adsorption energy then yields for the heat of adsorption q_{ads} :

$$q_{\text{ads}} = q_{\text{cal}} - \left(\frac{4}{2} \cdot R \cdot T_{\text{source}} - \frac{5}{2} \cdot R \cdot T_{\text{sample}} \right) = -\Delta H_{\text{ads}} \quad (2.5)$$

To gain a feeling for the order of magnitude of the correction necessary to convert the measured heats q_{cal} into q_{ads} , consider the deposition of calcium atoms at room temperature in the multilayer regime with a typical evaporation temperature for calcium of 1000 K, such that the correction amounts to:

$$\frac{4}{2} \cdot R \cdot 1000 \text{ K} - \frac{5}{2} \cdot R \cdot 300 \text{ K} = 1250 \text{ K} \cdot R = 10.4 \frac{\text{kJ}}{\text{mol}} \quad (2.6)$$

Compared to the standard enthalpy of sublimation for calcium of 178 kJ/mol, this is a rather small correction on the order of 6 %. Nevertheless, one must take this correction into account in order to obtain the most accurate results possible.

2.2 The X-ray Photoelectron Spectrometer VG Scienta SES-200

The X-ray photoelectron spectrometer used for the XPS part of this work is depicted in Figure 2.6. The apparatus is a VG Scienta ESCA-200 photoelectron spectrometer modified to meet the experimental requirements in Dr. J. M. Gottfried's group.

The apparatus with a base pressure of about $2 \cdot 10^{-10}$ mbar comprises an analysis and a preparation chamber separated by a gate valve. Pumping of the analysis chamber is done via a turbo molecular pump, an ion getter pump and a titanium sublimation pump. This chamber is equipped with an Al- K_{α} X-ray source and an X-ray monochromator for XPS experiments at a photon energy of 1486.6 eV. It also provides a differentially pumped gas discharge lamp (UVL-HI, Fisons) for ultraviolet photoelectron spectroscopy (UPS). In both cases, the photoelectrons are analyzed with a hemispherical energy analyzer (SES-200). An ion gun (IQE 12/38, Specs) allows for low energy ion spectroscopy (LEIS) measurements. The preparation chamber is pumped via a turbomolecular pump. Additionally, the rotary feedthrough of the manipulator attached to the preparation chamber is pumped by an ion getter pump and a rotary vane pump. The preparation chamber provides a sputter gun (ISS-2000-A, VSI Vacuum Instruments GmbH), a QCM (STM-100/MF, Sycon Instruments), a QMS (QMA 400, Pfeiffer Vacuum), a low energy electron diffraction

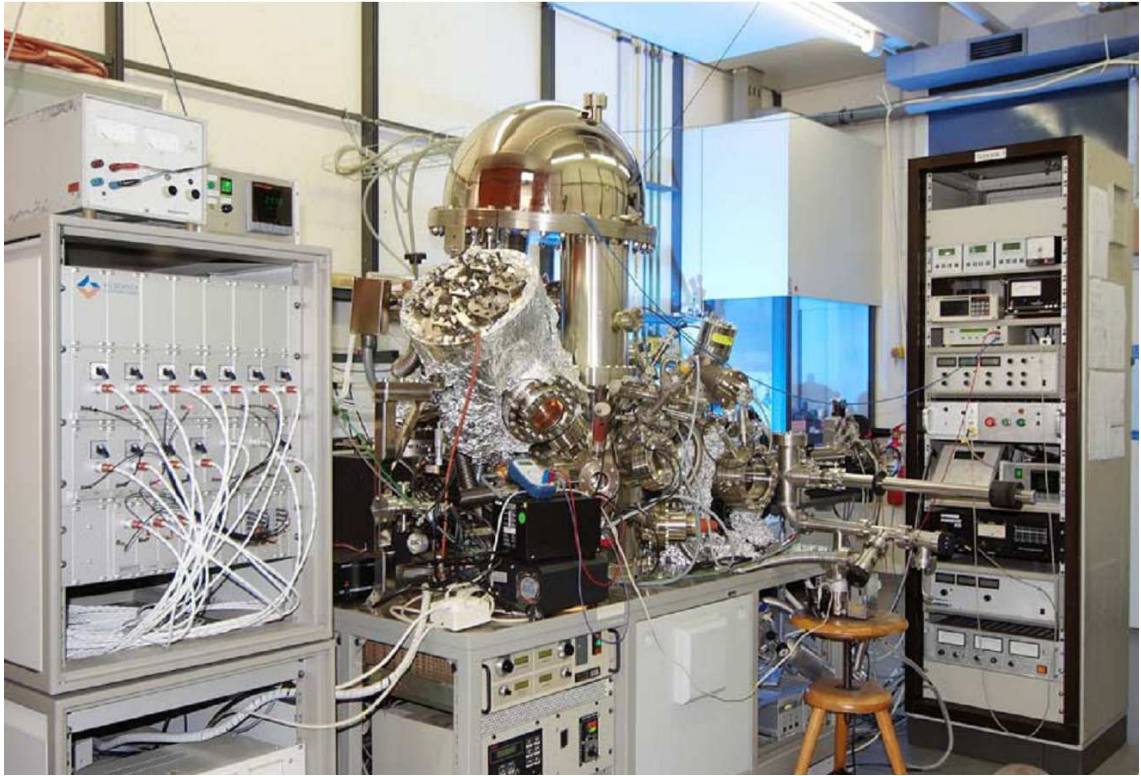


Figure 2.6: The Scienta SES-200 X-ray photoelectron spectrometer – the ultra high vacuum apparatus used for the XP spectra acquisition in this work. Center: spectroscopy chamber with hemispherical energy analyzer (top), X-ray monochromator (left), UV light and ion sources; left: analyzer electronics; right: preparation chamber with load lock, mass spectrometer, LEED optics, evaporators and some more electronics.

(LEED) optic (ErLEED-1000A, VSI Vacuum Instruments GmbH), an electron-beam evaporator (EFM3, Focus) and an in house built Knudsen cell evaporator.

The Knudsen cell evaporator used for deposition of calcium in this work was designed by Dr. Florian Maier and is depicted in Figure 2.7. It is separated from the preparation chamber by a gate valve and pumped independently by a turbomolecular pump. This setup allows for a change of the substance to be evaporated without breaking the vacuum in the preparation chamber. The manipulator can position a permanently mounted sample, as well as a transferable sample, which may be introduced to the preparation chamber from the load lock chamber equipped with another turbomolecular pump.

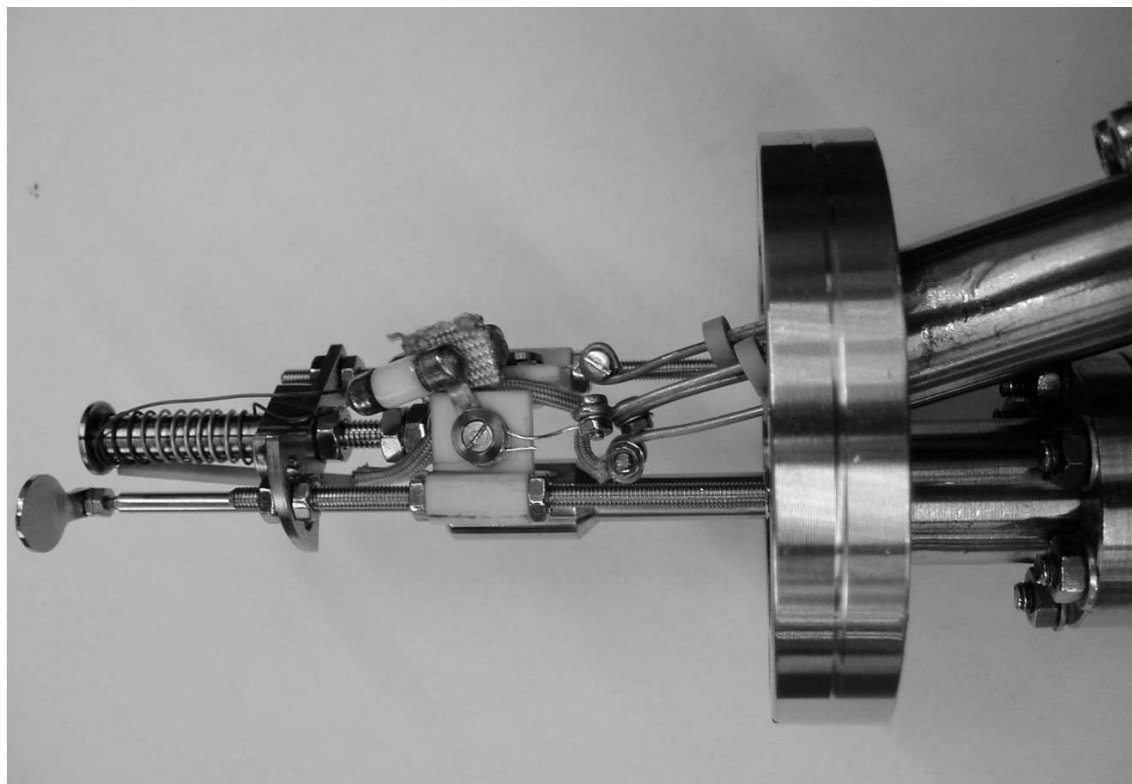


Figure 2.7: The Knudsen cell type evaporator used for the deposition of calcium on the polymer, here shown without its heat shield.

2.2.1 Fundamentals of Photoelectron Spectroscopy

Photoelectron spectroscopy employs the interaction between photons of a certain energy $E = h \cdot \nu$ with matter. The matter under investigation here are polymer films and calcium covered polymer films. Interaction of photons and matter leads to the emission of electrons, so called photoelectrons, with a specific kinetic energy E_{kin} . Considering an ideal process without any other interactions, the kinetic energy and the binding energy E_{B} are related to each other via the Einstein Equation:

$$E_{\text{B}} = h \cdot \nu - E_{\text{kin}} \quad (2.7)$$

The kinetic energy of the photoelectrons can be determined using an electron energy analyzer. The set-up used for data collection within this work employs a hemispherical capacitor, which deflects only electrons with the correct kinetic energy to the detector. Analyzers of this type are commonly referred to as hemispherical energy analyzers.

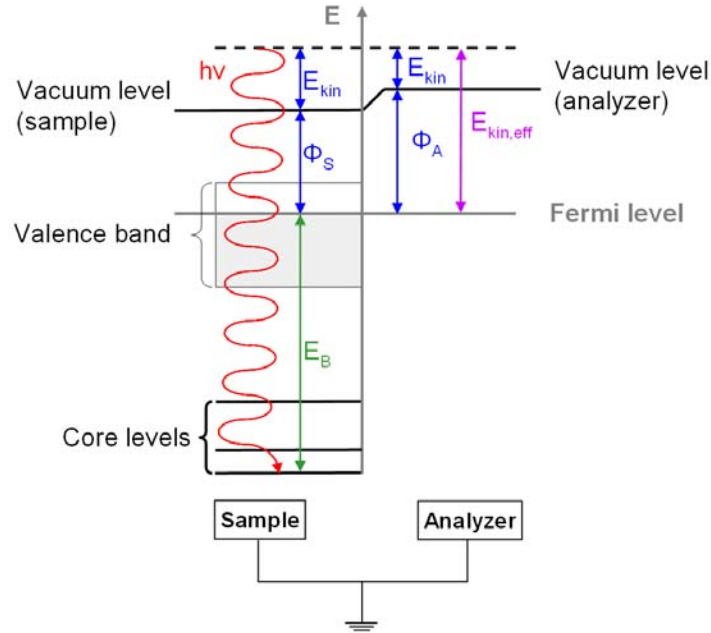


Figure 2.8: Schematic energy diagram (for a metal) for photoelectron spectroscopy. ^[122, 123]

The common reference level for binding energies used in gas phase experiments and in calculations is the vacuum level E_{vac} . The choice of this reference level is based on it representing a state with no interaction between the photoelectron and the core hole state. For condensed matter, the Fermi level is usually used as the reference. As the sample and the analyzer are electrically connected and grounded, a common Fermi level is established. This way, the binding energy with respect to the Fermi level may be calculated without explicit knowledge of the work function of the sample Φ_S and the work function of the analyzer Φ_A and the kinetic energy of the photoelectrons at the sample position. Only the energy relative to the Fermi level, $E_{kin,eff}$, is of importance. This quantity may be obtained from the measured kinetic energy of the photoelectron at the analyzer position and the work function of the analyzer, which is usually known from calibration of the spectrometer. The scheme in Figure 2.8 shows the relations between the various energy levels mentioned above.

A standard procedure to determine the Fermi level is to use a well known and reproducible feature in an XP spectrum to calibrate the energy scale of the spectrometer. It is evident that the best results are obtained employing features that show a high intensity and a small energetic width, e.g. the Au $4f_{7/2}$ peak.

The ideal case in which the emitted photoelectron does not interact with the surrounding matter is rather a special case. Typical interactions that occur are inelastic scattering, which includes excitation of electron-hole pairs (excitons) at or near the Fermi level of metals, vibrational and other electronic excitations. A photoelectron may well undergo several of such interactions before finally leaving the sample and prior to its detection in the analyzer. Due to these losses, the photoelectron exhibits a lower kinetic energy and thus a higher apparent binding energy. Such scattering events produce secondary electrons, i.e., electrons that gain sufficient energy from scattering events with photoelectrons to leave the sample. The secondary electrons in turn explain the steep increase of the background at low kinetic energy, ergo at high binding energy, that is often observed in XP spectra.

The chemical surrounding of a molecule or an atom does influence its core electrons, even though the core-electrons are not directly involved in chemical bonds. Consequently, the core levels of the same species in different chemical environments are shifted with respect to each other. The effects leading to this behavior can be divided into so called initial state effects and final state effects. The two terms refer to the states before and during the photoelectron emission process. The binding energy obviously is the difference of their respective energies:

$$E_B = E_f^{N-1} - E_i^N \quad (2.8)$$

with E_f^{N-1} denoting the energy of the final state with $N - 1$ electrons and E_i^N representing the energy of the initial state with N electrons. Koopmans' Theorem states that, under the assumption of the spatial distribution and the energies of the remaining $N - 1$ electrons after the photoionisation process remaining unchanged, the binding energy or Koopmans' Energy E_K , is equal to the negative orbital energy of the emitted photoelectron.

The frozen orbital approximation ignores relativistic and correlation effects, which both usually increase the core electron binding energies by δ_{rel} and δ_{corr} , respectively. Also, the possibility of a relaxation of the $N - 1$ -electron system to minimize its energy and an according decrease in the binding energy by δ_{relax} is not considered within this model. Taking these effects into account, the binding energy is more accurately described by the following equation:

$$E_B = E_K - \delta_{\text{rel}} - \delta_{\text{corr}} + \delta_{\text{relax}} \quad (2.9)$$

An exemplary initial state effect is the presence of a partial charge at the emitting atom: the measured kinetic energy is usually higher in case of a negative partial charge and lower for a positive partial charge. This effect can be easily explained with the decreased (negative charge) or increased (positive charge) Coulomb interaction between the photoelectron and the sample.

A prototypical final state effect is a more efficient screening of the core hole created by the photoemission process by surrounding electrons. The more effective screening lowers the interaction between core hole and the emitted photoelectron so that the photoelectron has a larger kinetic energy due to a decreased Coulomb interaction. Inefficient screening in contrast, leads to a lower kinetic energy of the photoelectron, as the interaction between the core-hole and the photoelectron is increased.

Core levels of different elements are in many cases well separated in binding energy and can therefore be measured separately and analyzed quantitatively. The ability to quantify X-ray photoelectron spectroscopy data led the usage of the term “electron spectroscopy for chemical analysis” (ESCA), reflecting the quantifying character of such experiments.

2.2.2 Layer Thickness Determination Using XPS

One way to exploit the quantitative nature of XPS experiments is to determine the thickness of a layer. For a very simple model system consisting of a homogenous overlayer on a thick sample, the thickness of the overlayer may be determined by comparing XP spectra containing a substrate peak before and after the overlayer is deposited. Making use of the exponential damping of the substrate signal, the following equation may be used for the evaluation of such a situation: ^[123]

$$d = \frac{\lambda}{\cos(\vartheta)} \cdot \ln\left(\frac{I^0}{I}\right) \quad (2.10)$$

In this formula, d denotes the overlayer thickness, λ the inelastic mean free path (IMFP) of electrons at their respective kinetic energy in the overlayer material, the angle between surface normal and detection direction, also referred to as detection angle, I^0 the signal intensity before and I the signal intensity after deposition of the overlayer.

Although this is a quite common way to determine the thickness of metal films deposited on a substrate, for example, its range of application is rather limited. One reason for the limits of application is the need for two spectra recorded before

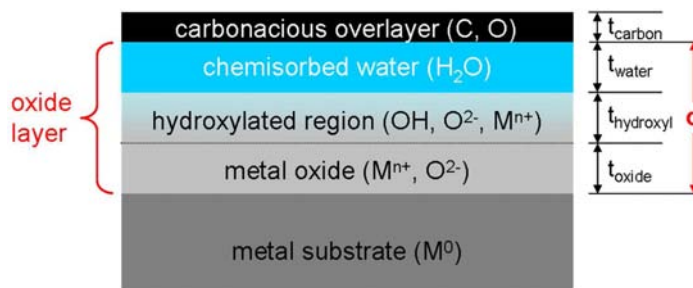


Figure 2.9: Schematic diagram of an oxide-covered metal investigated by McCafferty and Wightman. The different layers are shown along with their composition in parentheses and their respective thicknesses t . Also, the composition and thickness of what is commonly referred to as oxide layer is indicated.

and after modification of the sample.

In cases where the spectra before and after the modification are not both accessible, for example in the study of native oxide layers on semiconductors, a different route has to be taken to gain the desired information. In their study on the concentration of surface hydroxyl groups on metal oxide films, E. McCafferty and J. P. Wightman^[124] used an analysis method that allows determination of the oxide layers on top of metal substrates from a single spectrum. A schematic presentation of such a system is shown in Figure 2.9. The following expression, which is ultimately based on the rather simple equation employing the exponential dampening of signals arising from a certain depth in XPS experiments given above, yields the oxide layer thickness:

$$d = \lambda_{\text{mo}} \cdot \cos(\vartheta) \cdot \ln \left[\left(\frac{D_{\text{m}} \cdot \lambda_{\text{m}}}{D_{\text{mo}} \cdot \lambda_{\text{mo}}} \right) \cdot \left(\frac{I_{\text{mo}}}{I_{\text{m}}} \right) + 1 \right] \quad (2.11)$$

In this equation, d refers to the thickness of the oxide layer, λ to the IMFP for the corresponding kinetic energy of the electrons, ϑ to the detection angle, D to the atomic density and I to the measured intensity; the subscripts “m” and “mo” refer to the metal and metal oxide, respectively. The same method was used by Strohmeier^[125] in work on aluminum alloys.

A very interesting feature of this analysis method is that, in favorable cases, even buried layers can be investigated within the limitations of XPS; the favorable condition needed for such studies being similar kinetic energies of the electrons from the two different species under investigation. Then, the signal for both species is damped to (nearly) the same extent by a common adlayer, e.g. a carbonaceous

contamination. As the equation relies solely on the intensity ratios, the value for the layer thickness is not affected at all by the additional layers.

Despite the huge advantage this analysis method provides in requiring only one spectrum, it is only useful for well known systems, because a number of not readily available parameters such as the atomic density for different species and the inelastic mean free paths are needed with sufficiently high accuracy.

One important information for an interface resulting from deposition of a metal onto a semiconducting polymer is certainly the width or extent of the interface, i.e., the depth up to which the dosed calcium atoms diffuse into the polymer. As the interface is characterized by a certain species, the reacted sulfur in the case of calcium adsorption on poly(3-hexylthiophene) (P3HT), the situation is not very much different from the oxide layer determination on a metal explored by McCafferty and Wightman. However, as the parameters necessary for the evaluation of the spectra with respect to the interface thickness are often not well known, a common approach is to simplify as much as possible. In the case studied here, the two relevant peaks in the XP spectrum (reacted and unreacted sulfur for P3HT) are very close to each other, meaning that the respective photoelectrons have almost the same kinetic energies and thus almost identical IMFP values. Furthermore, the density of these species is very similar, in the example of P3HT the volume concentration of sulfur is considered to remain unaffected by adsorption of calcium atoms. As a result, the first factor in the logarithm in Equation (2.11) is equal to one. What remains is a very simple expression for the layer thickness, with the parameters being the measured intensity ratio between the two signals from the upper (I_{top}) and lower (I_{bottom}) layer, the detection angle ϑ and the IMFP λ in the top layer:

$$d = \lambda \cdot \cos(\vartheta) \cdot \ln \left(\frac{I_{\text{top}}}{I_{\text{bottom}}} \right) \quad (2.12)$$

2.3 Materials

After introducing the experimental set-ups employed in this work and the fundamentals of the different techniques, the most important materials used in this work shall also be addressed: the two investigated polymers, namely regioregular poly(3-hexylthiophene-2,5-diyl) (rr-P3HT) and poly[2-methoxy-5-(2-ethylhexyloxy)-1,4-(1-cyanovinylene)-phenylene] (CN-MEH-PPV).

Films of these polymers were produced by spin coating. In both cases, the polymer

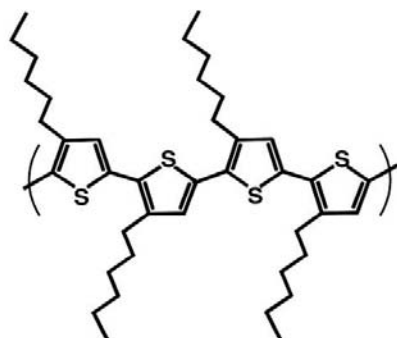


Figure 2.10: On the left: structure of regioregular P3HT in head-to-tail conformation; two repeat units which contain two thiophene units each are shown. On the right: photograph of rr-P3HT solution in chloroform utilized for spin coating.

was dissolved in chloroform to yield 0.3 % w/w (P3HT) and 0.5 % w/w (CN-MEH-PPV) solutions. The solutions were dropped on the samples at 1000 revolutions per minute (rpm). The rotational speed was kept constant at this speed for the first 30 seconds after applying the solution, before it was raised to 2000 rpm for an additional 90 seconds. The samples used for XPS experiments were spin coated on 0.1 mm thick aluminum foil, the samples for calorimetry experiments were spin coated directly onto sheets of the detector material (β -PVDF) sandwiched between metal tantalum plates. The tantalum plates served to increase the mechanical stability of the thin and wobbly β -PVDF sheet. A hole in the top plate served as a mask for the spin coating procedure, avoiding that the edges of the sheet are covered with the polymer film. Covering the edges of the β -PVDF sheet must be avoided, because this would effectively short the detector.

Solvents etc. were used without further treatment unless stated differently.

2.3.1 Poly(3-hexylthiophene)

The structure of rr-P3HT in a head-to-tail conformation is shown in Figure 2.10. Individual thiophene rings are attached to neighboring rings at the 2- and 5-position

as indicated by the name. This type of coupling is referred to as head-tail coupling. Coupling via the 2-2'-position or the 5-5'-position would result in a head-head or tail-tail conformation, respectively. One prominent and common structural property is that the hexyl side-chain points alternating in opposite directions.

The rr-P3HT used in this work was obtained from Sigma-Aldrich and comes as a black powder which is soluble in chloroform, trichlorobenzene, chlorobenzene, toluene and xylenes. Dissolving the black powder in chloroform results in an amber solution that can be used for spin coating samples. The certified purity of the polymer used in the experiments presented in this work is greater than 99.995 % with a regioregularity higher than 95 %. Typical trace metals in this polymer are iron, magnesium and nickel.

The molecular weight of approximately 30.000 atomic mass units (amu) corresponds to a mean length of a single polymer chain of 180 monomer units. Due to its electrical properties in combination with good solubility, processibility and environmental stability, P3HT has been widely studied.^[126–129]

The increased solubility with respect to unsubstituted polythiophene results from the alkyl substituents, here hexyl chains.^[128] Three different synthesis routes have been established: oxidative polymerization of 3-alkylthiophenes by oxidants such as ferric chloride (FeCl_3),^[130,131] nickel-catalyzed coupling of thiophene Grignard reagents^[132,133] and electrochemical polymerization.

In solution, the UV-vis spectra of rr-P3HT shows three maxima at 262, 456 and 607 nm. The fluorescence peak is located at a wavelength of 570 nm. In spin-cast films, UV-vis spectra exhibit two almost equally intense peaks at 556 and 610 nm and a shoulder at 526 nm.^[128] The band gap of rr-P3HT (head-to-tail) of 1.7 eV is considerably lower than the band gap of regiorandom P3HT, which amounts to 2.1 eV^[128], as determined by the isobestic point of the π - π^* transition in the absorption spectra.^[134,135] This difference is ascribed to the much greater conjugation length in the regioregular conformation. An electrical conductivity of as high as 100 S/cm has been reported for rr-P3HT films.^[136] The saturation field effect mobility in rr-P3HT based thin film transistors (TFT) is typically between $5 \cdot 10^{-3} \text{ cm}^2/\text{V} \cdot \text{s}$ and $3 \cdot 10^{-3} \text{ cm}^2/\text{V} \cdot \text{s}$. The mobility was found to increase with prolonged operation of such devices. Polarized absorption and micro-Raman spectroscopy experiments suggest that the reason for the increase in mobility is an increased interchain order of the polymer induced by the electric field applied during operation of the devices.^[137]

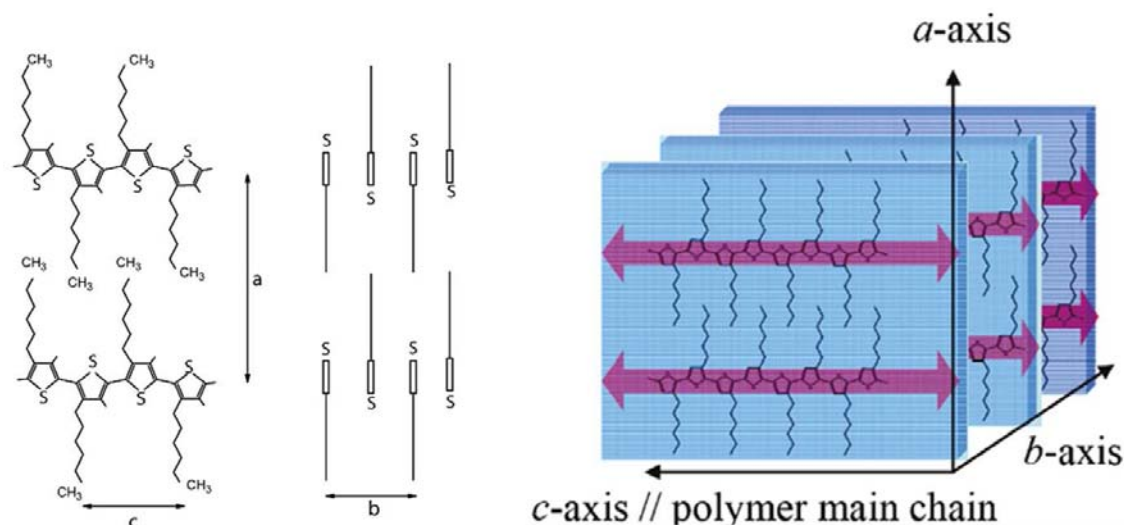


Figure 2.11: Schematic illustration of the layered structure of rr-P3HT with definition of the axes from Reference [138] (left) and Reference [137] (right).

Thin films of rr-P3HT from chloroform solution, either by drop casting or spin coating, generally show well-defined morphologies with fibrils indicating crystalline ordering. The fibrils consist of crystalline lamellae, as shown in Figure 2.11 with an interchain distance of 3.8 \AA (stacking distance between thiophene backbones, b -axis) and an interlamellar distance of 17 \AA (a -axis).^[139] Different orientations of the lamellae have been found, for example on SiO_2 , the a -axis was found to be normal to the substrate surface.^[138]

Concerning the thermal behavior, two temperatures are worth noting: the glass transition temperature at 65°C and the melting point at 238°C .^[140] Due to its favourable qualities, rr-P3HT is a suitable material for organic light emitting diodes (OLEDs) and solar cells. Under the brand name “Plexcore” it is sold in solution for inkjet-printing making use of its outstanding processibility for working devices. The manufacturer, Plextronics, promotes use of the polymer solution for the following applications: printed field effect transistors, plastic solar cells, printed memory, smart packaging, chemical and optical sensors, display and lighting backplanes, and smart textiles.

Konarka produces and distributes solar cells under the brand name “Power Plastic”. The already available products, some of those are depicted in Figure 2.12, demonstrate how the advantages of organic solar cells can be exploited in everyday products.



Figure 2.12: Examples for already available products making use of rr-P3HT (from www.konarka.com): Solar cells are integrated in parasols (left) and bags (right) providing the opportunity to charge mobile electronic devices such as cell phones or laptop computers.

2.3.2 CN-MEH-PPV

The structure of the second polymer used in this work, poly[2-methoxy-5-(2-ethylhexyloxy)-1,4-(1-cyanovinylene)phenylene] or CN-MEH-PPV, is shown in Figure 2.13. This is a cyano derivative of the electroluminescent poly-(p-phenylene vinylene) (PPV) ^[141] and emits light at a wavelength of 577 nm. ^[142] Due to its electrical qualities, it is used as an electron transport layer in organic LEDs, where it considerably increases the performance of devices. ^[143] Alike rr-P3HT, CN-MEH-PPV exhibits sufficient solubility in toluene and chloroform as to allow spin coating of films from such solutions. Especially the closed and uniformly thick films that can be prepared via spin-coating from toluene in combination with the ability to act as an electron acceptor render the material well-suited for use in two-polymer electroluminescent devices. ^[144]

PPV and its cyano derivatives such as CN-MEH-PPV find application in OLEDs and organic photovoltaic devices ^[141,145–148]. The schematic structure of an OLED employing indium-tin oxide (ITO) and calcium or other low work-function metals as electrodes is shown in Figure 2.14. Such devices show a good conversion efficiency, although a still better performance was expected. ^[149] In a double-layer configuration of PPV and CN-MEH-PPV with ITO and aluminum electrodes, a remarkable brightness of 1000 cd/m² at an operating voltage of 6 V has been observed. Such a red OLED showed a luminous efficiency of 2.5 lm/W, an internal quantum efficiency of 10 % and a lifetime of a few thousand hours. These characteristics meet the target

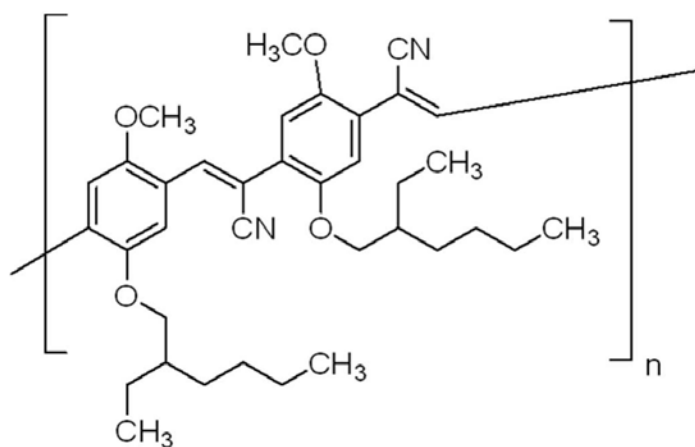


Figure 2.13: Structure of the repeat unit of CN-MEH-PPV.

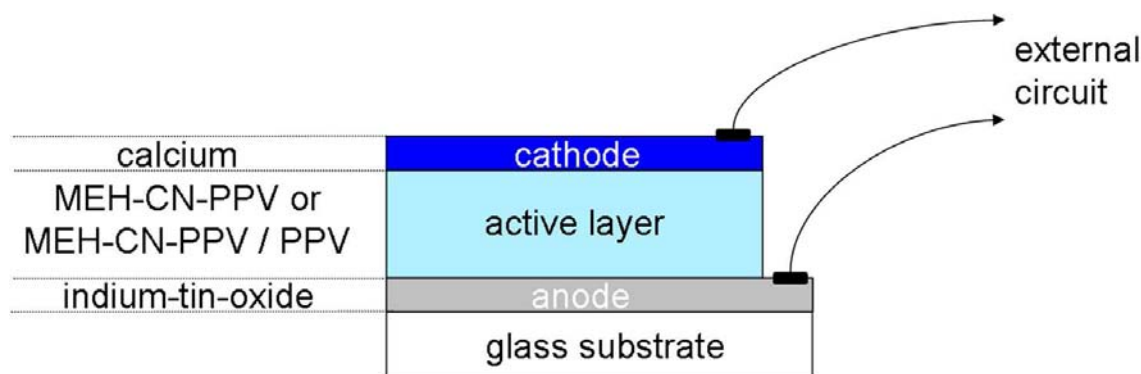


Figure 2.14: Schematic structure of an OLED along with common choice for the materials.

specifications for low-level backlighting and use in computer displays.^[146]

Despite its quite extensive use in organic electronic devices, work on the structural characteristics of CN-MEH-PPV is lacking. In an NMR study, Y. Li et al. proposed a reason for the limited performance of CN-MEH-PPV based devices normally present in trans configuration.^[149] They suggest that a substantial amount of cis-conformational segments is present in this polymer. Different from the effect of such segments on PPV, where it actually enhances the electroluminescence efficiency,^[150] it degrades the performance of CN-MEH-PPV. Large amounts of cis-segments may lead to a looser packing between CN-MEH-PPV chains compared to a purely trans-polymer. A loose packing should increase the probability for the CN-MEH-PPV to undergo a non-radiative relaxation via cis-trans- or trans-cis-isomerization of the

cyanovinylene group compared to the radiative relaxation from an electronically excited state. This explains the decrease in electroluminescence performance. More insights into the mechanisms responsible for limitations in the device performance and how to manufacture devices that are less affected by these will render this material even more interesting for future applications and devices. ^[149]

One route to synthesize CN-MEH-PPV is by Knoevenagel condensation and polymerization. ^[144] The CN-MEH-PPV used in this work was obtained from Sigma-Aldrich. The dark red powder was dissolved in chloroform yielding a clear, orange solution that was subsequently used to spin coat samples. Spin coating samples using 0.5 % w/w solution results in films with a typical thickness of around 100 nm as estimated from AFM line-scans over a scratch in a sample on a silicon wafer.

This thickness is suitable for a combination of calorimetry and XPS experiments, because the samples are thick enough to ensure bulk-like behavior of the samples and suppress any signal from the substrate in XPS, yet their heat capacity is sufficiently low and the thermal conductivity is satisfactory as to allow easily for calorimetric measurements.

3 Design of a Novel Single Crystal Adsorption Calorimeter

In the following sections, the design of a novel single crystal adsorption calorimeter currently being built in Erlangen is described. As an exhaustive description of the design of the calorimeter and all subsystems is far beyond the scope of this chapter, only the major differences and fields of improvement over previously constructed adsorption calorimeters are pointed out.

3.1 The Calorimeter Chamber

The calorimeter chamber as shown in Figure 3.1 is organized in three sections: two for calorimetry experiments and one providing space for various surface analysis techniques: XPS, AES, low energy ion scattering (LEIS) and low energy electron diffraction (LEED). Therefore, this section is labelled “surface analysis” in Figure 3.1. Within the individual sections, each port is oriented towards the center of the respective section.

The unique feature of housing two calorimeters in one chamber is motivated by the field of study the calorimeter is intended for: for a number of interesting systems, two successive deposition steps are performed and their energetics deserve to be studied with the highest precision possible.

One example for such a system would be the metallation of porphyrins, which has already been investigated in Dr. Gottfried’s group at the Chair for Physical Chemistry II (Prof. Steinrück) with other techniques.^[151–154] With the calorimeter presented here, both the adsorption of the porphyrins on the surface and the metallation process can be studied without breaking the vacuum. Experiments of this kind may give new insight into the mechanism of the metallation process, which is not completely understood up to now. In addition, the interaction of metallated porphyrin molecules with gases may be investigated further. For this system, too, spectroscopic and microscopic investigations have shown very interesting results,^[155,156] which may be complemented by calorimetry experiments. Here, the opportunity to

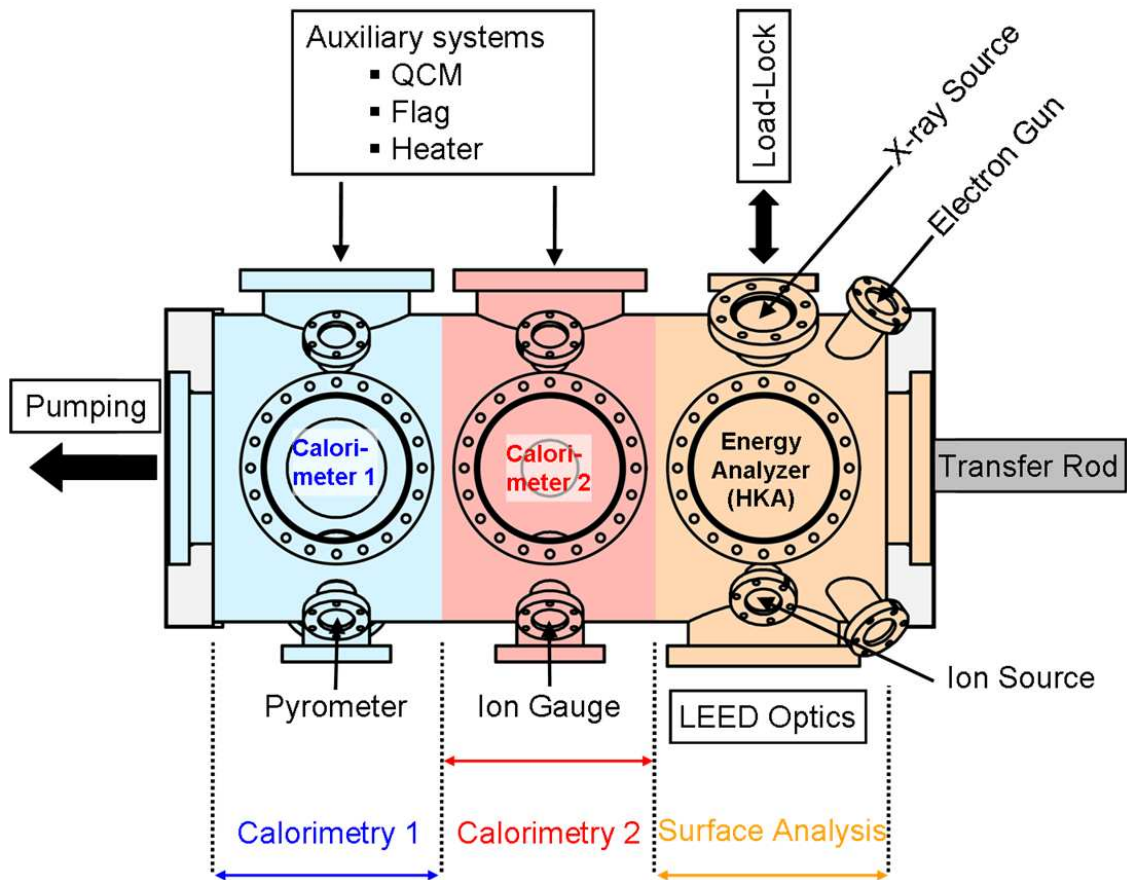


Figure 3.1: Top-view schematic diagram of the calorimeter. The three different sections (horizontally), two calorimeters and one surface analysis section are indicated as well as the purpose of the most relevant ports.

have two different types of beam sources, e.g., one for the deposition of a metal and the other for admitting a gas, is a tremendous advantage over the calorimeters used today in the groups of Campbell and King.

Another field of application for such a two-step experiment is catalysis: in the first step, a metal is deposited on an oxide support – Au on TiO_2 is a suitable example. In the second step, a gas is dosed on this system, for example carbon monoxide. The influence of the support on the active component is widely debated at the moment and such studies are bound to contribute to this discussion considerably.

The designated flanges for the calorimeters are on top of the chamber. This helps avoid lateral forces on the translation stage and the mount of the calorimeter which are problematic when the translational axis for the calorimeter is oriented horizontally. Then, the calorimeter is either prone to sagging and thus a less reproducible

positioning or a very bulky construction would be necessary to support the calorimeter sufficiently.

The calorimeter on top of the chamber requires that the beam source is mounted on the bottom flange pointing straight up. In this position, the whole capacity of the crucible in the beam source can be used (different from more horizontal orientations of the beam source) and inserting the refilled Knudsen cell is much easier.

Compared to the other calorimeters in use today, considerable more space was allotted for surface characterization and analysis. Recent studies have demonstrated the success resulting from a combination of adsorption calorimetry in conjunction with photo electron spectroscopy. In these studies, separate systems had to be used for calorimetry and photoelectron spectroscopy, respectively. The ability to conduct both types of experiments in the same chamber on the very same sample is very likely to increase the benefit from the combination of various techniques even further.

3.2 The Beam Chopper

A stepper-motor driven chopper (see Figure 3.3) is used to produce a pulsed atomic or molecular beam onto the sample from the constant flux provided by the Knudsen cell. In our setup, an arm with a U-shaped end resembling a two-pronged fork is used instead of a common chopper wheel (a wheel with a missing segment). The whole setup, motor and fork, are placed inside the beam chamber. Hence, there is no need for a motion feed-through. Furthermore, this chopper allows adjustment of the pulse-length independently from the repetition rate. A priori, one may expect a problem with this type of chopper: different from the chopper wheel that is rotating at a constant speed, the blade-type chopper is moved back and forth. As its center of mass is not even close to the axis of rotation, this setup is prone to create mechanical vibrations and accordingly noise from this source is visible in the detector signal. This problem can not be completely circumvented, but the angular momentum transmitted from the chopper and thus the noise can be minimized. To this end, the arm of the chopper is kept as short as possible and made from titanium in order to keep its weight low.

A similar level of control over the temporal characteristic of the beam is achieved in the setup by King with a piezoelectric crystal valve. However, this solution is only applicable for dosing gases and not metals. The chopper-wheel driven by an

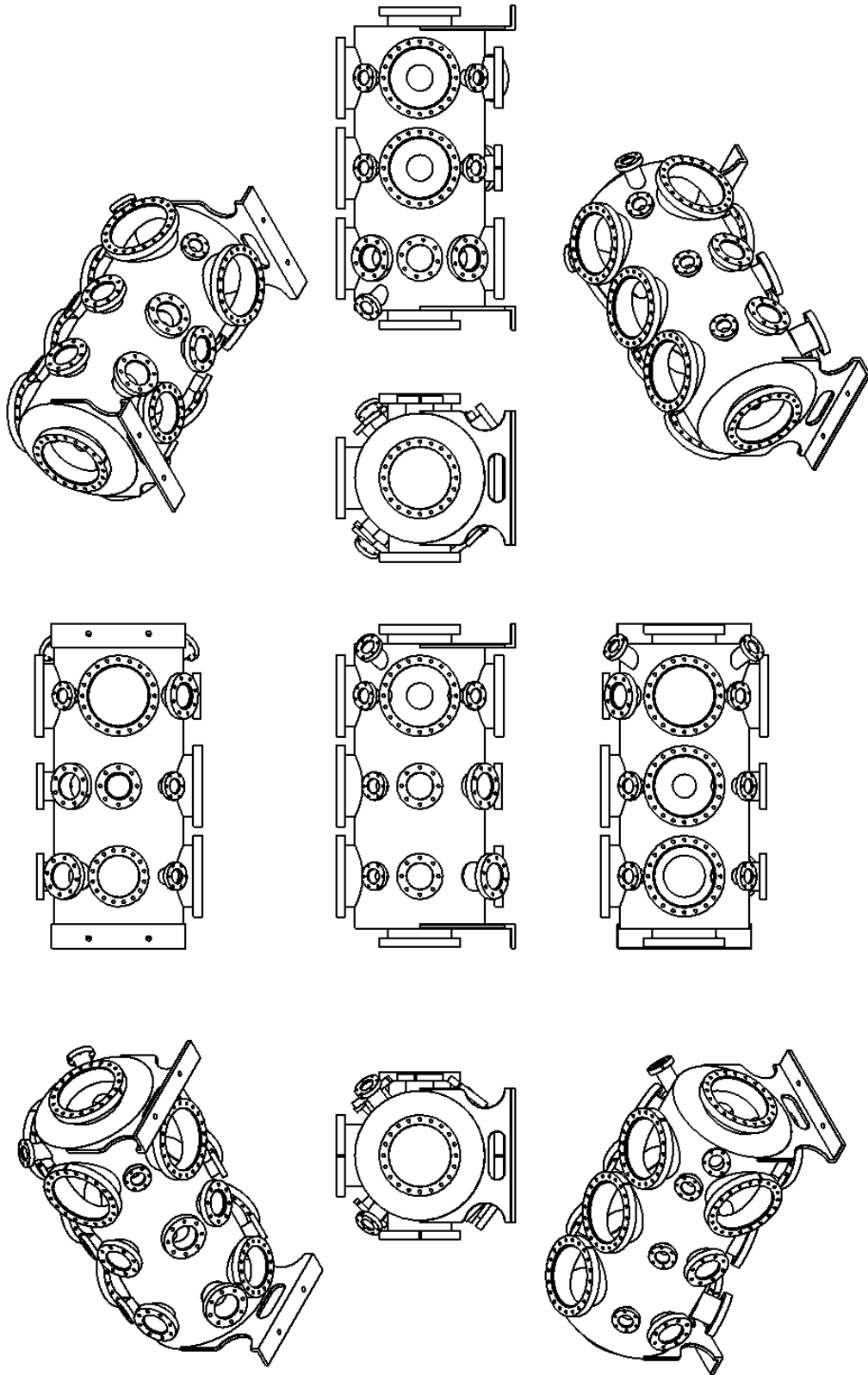


Figure 3.2: Several views of the main chamber.

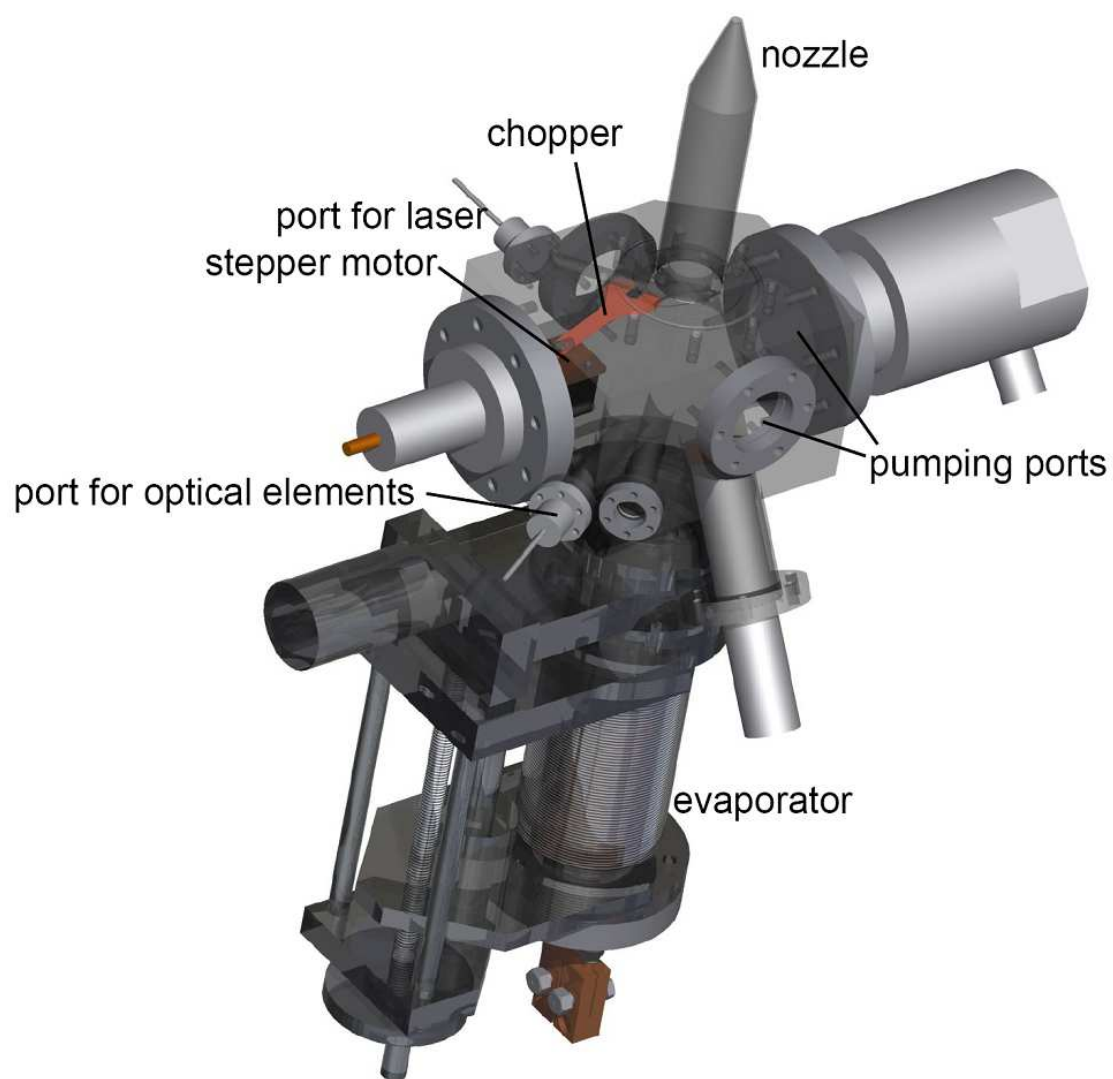


Figure 3.3: CAD drawing of the molecular beam source optimized for large organic molecules.

external motor in Campbell's calorimeter has a fixed ratio between the on and off times of the beam, but allows to dose metals. Another drawback of this solution is the susceptibility of the mechanical feed-through to failure, which entails a high down-time of the machine for maintenance. In conclusion, the new chopper concept employed in our setup in Erlangen is the attempt to combine the strength of both of these two systems and preliminary tests have given promising results.

3.3 The Beam Source

During the planning stage of the calorimeter, some attention was focused on the design of the beam source (a CAD drawing is provided in Figure Figure 3.3) and the requirements it must meet. The Knudsen cell has to provide high enough temperatures to create a suitably high vapor pressure, and thus a sufficiently high flux, to allow for calorimetry experiments. At the same time, the thermal radiation must be kept to a minimum in order not to disturb the experiment. In the newly designed calorimeter as well as in the prototype in Seattle, this is achieved via water cooled heat shields around the Knudsen cell.

As experiments involving large organic molecules planned in Erlangen are new with respect to the material dosed, the beam source must be adjusted accordingly. These adjustments include a very compact design in order to minimize the distance between Knudsen cell and sample. As large organic molecules are generally thermally less stable than metals, the cell temperature and correspondingly the vapor pressure are limited.

The only way to ensure a sufficiently high flux on the sample then is to place the Knudsen cell as close to the sample as possible (see also Section 2.1.2). For this purpose, the Knudsen cell is mounted on a z -translation stage. The placement of the Knudsen cell close to the sample is also of economical interest: the cost for evaporation materials may amount to several hundred Euros (e.g. ~ 600 € per gram for pentacene), or even more. In the pulsed beam, 95 % of the material dosed is not deposited on the sample, but on the chopper for typical 100 ms long pulses at a repetition rate of 0.5 Hz. Even more material is lost due the fact that only a miniscule portion of the material evaporated actually reaches the sample for pure geometric reasons. Considering the most simplified case, where the beam is not directed and the material from the cell is uniformly deposited in a hemisphere, the amount deposited on the sample is only around 0.9 % in our setup. Combining the

losses from pulsing the beam and the losses due to the distance, only about 0.04 % of the material dosed is actually used for the experiment. As the flux is inversely proportional to the square of the cell to sample distance, reducing this distance increases the percentage of material not wasted significantly, which is why a lot of effort was spent on optimizing the beam source.

Another design criterion for the beam source was that the cell must be refillable in a glove box. Here, the z -translation stage also plays an important role: the Knudsen cell can be retracted from the dosing position behind a gate valve. The beam section behind the gate valve can be removed from the chamber and docked to a glove-box, where the cell can be refilled under inert gas atmosphere. The z -translation stage is needed to gain access to the crucible from within the glove-box, as its load-lock chamber is too small to accommodate the whole beam section.

The opportunity to refill the cell under inert gas atmosphere and introducing the cell into vacuum without exposing the deposition material to ambient conditions is especially important for delicate materials: organic molecules that may react with water or oxygen or highly reactive metals like alkali and alkaline earth metals.

A specially designed and custom made in-line valve seals the main chamber, when the Knudsen cell is being refilled. The separation of the beam source from the main chamber in order to avoid frequent baking of the whole system is already widely used, of course. Usually, a gate valve mounted directly on the main chamber separates the beam source from the main chamber. Due to the compact design of the beam source in Erlangen, it was not possible to place a gate valve in between main and beam source chamber. Hence, a more complicated solution had to be devised: a sealing element made of copper on a z -translation stage is integrated into the setup. This element seals the flange on which the source chamber is mounted in the closed position without blocking any part of the molecular or atomic beam in the open position. Especially with the heavy geometric limitations, implementation of the separating valve turned out to be quite a challenge.

In order to determine the radiative contribution from the hot Knudsen cell to the calorimetry signal, a BaF_2 window may be used (see Section 2.1.2). However, this approach is sufficiently accurate only for metals, which can usually be deposited at high temperature and that often have a low emissivity in the infrared region. In such cases, the power irradiated in the far infrared region exceeding the transmission window of BaF_2 is very small and does not contribute to the heat signal significantly. For large organic molecules, the situation is completely different: these materials

usually show high emissivity in the infrared region and can not be heated to very high temperatures. The consequence is, that the power irradiated in the far infrared region beyond the transmission window of BaF₂ becomes too high to be neglected. As no material is transmissive enough in the far infrared region to be used as a window, a different way to determine the radiative contribution from the Knudsen cell to the heat signal had to be found. In contrast to materials that are highly transmissive in the far infrared region, highly IR reflective materials are readily available. Thus, an array of mirrors can be inserted into the beam path. Just like the BaF₂ window, this setup blocks the atomic/molecular beam from the cell, but allows the radiation to reach the sample. While the principle of this solution appears quite simple, the incorporation into the compact beam source proved quite difficult, as a two stage differential pumping system and optics for the laser calibration (see Section 2.1.3) also need to be contained in the small beam source chamber.

3.4 Thermal Design of the Calorimeter

The central part of the calorimeter is shown in Figure 3.4. A main aspect in the design of this part was thermal stability: the copper block serving as the thermal reservoir and the support for the sample during calorimetry experiments are made from copper. In order to enhance the thermal conductivity between the thermal reservoir and sample accommodation, copper braids are used in addition to the copper screws holding the support in place. Furthermore, also the housing of the detector itself and the sample holder are made of copper to ensure a uniform temperature in the surrounding of the sample. Thus, measuring the temperature of the sample accommodation close to the sample itself should be a fairly accurate way to determine the sample temperature. A second thermocouple on the thermal reservoir serves as an indicator that thermal equilibrium between the sample, more accurately, the sample accommodation, and the reservoir is established and experiments can be performed.

The detector housing is constructed in a way such that it self-aligns with the sample when it approaches the measurement position. This is achieved by giving the detector housing a conical shape and implementing a matching cavity in the back of the sample holder. As the detector approaches the sample, it is guided to always end up in the same position relative to the sample, as the detector is allowed a little movement off axis. This feature does not eliminate the need to calibrate the

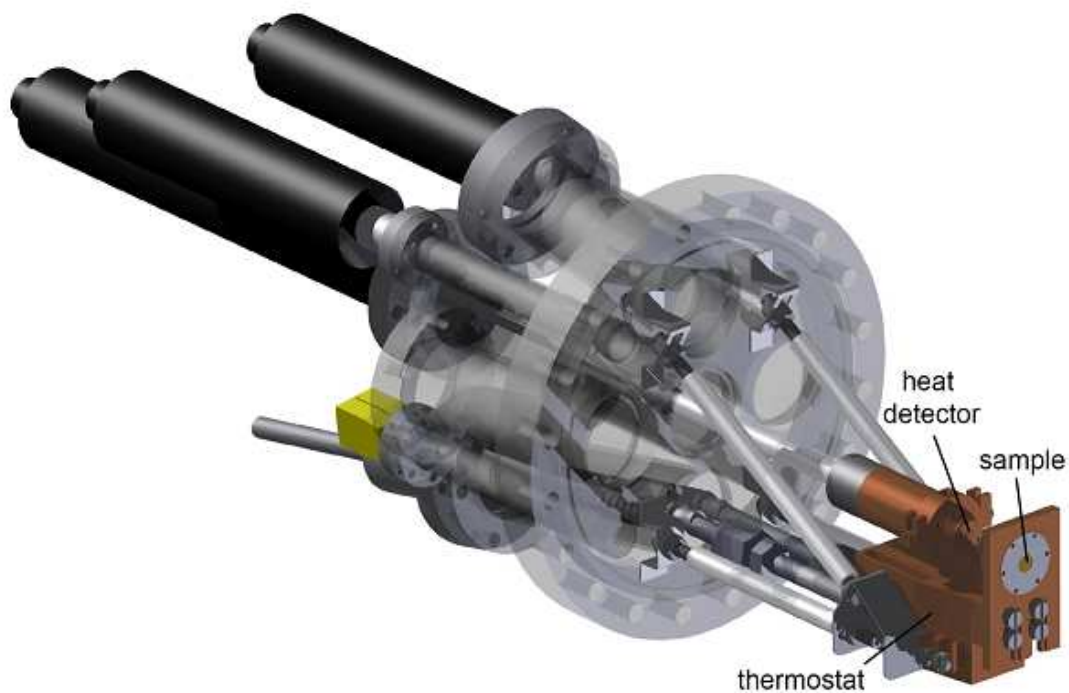


Figure 3.4: Central part of the Erlangen single-crystal adsorption microcalorimeter with heat detector and sample (top: photograph; bottom: CAD drawing). The electron beam heater and other elements have been omitted here for clarity.

calorimeter for every single experiment. However, as the thermal contact is quite reproducible, degradation of the detector polymer is much easier to recognize, as this then poses the main source of variation in the detector sensitivity.

The complete assembly of copper parts is supported by ceramic rods. These rods have a low thermal conductivity, which is necessary to reach maximum thermal stability at any chosen temperature. Their low thermal expansion coefficient is also advantageous in that the sample position is very little effected by the temperature at which experiments are conducted. Thus, a comparison between high and low temperature experiments is easy to accomplish. Of course, this is not connected to alignment of the detector to the sample. The detector is self-aligning, as pointed out above, but a change in the sample position may influence the flux of atoms or molecules onto the sample, as the beam source orientation is fixed and independent of the sample temperature. One may well account for a different flux in such experiments, however keeping the experimental conditions as similar as possible is certainly beneficial for the comparability of a series of experiments. Especially, as the deposition rate is known to have a profound influence on the growth mode of the deposited material, it seems advisable to aim for very similar conditions.^[157] This effect was also observed on recent studies on the deposition of Ca onto a semi-conducting polymer.^[115,158] A very helpful element worth mentioning is the mirror attached to same z -translation stage as the QCM and the zero-sticking flag (not shown in the picture). Alike the QCM, this mirror can be positioned at approximately the measurement position of the sample. It deflects the laser beam of the calibration laser to a window, where its intensity can be measured with a photodiode. This allows determination of the laser intensity impinging on the sample routinely, even at the beginning and end of every experiment. Without the mirror, a correlation between the laser intensity on the sample and the detector signal is only possible, when the chamber is vented and the photodiode can be placed at the sample position. As the incident laser power on the sample is, however, easily affected by minor misalignment of the laser, the opportunity to determine this quantity routinely will definitely improve the accuracy of the experiments.

4 Metal-Polymer Interfaces

The metal-polymer interface has been extensively studied for quite some time by now – the interest was high enough in 1987 for the American Chemical Society to arrange for a national meeting focused on metallization of polymers in 1989. ^[159] Widely used tools in studies concerning surface analysis of such interfaces include X-ray and ultraviolet photoelectron spectroscopy (XPS and UPS), near-edge X-ray absorption spectroscopy (NEXAFS), high-resolution electron energy loss spectroscopy (HREELS), and static secondary ion mass spectrometry (SIMS). Less popular in this context are elastic recoil detection (ERD) and techniques for trace element analysis like proton-induced x-ray emission (PIXE) and neutron activation analysis (NAA). The major strengths of the above mentioned methods with respect to metal-polymer interfaces are:

- Photoelectron spectroscopy proved to be a powerful tool in the study of interfacial chemistry. ^[159–162] With XPS, reactions taking place at the interface can be followed and the inequivalence of metal-on-polymer and polymer-on-metal interfaces could be demonstrated (see [159] and references therein).
- NEXAFS is a very powerful tool for determining molecular orientation, even of very complex systems, and bonding interactions. ^[159,163–165]
- HREELS, too, delivers information on the bonding interaction and on the adsorption geometry of, e.g., metal atoms deposited on a polymer. ^[159,166–168]
- SIMS yields depth-resolved information on the elemental composition. This is exploited in studies involving diverse modifications of polymer surfaces: ion-beam or plasma induced changes, as well as changes brought about by simply depositing metals. ^[159]

Electron microscopy, especially transmission electron microscopy (TEM), and atomic force microscopy (AFM) also are valuable tools for the investigation of the morphology of (metallated) polymer surfaces. ^[159,169]

Similar to the wealth of tools for investigating the metal-polymer interface, an almost equally large tool-set for the modification of polymer surfaces and interfaces has been known for a substantial amount of time. In the above cited older work many studies are concerned with polyimides, which were used in microelectronic devices as insulating materials due to their high tolerance against harsh (production) environments.^[159] In order to use the polymers more efficiently for this kind of application, it was highly desirable to increase the metal-polymer adhesion, as to allow for fabrication of more durable devices. Among the most common routes to modify polymer surfaces to achieve a higher adhesion are ion- and electron-beam irradiation^[170] and plasma treatments.^[169,171,172] Changes to the polymer may also be caused by laser^[173] and UV light irradiation or thermal treatment^[159], in these two cases the resulting modifications are generally considered detrimental as they may ultimately damage or destroy the interface.^[127] With respect to metallization, also the substrate temperature during deposition and the deposition rate of the respective metal were shown to have an influence on the interface morphology.^[170] Despite the wealth previous investigations, the energetics of the formation of polymer-metal interfaces remained a matter of not well-founded conjectures. Therefore, the processes leading to adhesion of metal films on polymers could not be readily related to an observable and attempts to improve metal adhesion were only poorly guided by previous findings. Particularly, it remained questionable whether metal evaporation could actually lead to the formation of metal-polymer bonds, as the corresponding deposition or impact energy of the metal atoms is very low (around 10 kJ/mol^[174]) compared to sputter deposition (950 kJ/mol^[175]), for example. In a simple picture, one would expect that the activation energy for a reaction between polymer and metal is on the order of the energy of covalent bonds (340-400 kJ/mol) and therefore a reaction accordingly unlikely to occur in the former case.^[159] More recently, the interest in polymers has shifted to semiconducting, π -conjugated polymers, such as derivatives of poly-(phenylene-vinylene), polyfluorene and polythiophene. The reason for the particular interest in this class of materials lies in their suitability for fabricating organic electronic devices. An incomplete list of such devices includes organic light emitting diodes (OLEDs)^[141], photovoltaic cells^[176], photodiodes, field effect transistors^[177-179] and solar cells^[180-184]. All of these applications carry a high technological and economical potential and, in contrast to the older work, the polymer is the active component in such devices. They all have in common that metal contacts, and thus metal-polymer interfaces play a very decisive

role here, as well.

As an exemplary case, one of the best electrode/polymer combinations in terms of performance in solar cell applications is considered: Ca on regioregular poly(3-hexylthiophene) (rr-P3HT). Usually, the devices are made with an Al film on top of the Ca electrode to prevent degradation of the Ca-P3HT interface. Quite extensive studies have been performed on this system, including XPS [160,161,185] and LEIS [186] studies. It is known that the bonding situation there, although widely unknown in detail, strongly influences the rates of charge injection.^[5] The bond strength has only been discussed on the basis of indirect information such as photoelectron and vibrational spectra (which show adsorption-induced changes of the electronic structure or the vibrational frequencies) as well as adsorbate-substrate bond distances (from X-ray standing wave (XSW) experiments) so far. In this work (Chapter 5), the first experimental investigation directly probing the energetics of the interface formation of Ca deposited on rr-P3HT is presented, along with structural (LEIS) and chemical (XPS) analyses. The difficulty in the study of the energetics of the interface formation is caused by the irreversible nature of the adsorption process, e.g., the use of classical desorption based techniques is ruled out. Only recent advances in adsorption calorimetry have made it possible to study the interfacial energetics directly, providing now thermodynamic information of general interest for a broad range of metal/polymer systems.

The modification of polymer surfaces prior to metal deposition aiming at optimizing device performances is already a well-established field, as such studies have been performed on insulating polymers before (see above). Even today, the most commonly used routes for such modification remain plasma treatments^[187–189] to tune the surface free energy, and electron-^[190–193] and ion-irradiation^[194–196] for the chemical modification of polymer surfaces. These procedures have the goal to improve the interface quality by reducing stress between the metal film and the substrate or to improve the adhesion. In Chapter 6, the calorimetric investigations are extended from the unmodified to electron-irradiated rr-P3HT surface. The combination of calorimetry with XPS, LEIS and surface scattering substantially improved the understanding of the changes induced by electron-beam irradiation, which was previously studied employing mass spectrometry by Massey and coworkers.^[191] Yet another way to influence the interface is the substrate temperature during deposition. Strunskus et al. noted that a very sharp interface could be obtained at low temperatures.^[170] However, a demonstration of this effect has not been shown in the

literature, at least not in the sense that the interfaces created at low temperature sustained its sharpness after being heated to room temperature. In contrast, the opposite effect that elevated temperatures facilitate diffusion and consequently lead to a larger thickness of the interfacial layer, i.e., the depth up to which metal atoms diffuse into the bulk of the polymer, is well known. ^[169] In Chapter 7, the first study on the formation of a sharp interface at low temperature with a sustained decrease of the interfacial layer thickness even at room temperature is presented.

5 Calcium Adsorption on Unmodified P3HT

The adsorption of Ca on poly(3-hexylthiophene) (P3HT) has been studied by adsorption microcalorimetry, atomic beam/surface scattering, X-ray photoelectron spectroscopy (XPS), low-energy He⁺ ion scattering spectroscopy (LEIS), and first-principles calculations. The sticking probability of Ca on P3HT is initially 0.35 and increases to almost unity by 5 ML (a monolayer of Ca is defined as the number of Ca atoms in a Ca(111) plane, $7.4 \cdot 10^{14}$ atoms/cm²). A very high initial heat of adsorption in the first 0.02 ML (625 kJ/mol to 500 kJ/mol) is attributed to the reaction of Ca with defect sites or residual contamination. Between 0.1 ML and 0.5 ML, there is a high and nearly constant heat of adsorption of 405 kJ/mol, which is ascribed to Ca reacting with subsurface sulfur atoms from the thiophene rings of the polymer. This is supported by the slow increase of the LEIS signal for Ca and the shift of the S 2p XPS binding energy by -2.8 eV for reacted S atoms. The heat of adsorption decreases above 0.6 ML coverage, reaching the sublimation enthalpy of Ca, 178 kJ/mol, by 4 ML. This is attributed to the formation of Ca nanoparticles, and eventually a continuous Ca(solid) film, on top of the polymer. LEIS and XPS measurements, which show only a slow increase of the signals related to solid Ca, support this model. Incoming Ca atoms are subject to a kinetic competition between diffusing into the polymer to react with subsurface thiophene units versus forming or adding to three-dimensional Ca clusters on the surface. At ~ 1.6 ML Ca coverage, Ca atoms have similar probabilities for either process, with the former dominating at lower coverage. Ultimately about 1.6 ML of Ca ($1.2 \cdot 10^{15}$ atoms/cm²) reacts with S atoms, corresponding to a reacted depth of ~ 2.6 nm, or nearly 5 monomer-unit layers. Density-functional theory (DFT) calculations confirm that the heat of reaction and the shift of the S 2p signal are consistent with Ca abstracting S from the thiophene rings to form small CaS clusters.

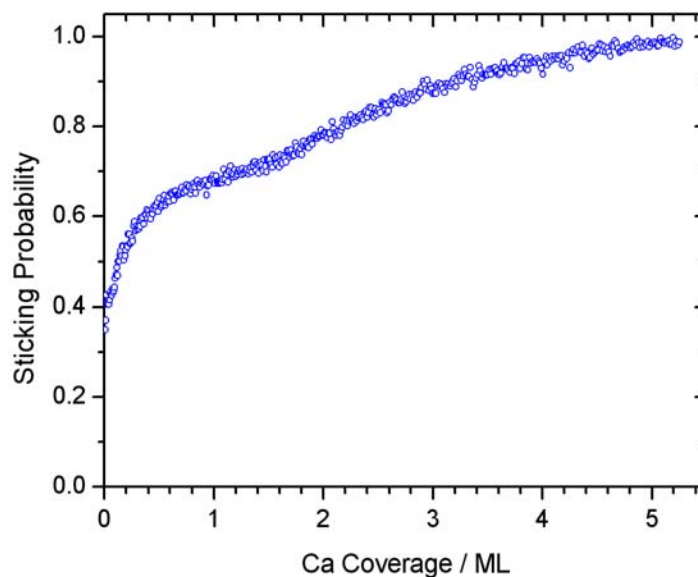


Figure 5.1: Sticking probability of Ca on a P3HT film at 300 K plotted as a function of Ca coverage. Monolayer coverage (1 ML) is defined as $7.4 \cdot 10^{14}$ Ca atoms per cm^2 (the Ca(111) packing density).

5.1 Results

5.1.1 Sticking Probability

In order to determine the amount of Ca that actually adsorbs on the P3HT surface and causes the heats of adsorption and reaction measured by microcalorimetry, the sticking probability of Ca on P3HT must be known. Figure 5.1 shows the sticking probability as a function of Ca coverage at 300 K. The curve is the average of three independent, yet highly reproducible experiments. Three distinct regimes can be identified. In the low coverage regime, the sticking probability increases rapidly from an initial value of 0.35 to 0.6 at a coverage of 0.5 ML. In the range of intermediate coverages between 0.5 ML and 1.5 ML, the curve is less steep and a sticking probability of 0.7 is reached at 1.5 ML. Above 1.5 ML, the sticking probability further increases with a steeper slope until it asymptotically approaches unity around 5 ML. Note that all coverages reported in this work refer to the amount of Ca that is actually adsorbed on the surface. These coverages are calculated by multiplying the Ca dosage – the flux of the atomic beam multiplied by the deposition time – by the sticking probability integrated over the total dosage.

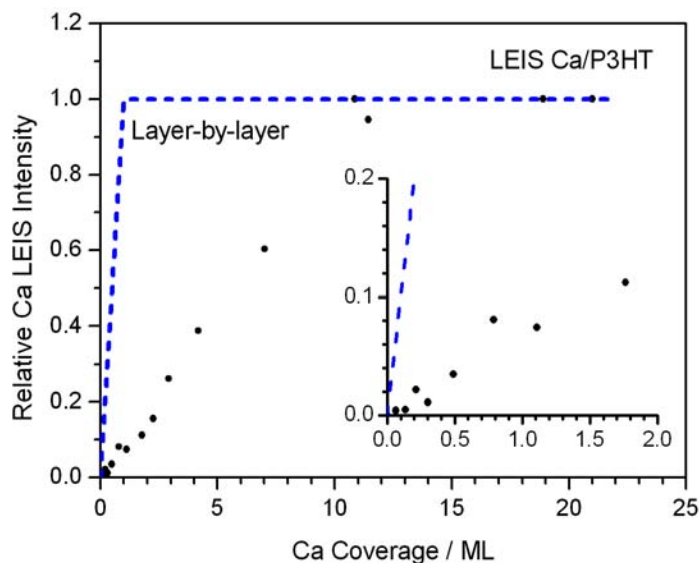


Figure 5.2: The relative integrated Ca LEIS peak intensity as a function of Ca coverage on P3HT at a sample temperature of 300 K, with all intensities normalized with respect to the saturation signal obtained for high Ca coverages. The blue dashed line indicates the expected trace for layer-by-layer growth. The inset shows a blow-up of the low-coverage region.

5.1.2 Low-energy Ion Scattering (LEIS)

Metal films growing on polymer surfaces form a variety of structures, including three-dimensional (3D) particles and continuous films. In addition, diffusion of the metal atoms to the subsurface region and reaction with functional groups of the polymer have been observed.^[120,170,197–199] Knowledge of the growth mode is, therefore, an essential prerequisite for interpreting the measured coverage-dependent heats of adsorption. LEIS with He^+ ions provides a valuable tool for the evaluation of the growth mode of Ca on P3HT, because it is element-specific and extremely surface-sensitive, that is, it probes only the topmost atomic layer. Figure 5.2 shows the evolution of the normalized LEIS peak intensity of Ca as a function of Ca coverage with the inset displaying the low coverage regime in more detail. Ion beam damage was proven not to be influencing this curve by repeating measurements at several Ca coverages with ~ 3 -fold less ion exposure. In these experiments, no differences could be detected with respect to the ones with normal ion dose. The data reveal that the intensity of the Ca signal increases approximately linearly until saturation is reached around 11 ML. For comparison, a dashed line representing the layer-by-layer growth mode is displayed. The much slower growth of the observed

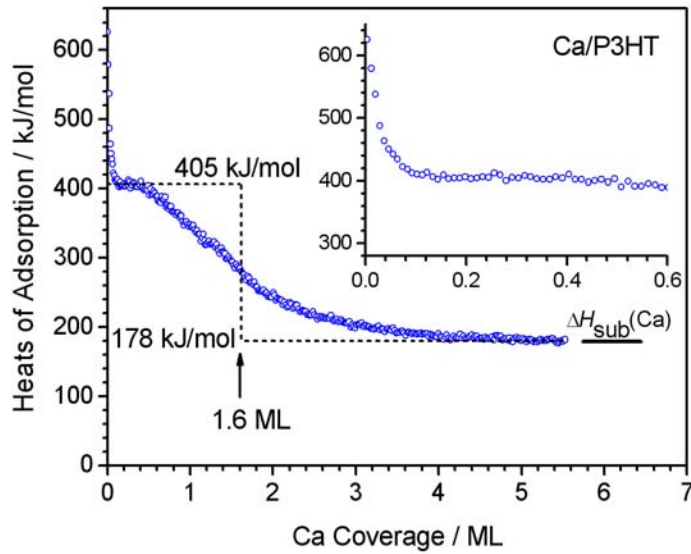


Figure 5.3: The differential heat of adsorption of Ca atoms on a rr-P3HT surface as a function of Ca coverage at 300 K. The inset shows an enlarged plot of the low-coverage range. The dashed line refers to a two-site model for Ca adsorption that is explained in the text. On the right hand side, the sublimation enthalpy of Ca, $H_{\text{sub}}(\text{Ca})=178$ kJ/mol, is displayed.

Ca peak intensity is consistent with 3D island growth resulting in tall, large Ca islands, which eventually coalesce into a continuous film around 11 ML, combined with diffusion of Ca atoms into the subsurface region of the polymer film at low Ca coverages. Note that since this curve would have the same qualitative behavior with or without this added subsurface diffusion, the LEIS data alone does not prove subsurface diffusion.

5.1.3 Heats of Adsorption

Figure 5.3 presents the differential heat of adsorption of Ca on P3HT averaged over three experimental runs at 300 K as a function of coverage. These measured heats represent the standard enthalpies at 300 K. The inset shows the low-coverage region (0 to 0.6 ML) in more detail. The pulse-to-pulse standard deviation of the heats of adsorption at high coverages, where the heat is independent of coverage, is less than 2 kJ/mol for a pulse size of approximately 0.01 ML.

As can be seen, the heat of adsorption drops very quickly from an initial value of 625 kJ/mol to ~ 405 kJ/mol, where it remains almost unchanged in the coverage range between 0.1 ML and 0.6 ML. Beyond 0.6 ML, the heat of adsorption starts

to decrease and, above 4 ML, asymptotically approaches the absolute value of the reported bulk heat of Ca sublimation ($\Delta H_{\text{sub}}=178$ kJ/mol) ^[200] to within 2 kJ/mol. This agreement confirms the absolute accuracy of our heat and flux calibrations. The sharp decrease in the heat of adsorption occurring at very low coverages (0 to 0.05 ML) is indicative of a small concentration of adsorption sites on the P3HT surface (or in the near-subsurface) that bind Ca very strongly. These sites may originate from impurities such as residual chloroform or adsorbed water, or intrinsic surface defects. Based on the calorimetry data, the number of such sites is very low (<0.05 ML), which is consistent with the fact that they were not detected by XPS. After these few sites are saturated, Ca adsorbing on P3HT releases a heat of adsorption of about 405 kJ/mol. This suggests a strong interaction between Ca and some site on or below the polymer surface, as this heat is much higher than that of Ca adsorbed on Ca (178 kJ/mol). From the appearance and growth of a strongly shifted S 2p XPS peak (see below) that correlates in coverage with this high heat, we conclude that weakly adsorbed Ca diffuses to the subsurface and preferentially binds to the sulfur atoms in the thiophene rings. Thus, the relatively high heat of adsorption at low and medium coverages reflects the chemical interaction between Ca and the S atoms. Above 4 ML, the curve reaches the heat of sublimation of Ca, indicating that adsorbing Ca atoms are added to large, bulk-like 3D Ca particles. The smooth decrease of the heat of adsorption between 1 ML and 4 ML indicates that both processes occur simultaneously and that the formation of 3D Ca clusters becomes predominant as the coverage increases.

The heat of adsorption trace implies in conjunction with the sticking probability data that Ca initially populates a very weakly bound, transient adsorption state (precursor). ^[201] In this precursor state it can rapidly diffuse across and possibly into the polymer subsurface, or desorb again if it does not find a stronger binding site or if the reaction with this binding site is not successful because of an activation barrier. Such a weakly bound transient species is expected, since the interaction of Ca with the dominant CH₂, CH and CH₃ groups of the polymer (these groups are most probably exposed on the surface to minimize the surface energy ^[202]) is only very weakly attractive. This precursor state and the kinetics of the different reaction pathways will be discussed in more detail in Section 5.2.4.

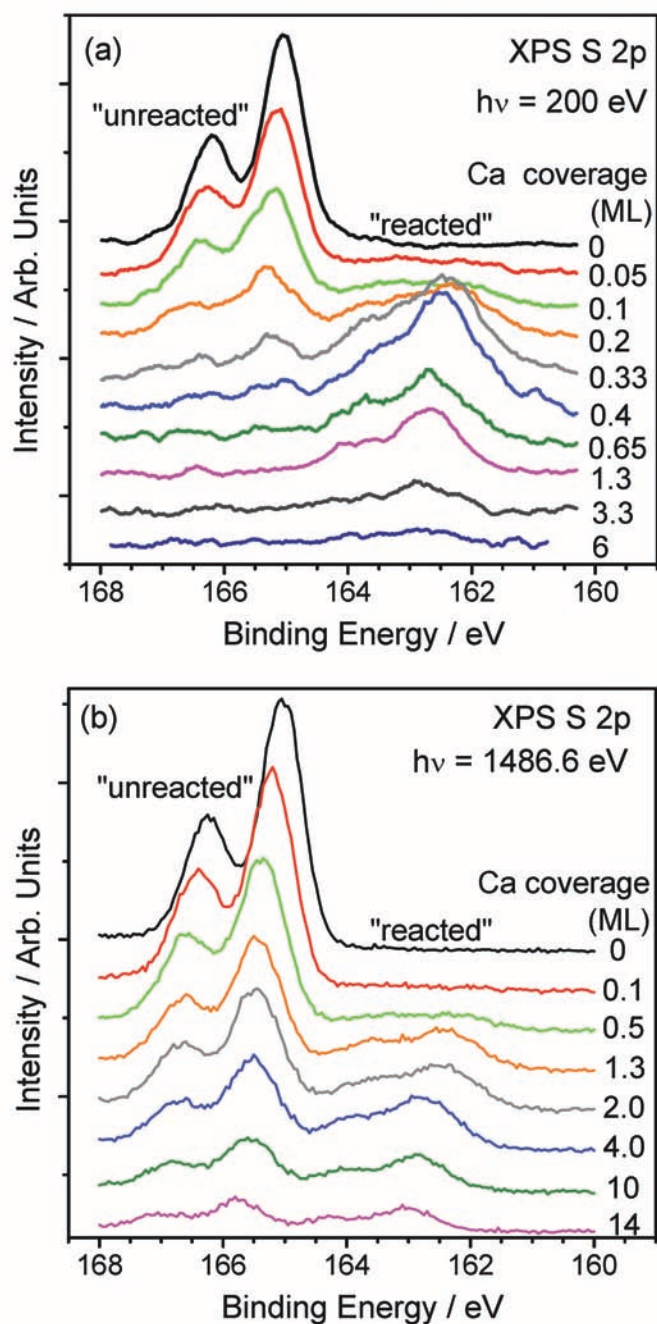


Figure 5.4: XP spectra of the S 2p region for different Ca coverages on P3HT recorded with photon energies of (a) 200.0 eV^[53] and (b) 1486.6 eV.

5.1.4 X-ray Photoelectron Spectroscopy

Figure 5.4a shows high-resolution XP spectra of the S 2p region for various coverages of Ca on P3HT. The spectra were recorded using synchrotron radiation with a photon energy of 200 eV. The spin-orbit splitting of the S 2p peak is well resolved with a spacing of 1.2 eV; the respective binding energies (165.0 eV and 166.2 eV) agree well with previous experimental results.^[160,161] Upon Ca deposition, two significant changes can be observed in the spectra, (a) damping of the original S 2p signal of pristine (“unreacted”) P3HT and (b) the appearance of a new doublet shifted by 2.8 eV towards lower BE relative to the original S 2p signal. The signal of pristine P3HT disappears for Ca coverages above 1.3 ML while the new feature (of “reacted” P3HT) can still be detected, albeit with very low intensity, at the maximum coverage reached in this experiment (6 ML). For comparison, the results of a similar experiment using a monochromatized Al-K α source ($h \cdot \nu = 1486.6$ eV) are shown in Figure 5.4b. Here, the kinetic energy (E_{kin}) of the S 2p photoelectrons and, consequently, their inelastic mean free path (IMFP) are significantly higher than in the above experiments with 200 eV photons. As a result of the thus increased probe depth, the original S 2p signal of pristine P3HT is visible for all Ca coverages up to 14 ML. The different attenuation lengths for electrons in the two experiments provide information on the diffusion of Ca into the polymer, as will be discussed in Section 5.2.3.

With increasing Ca coverage, the positions of the S 2p signals shift considerably (up to around 0.5 eV at 10 ML coverage) toward higher binding energies. Since the same shifts are observed in the C 1s peaks (Figure 5.5), they are most likely due to downward band bending (mainly during the first ML of Ca deposition) associated with long-range electron donation into the polymer.^[203] Beyond this band bending, the C 1s signal is much less affected by the deposition of Ca than the S 2p signal, indicating that Ca predominantly reacts with the sulfur rather than with the carbon containing backbone of the polymer or its side chains. The Ca 2p signal (not shown) initially appears at a binding energy of 348.1 eV. With increasing Ca coverage, a shoulder arises on the low binding energy side, which grows into a peak located at 347.1 eV due to 3D Ca(solid) (at 14 ML). Thus, the Ca 2p signal of “reacted” Ca (that is, Ca that chemically reacts with the polymer) is shifted by 1.0 eV towards higher binding energy relative to the signal of pure Ca multilayers. Note that after correction for band bending, the shift is even higher, 1.5 eV.

The changes of the C 1s and the S 2p peak intensities as a function of Ca coverage

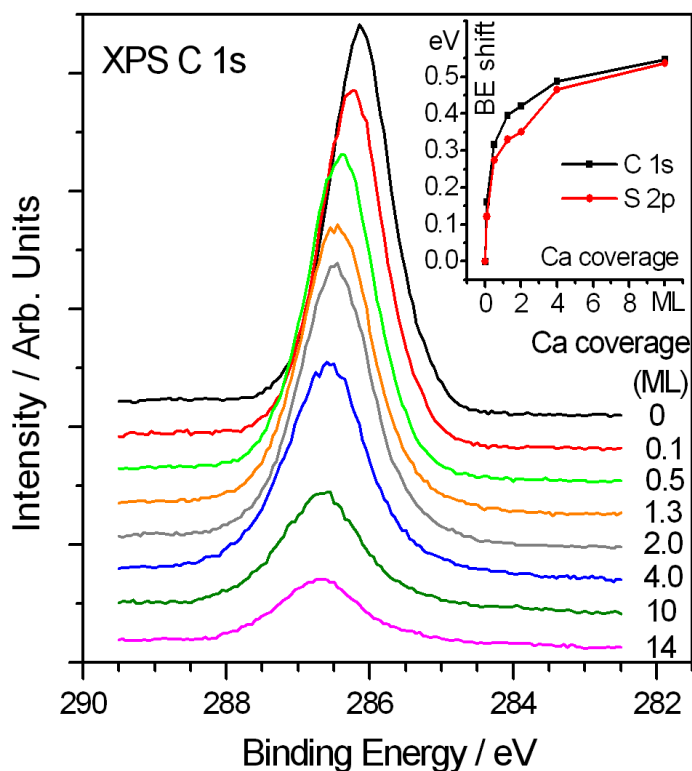


Figure 5.5: C 1s XP spectra of Ca adsorbed on P3HT, recorded with a photon energy of 1486.6 eV. Inset: Binding energy shift as a function of Ca coverage for the S 2p Figure 5.4b and C 1s signals.

are plotted in Figure 5.6 for the spectra taken at 1486.6 eV. The figure also shows the separate intensities of the “reacted” and “unreacted” S 2p peaks, as well as their ratio (inset). The intensity of reacted S increases up to 4 ML Ca, above which its intensity decreases due to Ca film growth on top. The reacted:unreacted ratio increases steeply up to a value of 0.75 at 4 ML Ca, after which the curve slowly approaches a saturation value near unity.

To ensure that these relative XPS intensities and lineshapes did not change significantly due to X-ray beam damage, XPS spectra of the polymer (before Ca and at some fixed Ca coverages) were taken with greatly decreased and greatly increased beam exposure times, with no significant changes besides the expected signal:noise differences.

5.2 Discussion

The experimental results can be summarized as follows:

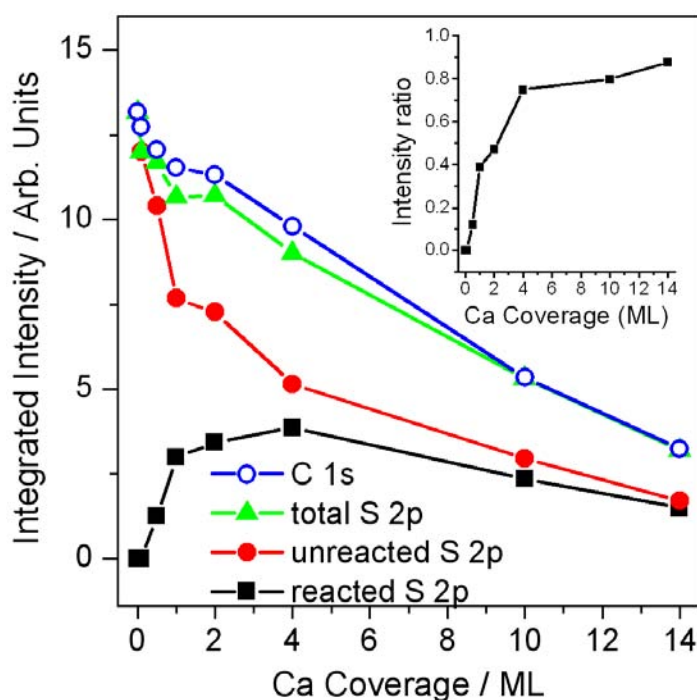


Figure 5.6: Normalized integrated intensities for the S 2p (Figure 5.4b) and C 1s (Figure 5.5) signals as a function of coverage. For S 2p, the intensities of the components for reacted and unreacted sulfur are displayed separately. Inset: ratio of the S 2p intensities of reacted and unreacted sulfur.

1. The heat of Ca adsorption on P3HT for low and medium Ca coverages (<4 ML) is very high (~ 405 kJ/mol) and much larger than the negative heat of Ca sublimation.
2. The LEIS intensity of Ca increases ten times more slowly with Ca coverage than expected for layer-by-layer growth.
3. Ca adsorption causes the appearance and growth of a new S 2p XPS peak, which is shifted by 2.8 eV compared to the unreacted portions of the polymer and correlates with the high (~ 405 kJ/mol) heat of adsorption, whereas the C 1s signal is much less affected.

In the following, a consistent model of the chemical state of the Ca/P3HT interface from these observations will be presented along with additional support for this model using DFT calculations.

5.2.1 Growth Model of Ca on P3HT

The LEIS data in Figure 5.2 show that the Ca signal increases much more slowly with Ca coverage than expected for the formation of a continuous first layer and subsequent layer-by-layer and/or three-dimensional (3D) growth. Rather, the data are consistent with 3D growth from the beginning or with diffusion of parts of the adsorbed Ca to the subsurface or bulk region of the polymer. In the first case, the heat of adsorption should approximately equal the negative heat of Ca sublimation, 178 kJ/mol (or less in the case of small clusters, due to the Kelvin effect^[204]). However, the measured heats of adsorption (Figure 5.3) are considerably higher than that for all coverages below 4 ML. Thus, the initial growth must follow the second scenario, that is, diffusion of parts of the adsorbed Ca to the subsurface or bulk region of the polymer (see below for an estimate of the diffusion depth), where a more exothermic reaction takes place than formation of Ca(solid). The decrease in the heat of adsorption between 1 ML and 4 ML shows that a growing amount of the adsorbed Ca contributes to the growth of 3D Ca clusters on the surface and that beyond 4 ML cluster growth is the dominating process. The LEIS data in Figure 5.2 show that these clusters coalesce around 11 ML, forming a continuous Ca(solid) multilayer film on the surface of the polymer.

5.2.2 Chemical Reaction between Ca and P3HT

The high heat of adsorption values at coverages below 4 ML (Figure 5.3) and the corresponding large S 2p core level shifts of -2.8 eV (Figure 5.4) indicate that there is a strong chemical interaction between Ca and P3HT. It is unlikely that such a large shift could be caused by a simple bonding mechanism whereby the Ca atom interacts with the S atom in the thiophene ring without breaking its S–C bonds. In addition, first-principles calculations (performed by the group of Dr. Hieringer at the University Erlangen-Nürnberg) of a Ca atom interacting with a thiophene molecule in the gas phase show that such an interaction leads to a bond energy of only 17.5 kJ per mole of Ca (MP2 level), which is not nearly as large as the experimental heat of 405 kJ/mol below 0.5 ML. Several such interactions on one Ca atom cannot combine to increase this heat to anywhere near 405 kJ/mol. For this reason, all interactions that do not involve bond cleavage in the polymer, combined with their replacement by stronger bonds, appear to be not adequate explanations for the observed heat of 405 kJ/mol.

Cluster Seize	ΔE in kJ/mol
(CaS) ₁	0
(CaS) ₄	-351
(CaS) ₃₂	-471
(CaS) ₁₀₈	-502
(CaS) _∞	-503

Table 5.1: Energies of CaS clusters (per mole of CaS units) relative to the energy of an isolated (CaS)₁ molecule, according to DFT calculations.

Therefore, it is suggested that a strongly exothermic chemical reaction is taking place that involves bond cleavage and formation. The strongly shifted S 2p peak indicates that this bond cleavage must be at the S atom of the thiophene. The most obvious possibility is that the Ca atoms abstract sulfur from the thiophene rings to form small clusters of CaS embedded in the polymer, and the two C atoms which lost their bonds to S form new C–C bonds. The simplest C–C bond formation mechanism is ring closure to form a cyclobutadiene ring, but this is probably too unstable. A more energetically favorable reaction would be that the C atoms from two nearby thiophene rings (which both lost their S atoms via abstraction by Ca) couple, resulting in polymer chain crosslinking. To obtain a crude estimate of the enthalpy of such a reaction, the simplest related reaction for which thermodynamic data are available is considered:



To estimate the heat of this reaction, the standard enthalpies of formation of Ca(gas) (177.8 kJ/mol), thiophene(liquid) (80.96 kJ/mol), CaS(solid) (-473.21 kJ/mol), and cyclooctatetraene(liquid) (254.5 kJ/mol) are used.^[200] From these values, the standard reaction enthalpy amounts to -604.7 kJ/mol, which is ~50 % larger than the measured heat of 405 kJ/mol in the plateau region below 0.5 ML in Figure 5.3. However, depending on their size, the CaS clusters in the polymer are expected to be less stable than bulk CaS(solid). To illustrate this size effect, the calculation of the standard enthalpy of the reaction according to Equation (5.1) was repeated, but the enthalpy of formation of a single CaS molecule, +123.59 kJ/mol,^[205] was used this time. The resulting reaction enthalpy is only -7.92 kJ/mol compared to -604.7 kJ/mol for the formation of bulk CaS(solid). Even considering that embedding the CaS molecule in the polymer matrix will make the reaction slightly more exothermic, the difference to the measured heat (-405 kJ/mol) remains very large.

This shows that neither single CaS molecules nor bulk CaS can be formed along with cyclooctatetraene, but small clusters of CaS. To obtain quantitative information about the size dependence of the energy of the CaS clusters, DFT calculations of the cluster stabilization energies ΔE relative to the energy of the isolated CaS unit were performed in the group of Wolfgang Hieringer (Table 5.1): As can be seen, the stabilization energy depends strongly on the cluster size for very small clusters, but approaches rapidly the value for the infinite crystal $(\text{CaS})_\infty$ for clusters larger than $(\text{CaS})_{108}$. Using the values in Table 5.1, we now relate the difference of 200 kJ/mol between the enthalpy of adsorption (-405 kJ/mol) and the calculated standard reaction enthalpy (-604.7 kJ/mol) to the reduced stability of small CaS clusters relative to bulk CaS. Table 5.1 shows that the $(\text{CaS})_4$ cluster is less stable by 152 kJ/mol than bulk $(\text{CaS})_\infty$ and, using interpolation, it is estimated that a $(\text{CaS})_3$ cluster is less stable by ~ 270 kJ/mol than bulk $(\text{CaS})_\infty$. Therefore, a destabilization of 200 kJ/mol is consistent with the formation of clusters which, on average, contain 3 to 4 CaS units. Considering this estimate, the assumed reaction (Equation (5.1)) is energetically consistent with the measured heats. There will be additional small energy differences associated with the fact that, in the real Ca/P3HT reaction, the thiophene and cyclooctatetraene units have their C–H bonds partly replaced by C–C bonds to neighboring units. The question arises of whether the CaS molecules are sufficiently mobile in the polymer matrix and on the time scale of the calorimetry signal (~ 0.1 s) to diffuse around and form clusters soon enough to have the heat of CaS–CaS bonding show up as part of the heat signal. Since no data for the mobility of CaS in P3HT are available, we will use data for other small molecules in other polymers for a rough estimate. For example, the diffusion coefficient, D , of CO_2 in poly(ethylene 2,6-naphthalene dicarboxylate) (PEN) is $4 \cdot 10^{-14}$ m²/s at 293 K. [206] According to the Einstein equation for the mean square displacement,

$$\langle x^2 \rangle = 2 \cdot D \cdot t \quad (5.2)$$

this corresponds to a mean displacement of ~ 90 nm within the ~ 0.1 s time-scale of the experiment. Since the mean distance between two neighboring S atoms in P3HT is only ~ 0.6 nm, the mobility should be more than sufficient for the formation of small clusters, even if CaS is less mobile than CO_2 due to its larger size and dipole moment.

Further support for the formation of CaS comes from a comparison of the observed S 2p XPS shifts (2.8 eV to lower binding energies upon reaction) and the computed

core-orbital energy shifts. According to the DFT calculations, the S 2p core orbital energies are shifted to lower binding energies by 2.4 eV to 4.1 eV with respect to gas-phase thiophene depending on the size of the CaS clusters considered. Larger clusters are characterized by smaller shifts (2.4 eV to 3.7 eV for $\text{Ca}_{32}\text{S}_{32}$, 3.6 eV to 3.8 eV for Ca_4S_4 , final-state effects not included).

The ~ 1.5 eV higher Ca 2p binding energy for the “reacted” Ca compared to the 3D Ca(solid) is also consistent with formation of small CaS clusters, if the less efficient screening in the clusters (as compared to the bulk materials) is taken into account. ^[207–209]

One might expect to notice stronger changes in the C 1s spectra due to the extraction of S from the thiophene ring than the corresponding spectra (Figure 5.5) show. However, the two C atoms attached to the S atom are of the type $-\text{C}=\text{C}-$ within a conjugated π -system and would remain so after losing the S neighbor, which in turn is replaced by a C–C nearest neighbor. The two types of C atoms are already present in the pristine polymer (along with aliphatic carbon) and thus their respective components are part of the C 1s peaks before any reaction with the Ca takes place. Thus, the proposed reaction is compatible with the observed lack of change in the C 1s spectra.

The combined calorimetry, XPS, and LEIS data suggest the following picture of the interaction between Ca and P3HT: Parts of the deposited Ca react with the thiophene units at the surface and in the surface-near bulk of the polymer. The reaction involves cleavage of the thiophene ring and formation of calcium sulfide as described above. Concurrently, and especially at higher coverages, 3D Ca islands are formed at the surface of the polymer, until the surface is completely covered with Ca at coverages above 11 ML. Thus, the decrease of the heat of adsorption between 0.6 ML and 4 ML can be interpreted as a superposition of the reaction (405 kJ/mol) and the formation of Ca clusters (178 kJ/mol, identical to the absolute value of the sublimation enthalpy). (There is also a very high heat, ~ 600 kJ/mol, at very low Ca coverages (< 0.1 ML), which we attribute to reaction with defects or impurities in the polymer and will ignore in the analysis below.)

The simplest approach for interpreting the heat of adsorption curve is a two-site model, ^[120] which includes sites with higher adsorption energy (405 kJ/mol, Ca interacting with the polymer S atoms) and other sites with lower adsorption energy (178 kJ/mol, adsorption of Ca onto 3D Ca particles). The step in the dashed line in Figure 5.3 is placed such that the integral under this curve is identical to the

integral under the experimental curve in the range above 0.1 ML. The position of this step indicates that approximately 1.6 ML Ca binds directly to S atoms of the polymer with a heat of 405 kJ/mol, whereas the rest of the Ca binds to Ca islands, releasing the heat of sublimation. The smooth heat curve is interpreted as due to a gradual transition between these two modes of bonding associated with a kinetic competition between Ca diffusing deeper and deeper below the surface to find S atoms, and Ca nucleating in clusters on the surface. The former process gets slower as the reacted polymer grows deeper, and the latter gets faster as more and larger Ca clusters are formed.

According to this two-site model, Ca binds exclusively to subsurface S atoms in the coverage range from 0.1 ML to 0.6 ML, where the Ca heat is nearly constant around 405 kJ/mol in Figure 5.4. The LEIS results show that only 1 % to 3 % of the surface is covered by Ca clusters in this coverage region. Thus, a tiny amount of the Ca is also appearing on the surface already, possibly as Ca clusters which contribute a lower heat (178 kJ/mol). Correcting the value of 405 kJ/mol for this possible contribution means that the true reaction heat with S may actually be $\sim 6\%$ higher, or up to 430 kJ/mol.

The model for the interaction between Ca atoms and P3HT presented above is, to the best of today's knowledge, an adequate one. However, there are two critical points that shall not be omitted from the discussion:

1. The DFT calculations suggesting that an interaction between intact thiophene units and Ca atoms could not possibly be strong enough to account for the observed high heats of adsorption were done on isolated P3HT units (as opposed to oligomers or polymers).
2. The dependence of the formation energy of CaS clusters on the cluster size gives quite a large window of 503 kJ/mol (computed value) to find a matching heat of adsorption value. Note that using experimental heats of formation results in an even larger window of 592 kJ/mol.

Concerning the first point, one has to realize that, due to conjugation, the lowest unoccupied molecular orbital (LUMO) of P3HT has a lower energy than the LUMO of an isolated thiophene molecule. Thus, there may be charge transfer from Ca to P3HT, but not to a single thiophene, because the LUMO energy of the latter is too high. Therefore, the calculations for Ca interacting with a single thiophene molecule are not truly representative for the real system. It is obvious that charge

transfer would lead to ionic interactions between Ca and polymer, which are much stronger than the interaction energies calculated for the isolated thiophene/Ca complex. Consequently, an alternative model for the Ca/P3HT interaction is suggested, in which the Ca atoms only donate charge to the polymer without breaking any covalent bond. Taking the large Ca induced shift of the S 2p signal into account, it may be speculated that the additional charge acquired by the P3HT is mainly localized at the sulfur atoms. This model is also consistent with the C 1s data, which show that Ca deposition hardly affects the carbon backbone of the polymer. The second point shows that essentially any measured heat of adsorption between 8 kJ/mol and 600 kJ/mol could be explained by cleavage of the thiophene units and formation of CaS. Thus, the conclusiveness of the argument based on the heat of adsorption alone is limited. However, the combination of all experimental results strongly supports the model presented above. The theoretical considerations support this model insofar as they do not contradict this model in any instance. Unfortunately, the system proved to be too complex to find direct support for the presented model in the calculations at this point.

5.2.3 Depth Range of Ca Diffusion and Reaction

In the following, the fact that the S 2p XPS measurements at different photon energies probe different depth ranges and thus provide complementary information about the depth up to which the Ca atoms diffuse into and react with the S atoms in the near-surface region of the polymer will be exploited.

The XP spectra in Figure 5.4a were taken at a photon energy of 200 eV, at which the kinetic energy of the S 2p photoelectrons ($E_{\text{kin}} \approx 34$ eV to 41 eV) is close to their minimum inelastic mean free path (IMFP), λ . This thus provides high surface sensitivity. Recognizing from the LEIS data that less than 10 % of the surface is covered by any 3D Ca particles below 2 ML of adsorbed Ca (Figure 5.3), it is a good approximation to use only the P3HT value below 2 ML Ca coverage and neglect the faster attenuation through the small amounts of 3D Ca. For the given energy range, we estimate $\lambda_{\text{P3HT}} = 0.18$ nm based on IMFP data for the structurally very similar poly(3-octylthiophene).^[210]

In contrast, the S 2p spectra in Figure 5.4b were taken with Al-K $_{\alpha}$ radiation, 1486.6 eV, which leads to much larger mean free path of the resulting S 2p photoelectrons ($\lambda = 4.8$ nm at $E_{\text{kin}} = 1320$ eV for poly(octylthiophene)).^[210] As a result, the signal of “unreacted” sulfur is now visible even at a large Ca coverage of 14 ML.

The thickness d of the layer containing exclusively “reacted” sulfur, i.e., the diffusion depth of the Ca atoms, is now calculated by comparing the intensities of the signals for “reacted” and “unreacted” sulfur, relying on the exponential damping of signal intensity at depth z below the surface. This is done via the formalism devised by McCafferty and Wightman already discussed Chapter 2.^[124]

$$d = \lambda_{\text{mo}} \cdot \cos(\vartheta) \cdot \ln \left[\left(\frac{D_{\text{m}} \cdot \lambda_{\text{m}}}{D_{\text{mo}} \cdot \lambda_{\text{mo}}} \right) \cdot \left(\frac{I_{\text{mo}}}{I_{\text{m}}} \right) + 1 \right] \quad (2.11)$$

with D denoting the atomic density of the probe element (metal there, but sulfur here), I the intensities, λ the inelastic mean free path of electrons, ϑ the emission angle and the subscripts “m” and “mo” referring to the metal and the metal oxide species, respectively. For the Ca-P3HT system, Equation (2.11) simplifies (for $\vartheta=90^\circ$) to:

$$d = \lambda \cdot \ln \left[\left(\frac{I_{\text{reacted}}}{I_{\text{unreacted}}} \right) + 1 \right] \quad (5.3)$$

where d is now the average depth of reacted S in the polythiophene. The concentration of Ca in the polymer is sufficiently low to justify the assumption that $\lambda \approx \lambda_{\text{P3HT}}$. Note that this model assumes that there is an abrupt interface between the reacted and unreacted polymer, which is probably not completely true when the reacted depth is large. However, the rapid decrease of the signal of the unreacted sulfur in the S 2p XPS data taken with 200 eV photons (Figure 5.4a) and the fact that for coverages exceeding 0.65 ML only the reacted species is visible in the spectra shows that a layer-by-layer reaction of the Ca with the polymer dominates at least for small reaction depths.

Figure 5.7 shows plots of this reacted depth of S versus Ca coverage estimated using Equation (5.3) and the reacted : unreacted S 2p intensity ratios from Figures 5.4 and 5.6. The data taken at the higher photon energy show that the reacted depth increases with Ca coverage up to ~ 3 nm. Since the signal of unreacted sulfur at $h \cdot \nu = 200$ eV becomes too small for an accurate estimate at higher coverages, no higher-coverage data are plotted for this experiment. Below 0.5 ML, there is good agreement between the data for both photon energies.

Another, independent estimate of the reaction depth can be derived from the simple two-site interpretation of the heat of adsorption measurements, which show that 1.6 ML of the Ca deposited reacts with the polymer at the highest Ca coverage (see above). This reacted Ca coverage can be converted to a reacted thickness, assuming that each reacted Ca atom binds one sulfur atom of the polymer, by using the mass

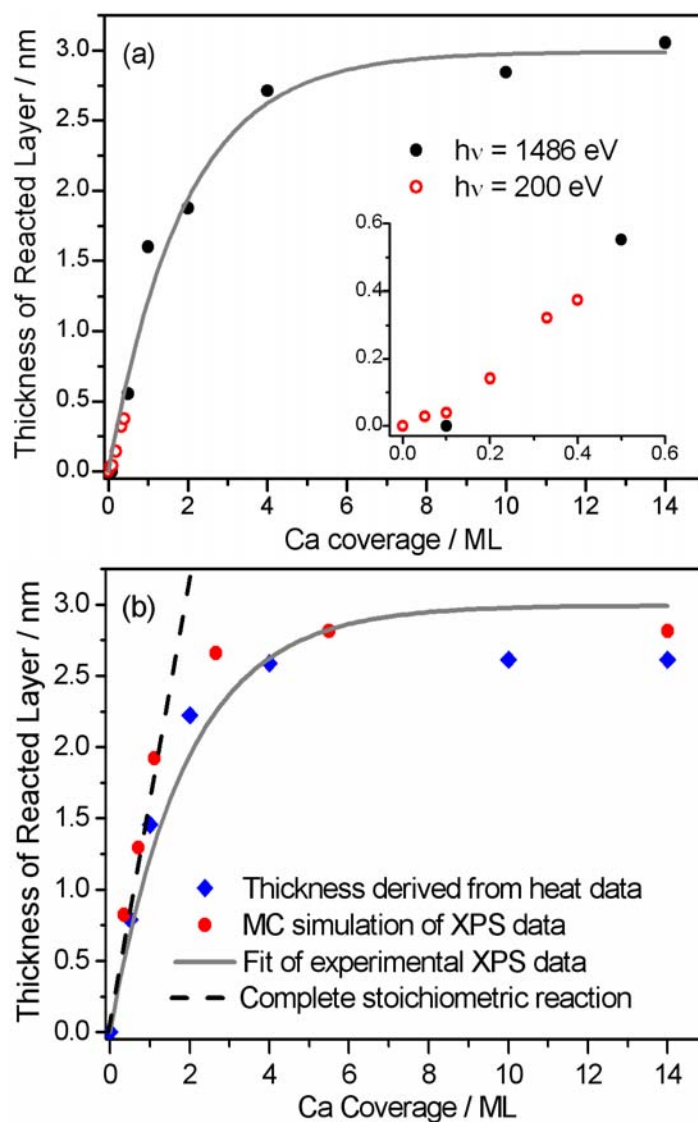


Figure 5.7: (a) Thickness of the reacted layer vs Ca coverage as extracted from the XPS data in Figure 5.4a (red open circles) and Figure 5.4b (black closed circles) using Equation (5.3). The grey solid line is an exponential fit with a function of the type $a(1 - \exp(-bx))$. The blow-up of the low-coverage range (inset) shows good agreement between the two data sets in the low-coverage range. (b) Blue diamond-shaped symbols: thickness of the reacted layer determined by analysis of the heat of adsorption data, based on the two-site model and assuming layer-by-layer reaction. This is compared to the results of the XPS data from Figure 5.7a (grey solid line) and Monte-Carlo simulations of the XPS intensities (red closed circles). The dashed line shows the hypothetical reaction depth for the case that all adsorbed Ca reacts stoichiometrically with the polymer in a layer-by-layer fashion. See text for further details.

density (1.33 g/cm^3)^[211] and the stoichiometry of the polymer. This reacted Ca coverage of 1.6 ML ($= 1.18 \cdot 10^{15} \text{ atoms/cm}^2$) corresponds to a depth of 2.5 nm at the highest Ca coverage, in excellent agreement with the value of ~ 3.0 nm obtained from the XPS data in Figure 5.7a.

To obtain the reacted depths for the lower coverages, we now apply the same type of two-state analysis of the heat data as described above for the highest Ca coverage. Figure 5.7b shows the results and compares them to the reacted depths derived from XPS. (Note that the integral heat of adsorption minus the heat of sublimation directly gives the amount of Ca in the stronger bonding state at each coverage.) The agreement with the XPS results is remarkably good. Also shown here for comparison is the reacted depth that would result if the adsorbed Ca reacted completely and stoichiometrically with the polymer in a layer-by-layer fashion (dashed line). The good agreement with both data curves at low coverages reveals that the Ca initially, below 1 ML, reacts indeed completely with the polymer. At higher coverages the formation of Ca clusters as the competing process becomes increasingly efficient.

This analysis was verified using the XPS simulation program SESSA by Smekal et al.,^[212] which performs Monte-Carlo simulations of the electron trajectories based on the partial-intensity approach for the electron-solid interaction.^[213] As input parameters, only the stoichiometry and the density (1.33 g/cm^3) of the material are necessary. Thus, this approach has the very important advantage that no assumptions about the IMFP of the electrons need to be made, as it will be determined as part of the simulation. The program SESSA was used to simulate the damping of the signal of unreacted P3HT by a layer of reacted P3HT, assuming again an abrupt interface between the two layers. The resulting curve (red open symbols in Figure 5.7b) shows good agreement with the data derived from the experiment and thus confirms the validity of our approach. (Note that the fraction of the deposited Ca that actually reacts with the polymer is needed to relate the total amount of deposited Ca to the thickness of the reacted layer. This fraction was determined using the calorimetric data as described above.)

In summary, the Ca coverage range over which Ca reacts with sulfur, as revealed by the heats in Figure 5.3, is very consistent with the range revealed by the XPS data taken at higher photon energy. Note that the LEIS data indicated the existence of a continuous Ca film on top of the polymer for coverages exceeding 11 ML, proving that this coverage indeed represents a Ca excess. It shall be pointed out here that the damping of S 2p intensities caused by any Ca overlayer does not

affect the above thickness calculation, because only the ratio of peak intensities of the two sulfur species was used, which are equally influenced by the Ca layer. The shape of the Ca sticking probability versus Ca coverage curve (Figure 5.1) can now be understood. The initial value of 0.4 corresponds to the intrinsic sticking probability of Ca on clean P3HT, which is small because of the very weak attraction of Ca to the dominant CH₂, CH and CH₃ groups of the polymer. Even if a Ca atom binds to these groups and enters a weakly-held mobile precursor state, it may desorb again before it finds a strong binding site, and this would appear as if it did not stick in this measurement. Furthermore, the highly exothermic reaction between Ca and thiophene under formation of CaS involves cleavage of C–S bond and therefore probably has an activation barrier. This would also lead to a reduced sticking probability. The initial, rapid increase in sticking probability from 0.4 to ~ 0.65 occurs in the first $\frac{1}{3}$ ML of Ca, which is approximately the amount of Ca required to react with the sulfur atoms in first layer of P3HT monomers. Thereafter, the sticking probability slowly increases from 0.6 to 0.7 up to ~ 1.4 ML, when the thiophene groups at the surface have already reacted and additional Ca is mainly reacting with thiophene groups deeper in the polymer. This broad coverage range of nearly constant sticking probability indicates that the intrinsic sticking probability of Ca is $\sim 0.65 \pm 0.05$ on fully reacted P3HT (i.e., P3HT in which the thiophene units have already reacted with Ca, presumably via a reaction analogous to Equation (5.1) above). Then, from 1.5 ML to 2.5 ML, the sticking probability increases more rapidly again as the growth mode of Ca becomes dominated by the growth of 3D Ca particles on top of the polymer. On the 3D Ca, the sticking probability is clearly higher than on the polymer, with or without subsurface Ca. Eventually, the surface is covered with a continuous overlayer of Ca(solid), which has an intrinsic sticking probability of unity, as also observed previously. ^[120,121]

5.2.4 Comparison to Ca Adsorption on Other Polymers

The qualitative trend of the heat of adsorption versus Ca coverage seen here for Ca on P3HT Figure 5.3 is very similar to that previously reported for Ca on poly(methyl methacrylate) (PMMA) ^[120] and Ca on polyimide (PI) ^[214], and would probably be even closer if the Ca/PI data had used true measured sticking probabilities instead of assuming unit sticking probability. This suggests that the same basic reaction events are at work in each case. The Ca/P3HT reaction is shown to initially involve a sulfur-specific abstraction mechanism (which requires subsurface diffusion). However, the

coverage dependence of the heat requires a kinetic competition between this highly exothermic subsurface reaction and the much less exothermic clustering of Ca on top of the polymer surface to form solid Ca particles and eventually a continuous Ca film. The subsurface reaction dominates initially but, as the diffusion depth required for this reaction increases, it becomes less likely and, as the area covered by Ca clusters increases, Ca addition to these becomes more likely. It must be this same kinetic competition between some highly exothermic reaction below the surface and the clustering of Ca on top of the polymer which is the common feature in the reaction of Ca with these three very different polymers. In the case of PMMA, the highly exothermic subsurface reaction occurs with ester groups and is also thought to require cleavage of C-heteroatom bonds.^[120] In the case of polyimide, the highly exothermic reaction probably involves Ca inducing some subsurface C–O or C–N bond cleavage.

The qualitative trend of the Ca sticking probability versus Ca coverage seen here for Ca on P3HT (Figure 5.1) is also very similar to that previously reported for Ca on PMMA.^[120] This is also due to the similarity of this kinetic competition. Initially, the sticking probability is low since the polymer surfaces are inert and the physisorbed Ca atoms must diffuse subsurface to find the dominant reaction sites, during which time the Ca adatom may also desorb. In addition, the initially predominating reaction of Ca with P3HT involves cleavage of C–S bonds and thus probably has an activation barrier, which reduces the sticking probability, as mentioned above. Once the Ca reacts with the first layer of subsurface thiophenes or esters, this changes the electronic structure of the polymer, which seems to increase its intrinsic sticking probability for Ca. During these stages, the sticking probability is controlled by a kinetic competition between the relative rates of subsurface diffusion and desorption of the very weakly adsorbed Ca atoms. If the Ca-induced change in electronic structure upon reaction of the first layer of subsurface thiophenes or esters is sufficient to increase the former rate or decrease the latter rate, then the sticking probability will increase, as observed. A further increase in sticking probability occurs as Ca particles nucleate and begin to cover a larger and larger fraction of the surface, since Ca sticks with unit probability to Ca surfaces. Unit sticking probability is reached by ~ 4 ML, well before LEIS shows that the surface is completely covered by Ca (~ 11 ML). This indicates that Ca traps with nearly unit probability into a weakly-bound precursor state on the Ca-free parts of the polymer surface, and rapidly diffuses across the surface to find growing Ca clusters.

Such behavior is common in metal nucleation and particle growth on surfaces which attract metal atoms only weakly, such as many oxides.^[215] This also explains why the heat of Ca adsorption reaches the bulk heat of sublimation already at 4 ML.

5.3 Conclusions

Calcium adsorbs on poly(3-hexylthiophene) with a high heat of adsorption of 405 kJ/mol between 0.1 ML and 0.6 ML, which correlates in coverage with the appearance and growth of a new S 2p XPS signal that is shifted by -2.8 eV relative to the respective signal of the unreacted polymer. These findings are attributed to Ca inducing the cleavage of C–S bonds in the thiophene groups below the surface, and formation of CaS clusters. LEIS and XPS measurements reveal that Ca ultimately reacts with sulfur atoms down to a depth of ~ 3 nm, which corresponds to $1.2 \cdot 10^{15}$ atoms of reacted sulfur atoms per cm^2 , or nearly 5 monomer-unit layers. At high coverage, the adsorbed Ca also forms 3D Ca clusters on the surface of the polymer. This process, which competes with diffusion to the subsurface region and reaction with sulfur, predominates above ~ 2 ML and leads to the formation of a continuous Ca(solid) multilayer film beyond 11 ML. These competing kinetics can be explained by invoking a transiently adsorbed, mobile Ca species, bound by the very weak attractive interaction of Ca to the dominant polymer moieties (CH_2 , CH and CH_3). This adsorbed Ca precursor state can either (a) diffuse to the sulfur atoms of subsurface thiophene units and react, (b) diffuse to find other Ca atoms on the surface and to form Ca clusters, or (c) desorb.

6 Calcium Adsorption on Electron-Irradiated P3HT

The adsorption of Ca on electron-irradiated P3HT surfaces at 300 K ($E_{\text{kin}}=100$ eV) has been studied by adsorption microcalorimetry, atomic beam/surface scattering, X-ray photoelectron spectroscopy (XPS), and low-energy He⁺ ion scattering spectroscopy (LEIS). The results are compared to the studies of Ca adsorption on pristine P3HT presented in Chapter 5 and the corresponding publication.^[115] The major structural effect of electron irradiation is a substantial increase in the fraction of unsaturated carbon atoms, probably a result of electron-induced hydrogen abstraction from the hexyl chains and formation of new C=C double bonds, whereas no loss of sulfur was observed. The combined XPS, LEIS and calorimetry data indicate that the reaction and growth behavior of Ca on P3HT surfaces is not significantly affected by this electron damage, apart from an increased sticking probability at low coverages. The sticking probability of Ca on the irradiated P3HT is initially 0.63, compared to 0.36 on the pristine surface. It increases with coverage, up to unity by 4 ML Ca. The heat of adsorption stays nearly constant at 405 kJ/mol up to a coverage of 0.6 ML, which is ascribed to Ca diffusing below the surface and forming CaS clusters by abstraction of sulfur from the thiophene rings, based on XPS and LEIS data. The heat of adsorption then decreases gradually until it reaches the heat of sublimation of bulk Ca, 178 kJ/mol, by 4 ML. This is attributed to the formation of 3D Ca islands on top of the polymer, which eventually coalesce into a continuous Ca film by 11 ML. The heat of reaction versus coverage and the ultimate depth to which the Ca atoms react with the polymer thiophene groups (~ 3 nm) are nearly independent of electron damage, except for a difference in the heat of adsorption below 0.1 ML associated with defects or impurities. The increase in initial sticking probability caused by electron damage is explained by a stronger bonding of Ca adatoms to unsaturated versus saturated hydrocarbons. These very weakly held Ca adatoms are transient precursors to the two reactions which dominate the measured heat of adsorption (reaction with thiophene units and Ca cluster formation), but they can also desorb in this 3-path kinetic competition. Mass spec-

trometer data show that these precursors have longer surface residence times on the electron-damaged surface.

6.1 Results

6.1.1 X-ray Photoelectron Spectroscopy

To analyze the influence of the electron bombardment on the chemical composition of the polymer surface, XPS investigations before and after irradiation of the P3HT sample with 10 MLE electrons (corresponding to $7.4 \cdot 10^{15}$ electrons per cm^2) with a kinetic energy of 100 eV were performed. The survey XP spectra in Figure 6.1a show no major differences caused by the electron irradiation. However, they assure cleanliness of the sample, since only sulfur and carbon contribute to the spectrum. The inset furthermore proves that there is no S 2p intensity in the binding energy region 160-164 eV, which is important with respect to the Ca deposition studies described below.

Previous XPS investigations on pristine P3HT showed that deposition of Ca onto the polymer leads to the following changes: (a) damping of the S 2p and C 1s signals, (b) gradual shift of all S 2p and C 1s features towards higher binding energy due to band bending-like effects and (c) evolution of a new S 2p component, which is shifted by -2.8 eV relative to the S 2p signal of P3HT prior to Ca deposition.^[115] The last and most significant change (c) is attributed to a reaction of Ca with the S atoms from the thiophene rings of the polymer, resulting in the formation of CaS clusters. This interpretation has been confirmed by density functional theory (DFT) and MP2 calculations of core level shifts and reaction enthalpies. The depth up to which Ca atoms react with the polymer was calculated from the intensity ratio of the original and the new feature in the S 2p region. Here, similar investigations are reported for electron irradiated P3HT, in order to clarify the influence of the irradiation on the reaction depth of Ca.

The deposition of Ca on the irradiated P3HT sample was investigated by collecting spectra of the S 2p region before and after incremental deposition of Ca. Figure 6.1b displays spectra collected in direct succession: (i) before electron irradiation, (ii) after electron irradiation, and (iii) after deposition of 1.0 ML Ca on the irradiated surface. This Ca coverage allows for a straightforward comparison with a previous XPS investigation of Ca on pristine P3HT.^[115]

It is noteworthy that there is no effect of electron irradiation visible in the S 2p

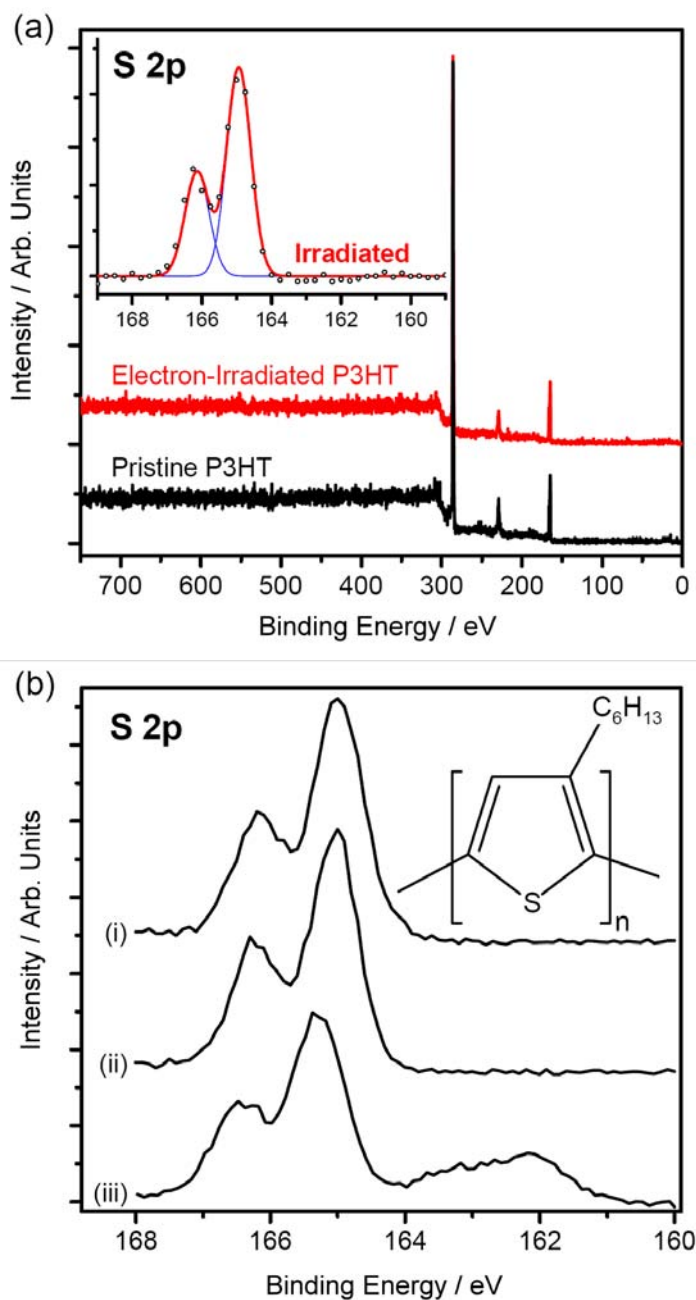


Figure 6.1: (a) Survey XP spectra recorded before (bottom) and after electron-irradiation (top). The inset shows the S 2p region after irradiation in more detail. Note that there is no S 2p intensity in the range between 160 eV and 164 eV before or after irradiation, consistent with our earlier results.^[18] (b) XP spectra of the S 2p region acquired before (i) and after (ii) electron irradiation and after deposition of 1.0 ML Ca on the electron irradiated P3HT sample (iii), recorded consecutively on one sample. The inset shows the molecular structure of P3HT.

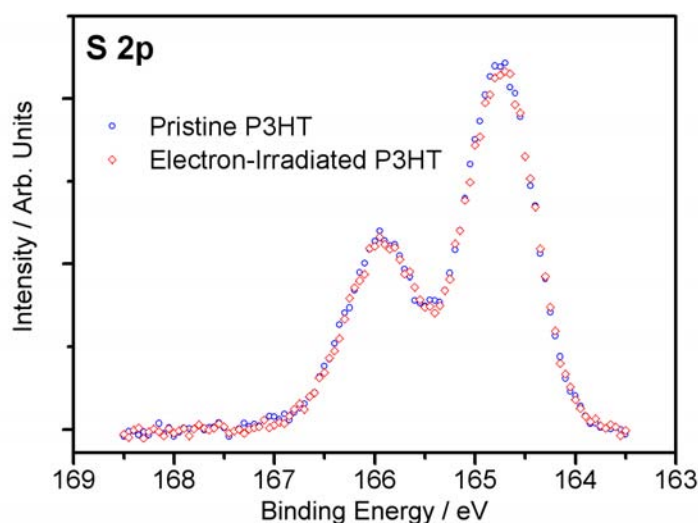


Figure 6.2: XP Spectra of the sulfur region before and after electron irradiation. The spectra were normalized with respect to the background signal, only (no other post processing was performed).

region of the spectra, as spectra (i) and (ii) are virtually identical. This indicates that the thiophene ring is not affected by the electron bombardment; in particular, no loss of sulfur as reported in earlier studies^[216,217] is observed. In addition, the lack of any shift in binding energy confirms that the electron-beam induced changes in the C 1s region discussed below are not related to charging or band bending effects, which would also shift the sulfur feature.

In Figure 6.2, the two spectra are displayed right on top of each other, after normalization to the background signal in the individual spectra. It is obvious that the spectra are not distinguishable without labeling, which emphasizes strongly that no sulfur is lost due to electron irradiation and that no shift in binding energy occurs, as was concluded above from Figure 6.1.

Spectrum (iii) in Figure 6.1 recorded after deposition of 1 ML Ca exhibits the expected damping of the S 2p feature by the Ca overlayer and a shift of 0.31 eV towards higher binding energy. The latter effect is attributed to band bending effects. Most importantly, a new feature shifted by -2.8 eV relative to the original signal evolves. All these changes agree with our previous results for Ca on pristine P3HT.^[115] In particular, the intensity ratio of the original S 2p feature to the newly evolved one (0.3) and the observed binding energy shift are in perfect agreement with the respective values on the pristine surface for a Ca coverage of 1 ML.^[115] With the depth profiling method based on the relative S 2p intensities of reacted and

unreacted polymer introduced in Section 2.2.2, the thickness of the reacted layer is calculated to be 1.2 nm at this Ca dose. This conforms with the value for pristine P3HT obtained from the same type of analysis.^[115]

Figure 6.3 displays XP spectra of the C 1s region of (a) pristine and (b) electron-irradiated P3HT. According to a previous study by Ratcliff et al. and in agreement with the composition of the polymer (see inset of Figure 6.1b), the spectrum of pristine P3HT can be deconvolved into two components with a 3:2 intensity ratio, one for saturated aliphatic carbon atoms (6 atoms per repeat unit) and another for unsaturated (aromatic) carbon atoms (4 atoms per repeat unit).^[218] Using these two components with their reported binding energy difference of 0.4 eV^[218], the C 1s spectrum in Figure 6.3a is deconvolved with two peaks of equal full widths at half maximum of 0.8 eV, one at 285.8 eV for saturated and another at 286.2 eV for unsaturated carbon. The fitting procedure leads to an intensity ratio of 3:2, reflecting the polymer structure correctly. Irradiation with electrons with a kinetic energy of 100 eV results in small but significant changes in the C 1s XP signal, most notably a shift towards higher binding energy. Since no shifts occur for any of the other core level signals of the sample, charging and band bending effects can be excluded as possible origins of the C 1s shift. For the deconvolution of the C 1s spectrum of the irradiated sample (Figure 6.3b), it is assumed that there is still saturated and unsaturated carbon, but with a different ratio. Therefore, the same two components for saturated (285.8 eV) and unsaturated (including aromatic) carbon (286.2 eV) that were used in the peak fitting for the pristine sample are used, again. For the irradiated sample, however, the relative intensities amount to 34 % (saturated carbon) and 66 % (unsaturated carbon), respectively; in other words, the saturated:unsaturated ratio has changed from 3:2 before electron irradiation to 1:2 afterwards. The fraction of unsaturated carbon atoms obviously increased due to the influence of the electron beam, presumably by electron-induced hydrogen elimination followed by intramolecular rearrangement yielding C=C double bonds. This interpretation is supported by a previous study of the irradiation of poly-styrene with 100 eV electrons, where it was found that H⁺ is the predominantly desorbing ion.^[191]

A deconvolution of the C 1s signal using two components – one ascribed to C atoms attached to the S atom in the thiophene ring and the other one to all remaining C atoms – with an intensity ratio of 1:4 (as was used previously in reference [160]) did not yield adequate fitting results. Thus, this model was discarded. The C 1s spectra

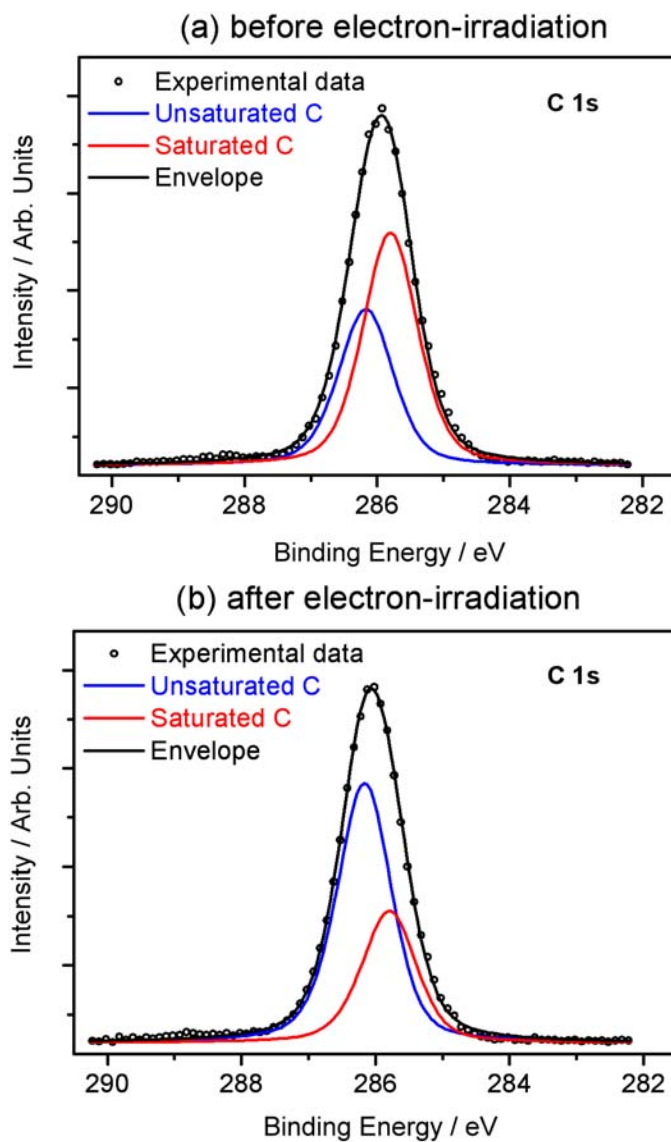


Figure 6.3: XP spectra of the C 1s region (a) before and (b) after electron-irradiation (electron dosage 10 MLE). The black open circles represent the experimental data, while the two individual components used to fit the experimental data are displayed using blue (unsaturated / aromatic carbon) and red (saturated carbon) lines. The sum of the individual components is indicated by the black line. The intensity ratio saturated (aliphatic):unsaturated (aromatic) carbon is 3:2 in (a) and 1:2 in (b), respectively.

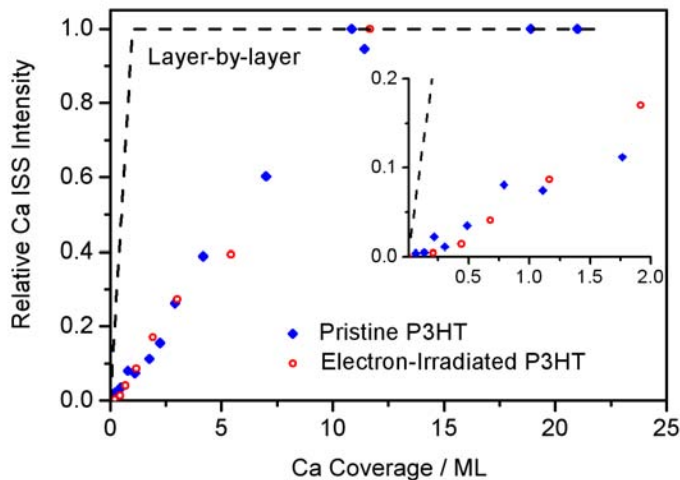


Figure 6.4: LEIS measurements of Ca on electron-irradiated and pristine P3HT. The relative integrated Ca LEIS peak intensity is displayed as a function of Ca coverage at 300 K. All intensities were normalized with respect to the saturation signal obtained for high Ca coverages (red hollow circles: irradiated sample; blue diamonds: pristine sample). The black dashed line indicates the expected trace for layer-by-layer growth. The inset shows the low-coverage region in more detail.

recorded during Ca dosing on electron irradiated P3HT (not shown here) show the same shift to higher binding energies as was previously observed after Ca adsorption on pristine P3HT.^[115] This shift is attributed to band bending effects. Here, these shifts add to the shift of the C 1s signal caused by the electron irradiation prior to deposition of Ca.

6.1.2 Low-energy ion scattering (LEIS)

Because of its top-layer surface sensitivity, LEIS is a valuable tool for investigating the varying growth modes of metals on polymer films.^[219] In Figure 6.4, the normalized Ca LEIS intensity is plotted as a function of the Ca coverage, again for both, pristine and electron-irradiated P3HT; the inset shows the low coverage range in more detail. The curves show no statistically significant difference, indicating that the growth mode is not affected by electron irradiation prior to Ca deposition. In both cases, the Ca intensity increases nearly linearly, but saturation is not reached until ~ 11 ML. This is a much higher coverage than expected for layer-by-layer growth, where saturation would occur at 1.0 ML.

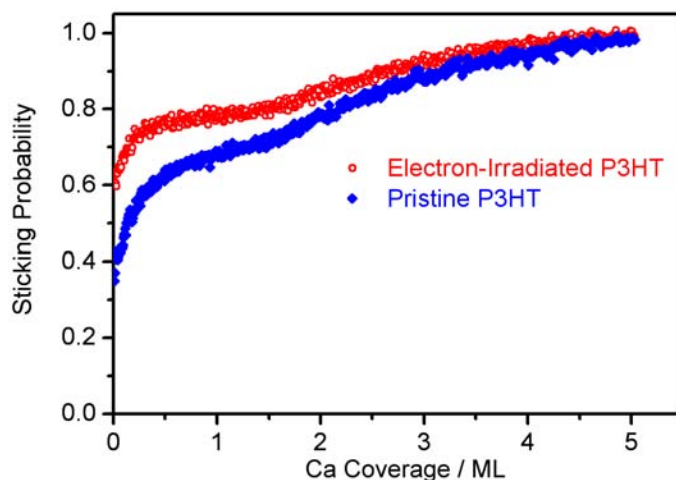


Figure 6.5: Sticking probability of Ca on a P3HT film at 300 K plotted as a function of Ca coverage for the pristine (blue diamonds) and electron-irradiated (red hollow circles) P3HT surface. The coverage was calculated from the Ca dosage and the sticking probability.

In order to exclude any detectable degradation of the polymer induced by exposure to the He^+ -ion beam, similar LEIS measurements were performed using much shorter acquisition times and accordingly reduced ion doses. These experiments show essentially the same result, namely that substantial degradation induced by the ion bombardment can be excluded.

6.1.3 Sticking Probability

Figure 6.5 displays the sticking probability of Ca on electron-irradiated P3HT at 300 K as a function of Ca coverage and, for comparison, the respective data for pristine P3HT. At low Ca coverage, the sticking probability in both cases deviates from unity quite significantly, but approaches unity between 4 ML and 5 ML. Since clean, multilayer Ca surfaces have unity sticking probability for Ca^[120], this implies that the surface remains incompletely covered by Ca at least up to ~ 5 ML, consistent with the LEIS data shown above. The shape of the sticking probability curve for irradiated P3HT is qualitatively very similar to the shape of the curve for the pristine polymer: the sticking probability steeply increases from its initial value of 0.6 to 0.75 at 0.33 ML. Then, the curve flattens and slowly reaches 0.8 at 1.5 ML. Above this coverage, the slope increases again and the curve reaches unity around 5 ML. The major difference between the two curves is an upwards-shift of the trace for electron-irradiated P3HT. The higher initial sticking probability of Ca on

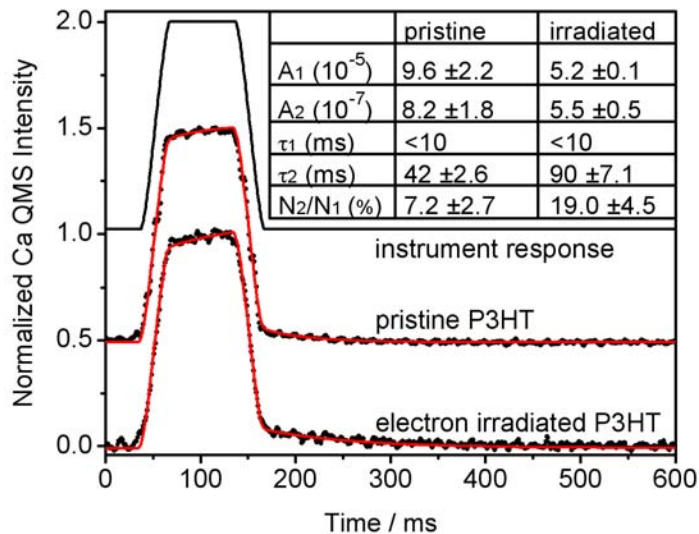


Figure 6.6: The observed Ca QMS signal (at $m/e = 40$) as a function of time for 100 ms pulses of Ca impinging on a P3HT surface at a repetition rate of 0.5 Hz with and without electron irradiation. The data points are the average of three experiments, for which the first 100 pulses of Ca onto P3HT (Ca coverage range 0 to ~ 0.7 ML) were averaged for each experiment; in this coverage range the sticking probability of Ca on both pristine and irradiated surfaces is non-unity. The red lines are fits to the data generated by convolving two exponential decays with the instrument response function. The inset gives the average best-fit parameters for the two exponential decays, with the estimated error bars based on the range of values for the best fits to multiple data sets (but always using $\tau_1 = 5$ ms, which is its average value within its acceptable range $0 < \tau_1 < 10$ ms).

the electron-irradiated P3HT is not unexpected, as this electron-damage effect has been observed before, for example for Ca adsorption on poly(methyl-methacrylate) (PMMA) ^[120], and will be discussed below. The sticking probability data reported here, in conjunction with the flux of Ca atoms, will be used in Section 6.1.4 for determining the molar heat of adsorption of Ca.

The pulsed molecular beam used here to measure the sticking probability by mass spectrometry also allows the determination of surface lifetimes for the impinging atoms that do not permanently adsorb to the surface. ^[114,220] The measured QMS signal plotted in Figure 6.6 is a convolution of the instrument response function with the system response function, which is an expression for the physical processes that lead to a time lag for Ca atoms desorbing from the surface. Assuming a simple trapping/desorption mechanism with first-order desorption kinetics for the

atoms that do not “stick” permanently, the system response function is a simple exponential decay with characteristic time constant τ , corresponding to the lifetime in the precursor state. Then, the system response function $y(t)$ is of the form:

$$y(t) = A \cdot \exp\left(-\frac{t}{\tau}\right) \quad (6.1)$$

where A is a fitting parameter. An attempt to fit the pulse shapes in Figure 6.6 with this simple model resulted in inadequate results. The data were, however, well fitted using a system response function incorporating two trapping/desorption pathways. The corresponding system response function is the sum of two exponential expressions:

$$y(t) = A_1 \cdot \exp\left(-\frac{t}{\tau_1}\right) + A_2 \cdot \exp\left(-\frac{t}{\tau_2}\right) \quad (6.2)$$

Fits employing this kind of system response function are shown in Figure 6.6 along with the best fit parameters. A similar behavior has been observed previously in a study of the adsorption of Pb on Mo(100).^[220] There, desorption from terrace sites and step sites constituted the two different desorption pathways. As the quality of the fitting results were not influenced by variation of τ_1 between 0 and 10 ms, this step is concluded to be faster than the instrument response time, which is on the order of 10 ms.

The ratio $\frac{A_2 \cdot \tau_2}{A_1 \cdot \tau_1}$, listed as N_2/N_1 in the fit parameters, is equal to the ratio of the number of Ca atoms desorbing from the two pathways within the two-second pulse period. This ratio is well below one for both the pristine and electron irradiated P3HT, indicating that the dominating contribution to the signal stems from the faster pathway. The main effect observed after electron irradiation is an increase the contribution of the slower (τ_2) pathway and a significant increase in the time constant for the slower pathway from 42 ms to 90 ms.

It may seem surprising that the small changes between the two lower traces in Figure 6.6 can be responsible for the large change of the sticking probability. However, it should be considered that the signal shape is dominated by the non-sticking fraction, which corresponds to atoms which are simply reflected or desorbing from a very short lived precursor state (<10 ms). In contrast, the precursor states with the longer lifetimes (42 ms and 90 ms) contribute only marginally to the desorption signal because of their much higher probability for permanent adsorption.

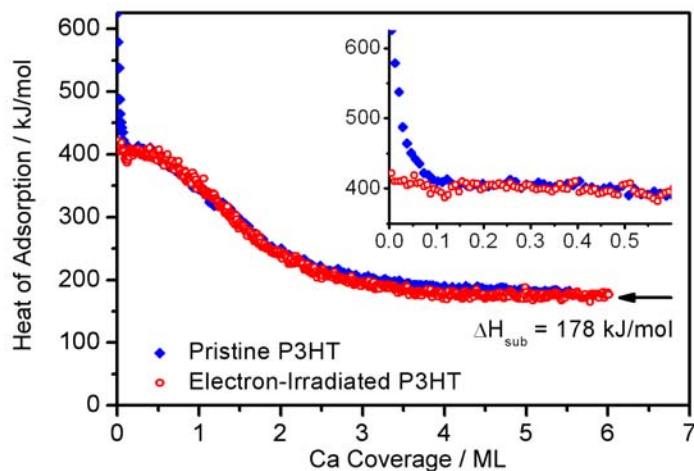


Figure 6.7: The differential heat of adsorption of Ca atoms on an rr-P3HT surface (red hollow circles: electron-irradiated sample, blue diamonds: pristine sample) as a function of Ca coverage at 300 K. The inset shows an enlarged plot of the low-coverage range, where the curves are different. On the right hand side, the sublimation enthalpy of Ca, $\Delta H_{\text{sub}}=178$ kJ/mol, is indicated.

6.1.4 Heats of Adsorption

Figure 6.7 presents the differential heats of adsorption, that is, the standard enthalpies at 300 K, of Ca on both pristine and electron-irradiated P3HT, as a function of coverage. The data shown are averaged over three highly reproducible experimental runs. In the inset, the low-coverage region (0 to 0.6 ML) is shown in more detail. There is only a small difference due to electron damage, as discussed below.

For the irradiated sample, the heat of adsorption stays nearly constant at around 405 kJ/mol for coverages up to 0.6 ML. This high heat is attributed to Ca abstracting subsurface thiophene S atoms to form CaS clusters and C–C bonds between adjacent polymer chains, as shown to occur on the pristine surface (see Chapter 5).^[115] Above 0.6 ML coverage, the heat of adsorption decreases, gradually approaching the sublimation enthalpy of Ca ($\Delta H_{\text{sub}}=178$ kJ/mol) to within 2 kJ/mol by a coverage of 4 ML, where Ca is mainly adding to 3D Ca particles to eventually make a continuous Ca film on the surface. It is clear from the similarity of the heat of adsorption curves that these same processes also occur on the electron-damaged surface. The heats of adsorption on the irradiated P3HT differ only in the very low coverage regime (<0.1 ML) from those observed on pristine P3HT. The very high initial heat of adsorption (625 kJ/mol) for the pristine P3HT surface has been ascribed to the reaction of Ca with ~ 0.02 ML of defect or impurity sites.^[115] The

absence of this very high initial heat of adsorption for the electron-irradiated P3HT may be due to the electron-induced removal or altering of these defect or impurity sites such that they can no longer react with impinging Ca atoms.

6.2 Discussion

It was shown that irradiating P3HT surfaces with electrons of 100 eV kinetic energy leads to distinct changes in some of the polymer's properties and the adsorption behavior of Ca thereon, while other properties are less affected. In the following, these electron-induced chemical changes and the resulting effects on the interaction of Ca with the polymer will be discussed. Based on the previous study of Ca on pristine P3HT^[115], a detailed mechanistic model of adsorption, reaction and growth of Ca on the irradiated polymer surface will be presented.

The interaction of Ca atoms with pristine P3HT surfaces was extensively discussed in Chapter 5 and reference [115]. Only the most important points related to our new results on electron irradiated P3HT shall be recalled here to allow for a better comparison. XPS investigations showed the evolution of a new feature in the S 2p region upon deposition of Ca on pristine P3HT. With the aid of DFT and MP2 calculations, this new feature could be attributed to calcium sulfide clusters formed by the reaction of Ca with the thiophene groups of the polymer. Furthermore, XPS depth profiling with respect to the concentrations of reacted and unreacted thiophene groups revealed that the Ca atoms diffuse sub-surface and react with the polymer up to a depth of ~ 3 nm. In competition with this reaction, Ca atoms also form 3D clusters and solid particles on the surface. LEIS, adsorption calorimetry and sticking probability data show that this process becomes increasingly efficient at higher coverages and prevails above 4 ML. The Ca particles coalesce into a continuous Ca film by around 11 ML.

First, the chemical changes of the polymer surface induced by electron-irradiation are addressed. The S 2p XP spectra taken before and after electron irradiation (Figures 6.1b and 6.2) show no substantial differences. This indicates that the thiophene ring is not affected by the electron beam and in particular that no sulfur is removed from the surface region. Note that previous work reports that irradiation with electrons of 500 eV kinetic energy leads to partial desulfurization.^[217] Instead, the electron beam damages the aliphatic parts of the P3HT. Especially, the C 1s XP spectra show that electron irradiation increases the fraction of unsaturated carbon atoms,

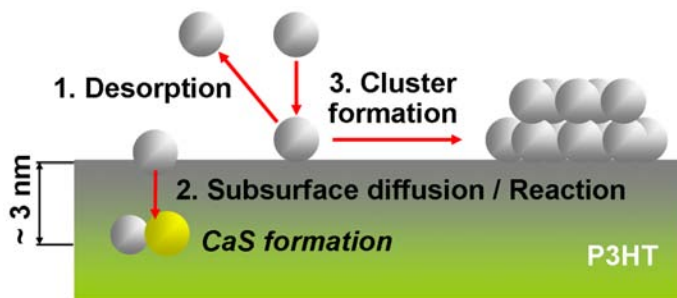


Figure 6.8: Schematic of the kinetic competition between different reaction pathways for impinging Ca atoms discussed in the text.

presumably by hydrogen abstraction and formation of new C=C double bonds in the hexyl side chains of the polymer.

The calorimetric measurements show that the heat of adsorption and reaction of Ca is almost identical with and without electron irradiation, in particular in the range 0.1 to 1.6 ML, where the reaction between Ca and the thiophene groups is the dominant contribution to the heat of adsorption. Further evidence that the thiophene groups are unaffected by the electron irradiation is provided by the S 2p XP spectra recorded after incremental doses of Ca on the irradiated P3HT. These spectra show exactly the same behavior as the corresponding spectra on the pristine sample^[115], particularly with respect to the signal intensities of reacted and unreacted sulfur as a function of Ca coverage. This suggests that the sulfur in the surface region is not lost due to the electron irradiation and that the reaction depth of ~ 1.2 nm at 1 ML Ca coverage, as derived from the XPS experiments, remains unchanged with respect to interpolated values for Ca adsorption on pristine P3HT.

It was demonstrated in previous work (see Chapter 5 and reference [115]) that the thickness of the reacted layer can also be derived from the heat of adsorption data. Applying this method to Ca deposition on irradiated P3HT yields a value of ~ 3 nm for the saturation thickness of the reacted layer on electron-irradiated P3HT. The same value as was previously found for pristine P3HT.^[115] This result is not surprising, because the heat curves before and after irradiation are identical except for the very low coverage regime (< 0.1 ML).

Second, the sticking probability of Ca atoms on the polymer surface is elaborated. To understand why this probability is substantially increased by electron irradiation, as was shown in Section 6.1.3, one needs to recall the model developed for the understanding of Ca adsorption on pristine P3HT. According to this model, the

shape of the sticking probability vs. coverage curve reflects a kinetic competition between three reaction pathways of a Ca atom in a transiently adsorbed precursor state, which is also presented graphically in Figure 6.8: (1) desorption, (2) subsurface diffusion and subsequent reaction with the thiophene groups under formation of CaS, and (3) formation and growth of Ca clusters and eventually a continuous Ca film on the surface of the polymer. For the first 1 ML, processes (1) and (2) prevail, leading to subsurface reaction exhibiting a high heat of adsorption, but a low sticking probability (0.4 to 0.6). The low sticking probability is associated with the fact that the reaction of the weakly-held Ca with the thiophene groups involves bond cleavage and thus has an activation barrier comparable to its desorption barrier. The rapid increase of the sticking probability in the coverage range 0 to 0.33 ML is ascribed to changes in the electronic structure induced by reaction of Ca with the polymer. The coverage at which the curve starts to flatten, approximately 0.33 ML, corresponds to the amount of Ca required to completely react with the sulfur atoms in the first layer of thiophene units and to form one complete layer of “reacted” repeat units of the polymer. These will have a different electronic structure than pristine P3HT and thus a different bonding energy for weakly-held Ca atoms, which apparently gives rise to a higher sticking probability. Above this coverage (and up to ~ 1.4 ML, where process (3) comes into play), the curve therefore corresponds to the intrinsic sticking probability of Ca on P3HT in which the topmost thiophene units have already reacted with Ca. In this coverage range (0.33 ML to 1.4 ML), there is less change in the sticking probability, since additional Ca predominantly reacts with thiophene groups deeper in the polymer. Between 1.5 ML and 2.5 ML, the sticking probability increases more rapidly, because adsorbing Ca atoms can now undergo process (3) and add to Ca clusters on the surface. Since Ca atoms have a sticking coefficient of unity on solid Ca and since the number and/or the size of the clusters grow, this process competes increasingly successfully with the diffusion of the metal into the polymer, until the surface is eventually covered with a continuous Ca film. The same mechanism and kinetic competition can be used to explain the very similar shape of the sticking probability versus coverage curve for the electron-irradiated P3HT. Note that Ca atoms bind strongly to the Ca clusters or the Ca film (178 kJ/mol) and therefore are unlikely to detach and react further with deeper layers of the polymer at room temperature. This is the most likely reason why the ultimate thickness of the reacted layer is intrinsically limited.

The markedly higher sticking probability of Ca on the irradiated sample was ex-

plained in Section 6.1.3 with the prolonged lifetime of the transiently adsorbed Ca precursor state, which was observed directly by atomic beam/surface scattering. The longer lifetime of the precursor increases its chance of finding an appropriate adsorption or reaction site for the Ca atoms before desorbing, and thus causes a higher sticking probability. Based on the observation that electron irradiation leads to the formation of C=C double bonds at the expense of C–C single bonds, we propose that the increased interaction of weakly-held Ca with the additional π -bonds is responsible for the higher sticking probability on the irradiated polymer.

The shape of the heat of adsorption curve in the region above 0.1 ML is determined by the same kinetic competition as the shape of the sticking probability curve. At low coverages, the strongly exothermic reaction (405 kJ/mol) of Ca with thiophene under formation of CaS prevails, as was shown previously^[18], whereas the less exothermic formation of bulk Ca (178 kJ/mol) becomes the predominating process at higher coverages. The fact that the curves before and after electron irradiation have almost the same shape above 0.1 ML indicates that the two processes have the same relative probabilities at any given coverage, regardless of whether the surface was bombarded with electrons prior to Ca adsorption or not.

The two heat vs. coverage curves are markedly different only in the range below 0.1 ML. For pristine P3HT, the heat of adsorption changes rapidly from 625 kJ/mol to 405 kJ/mol within the first 0.1 ML. This feature has been attributed to a very small concentration of defect or impurity sites on the P3HT surface (or in the near-subsurface) that bind or react with Ca very strongly. These sites may originate from impurities such as residual chloroform, dioxygen or water, or from intrinsic surface defects such as the ends of polymer chains. Based on the calorimetry data, the number of such sites is very low: <0.1 ML distributed over a depth range of ~ 3 nm or more, if the impurities are mobile and can diffuse to the surface within the timeframe of the experiment. This is consistent with the fact that they were not detected by XPS within reasonable data acquisition times. After these few sites are saturated (i.e., at Ca coverages above 0.1 ML), Ca adsorbing on P3HT releases a heat of adsorption of about 405 kJ/mol, which originates from the reaction of the Ca atoms with the thiophene groups. If Ca is adsorbed after electron irradiation, the heat vs. coverage curve starts directly at 405 kJ/mol and the heat remains almost constant within the first 0.5 ML. This qualitative difference was independent of the order in which the measurements were made, i.e., pristine samples were measured both before and after electron-damaged samples, providing strong evidence that this

difference is not due to variations in the way the samples were prepared or outgassed. Apparently, the impurities and/or defect sites are removed or deactivated by electron bombardment, which is the opposite of what may naïvely be expected. For example, residual solvent from the spin coating process may be removed from the surface by electron stimulated desorption. Another possibility is that reactive molecules such as residual dioxygen may be dissociated by the electron bombardment and react with the polymer, such that a reaction with Ca is not possible or less exothermic. Since the nature of the sites with the very high adsorption energy is unknown, the explanation must remain speculative at this point.

6.3 Conclusions

The adsorption and reaction of Ca on poly(3-hexylthiophene) (P3HT) was studied after irradiation of the polymer with electrons with a kinetic energy of 100 eV. The results are compared with the investigation of Ca on pristine P3HT, which allows for the presentation of a conclusive picture of the changes induced by the electron irradiation.

XPS shows that electron irradiation increases the ratio of unsaturated to saturated carbon from initially 2:3, which agrees with the chemical composition of the pristine polymer, to 1:2 after irradiation. This change is attributed to hydrogen abstraction from the hexyl side chains of the polymer and formation of new C=C double bonds. In contrast, the aromatic thiophene groups are apparently not affected by the electron bombardment; in particular, no loss of sulfur is observed.

These chemical changes influence the adsorption of Ca atoms and lead in particular to higher sticking probabilities below 5 ML due to longer residence times of Ca atoms in the precursor state. This effect is ascribed to a stronger interaction of the trapped Ca atoms with the unsaturated carbon atoms.

The coverage dependence of the sticking probability and the heat of adsorption can be understood on the basis of a kinetic competition between three reaction channels for the trapped Ca atoms: (1) desorption, (2) subsurface diffusion and reaction with thiophene groups under formation of calcium sulfide and (3) formation of 3D Ca particles on the surface, which eventually coalesce into a continuous film of solid Ca. The LEIS, sticking probability and calorimetry data show that the relative rates for the three processes are nearly identical for the electron-irradiated and the pristine polymer and vary in the same way with Ca coverage. However, electron damage

increases the lifetime of the transiently adsorbed Ca precursor. As a result, the fraction of Ca atoms that undergo processes (b) and (c) increases measurably at low coverages resulting in a higher sticking probability.

In contrast, electron irradiation has no influence on the heats of adsorption at low coverages (405 kJ/mol in the range 0.1 ML to 0.5 ML, attributed to the reaction of Ca with thiophene) and at high coverages (178 kJ/mol above 5 ML, attributed to the formation of bulk Ca). In addition, the depth up to which Ca reacts with the polymer, ~ 3 nm, is not influenced by the electron bombardment. The only difference in the heats of Ca adsorption concerns the range of very low coverages (< 0.1 ML). On pristine P3HT, the heat of Ca adsorption changes from 625 kJ/mol to 410 kJ/mol within this coverage range, which was attributed to the initial reaction of Ca with impurities or defects sites in the pristine polymer. For the electron irradiated polymer, however, the heat is constant at 405 kJ/mol, even below 0.1 ML. This shows that the impurities and/or defect sites are removed or deactivated by electron bombardment via a mechanism that is yet unknown.

7 Calcium Adsorption on P3HT at Low Temperature

The importance of the metal-polymer interface has been emphasized in Chapter 4 and the basic processes governing the interface formation between P3HT and Ca are addressed in Chapters 5 and 6. This chapter now focuses on the influence of the substrate (P3HT) temperature during vacuum-based vapor deposition of Ca. The preceding chapters have shown that the resulting interface exhibits a high chemical and structural complexity: Ca atoms diffuse into the polymer, undergo chemical reactions with the polymer and form clusters atop the polymer surface. It is well established that the metal-polymer interface is decisive for the performance of working devices; charge injection rates at the metal/organic interface depend critically on the overlap of wave functions, i.e., the chemical bonds at the metal-polymer interface.^[5] It is quite obvious that especially the reaction between metal and polymer strongly influences the chemical composition and the electronic structure.

In Chapters 5 and 6, it was shown that Ca cleaves the thiophene units of the polymer, forming calcium sulfide (CaS). When Ca is deposited at 300 K and low fluxes of ~ 0.4 ML per minute, the reaction zone extends ~ 3 nm into the polymer, but does not grow any further irrespective of continued dosage of Ca. Excess Ca accumulates on the surface of the polymer in Ca clusters, which eventually coalesce into a closed film. Detailed investigation of energetics and dynamics of the interface formation revealed that subsurface diffusion and reaction of an adsorbing Ca atom proceeds at a lower rate than the attachment of the Ca atom to particles (clusters) of solid Ca on the surface (or in the near-surface region) of the polymer.^[115,158] Based on these findings, it is proposed that subsurface diffusion and reaction is only possible during the initial phase of metal adsorption. Once Ca clusters have been formed on the surface, additional adsorbing Ca adds to these clusters rather than diffusing into and reacting with the polymer.

If this scenario is correct, a sharp, well-defined metal/polymer interface will be obtained, if subsurface diffusion and reaction is suppressed during the initial stages of metal adsorption. Here, it is demonstrated that this can be achieved by performing

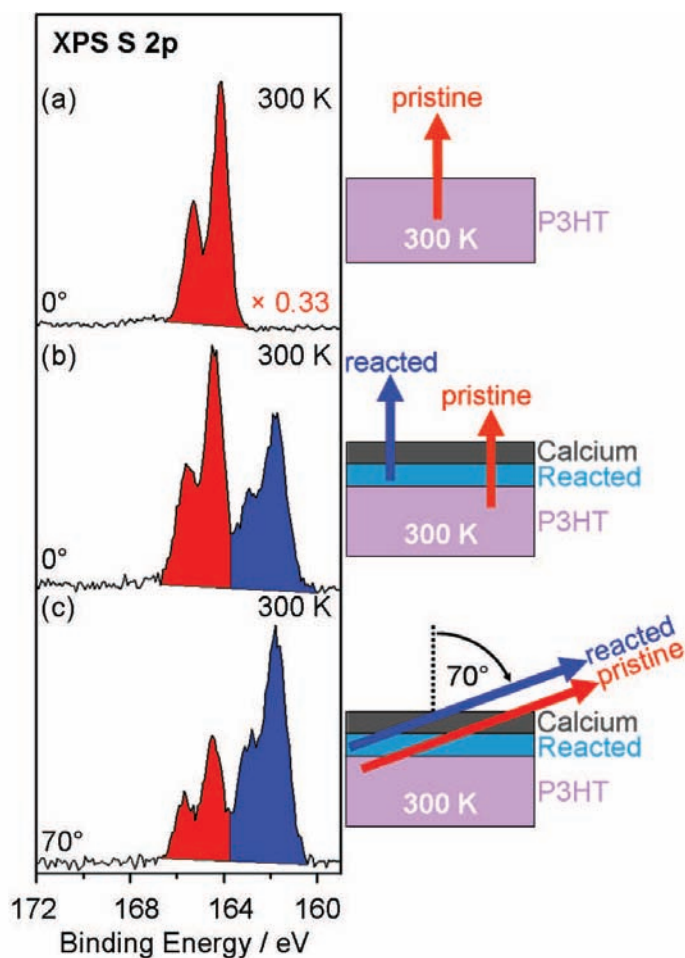


Figure 7.1: XP spectra collected of (a) pristine P3HT under normal emission (the intensity is scaled by a factor of 0.33) and 12 ML Ca dosed at 300 K on P3HT at an emission angle of (b) 0° and (c) 70° .

the metal deposition at low temperatures (~ 130 K). After warming up to room temperature, the interface remains sharper compared to the case when the metal was directly deposited at room temperature. In fact, this route has been suggested by Strunskus et al. in reference [170] and some results for deposition of a metal on a polymer at low temperature were presented by the same group in reference [157] – here low temperature refers to 230 K. However, an effect persisting after heating the sample to room temperature had not been reported yet.

7.1 Results and Discussion

For monitoring the reaction between Ca and the polymer, X-ray photoelectron spectra of the S 2p core level were collected. In these spectra, signals from reacted and unreacted P3HT can be distinguished. The S 2p XP spectrum of the clean polymer (in the form of a thin P3HT film spin-coated onto an Al foil) is shown in Figure 7.1a. It features a spin-orbit split signal at 164.1 eV (S 2p_{3/2}) and 165.3 eV (S 2p_{1/2}), which is attributed to sulfur in the unperturbed thiophene unit. Onto this pristine P3HT surface, Ca is vapor deposited at a rate of 0.4 ML/minute and at a substrate temperature of 300 K up to a total dose of 12 ML. Taking the coverage-dependent sticking coefficient into account (see Chapter 5), this dose leads to a coverage of 10.5 ML, which is sufficient for the formation of a closed Ca film on the surface of the polymer, as confirmed by low-energy ion scattering (LEIS) spectroscopy^[115].

Figure 7.1b shows the S 2p spectrum after Ca deposition on pristine P3HT at 300 K. The signal of pristine P3HT (S 2p_{3/2}) now appears at 164.4 eV, i.e., shifted by 0.3 eV relative to the S 2p_{3/2} signal before Ca deposition. This shift is due to band bending and occurs similarly in all spectra with Ca deposition; it is a purely electronic effect, which was observed in earlier studies as well (see Chapters 5 and 6).^[115,158] More importantly, the spectrum in Figure 7.1b features a new signal at 161.7 eV, i.e., -2.7 eV relative to the signal of pristine P3HT. As was discussed in Chapter 5, this signal results from small calcium sulfide (CaS) clusters which are formed by reaction between Ca and thiophene in the surface-near region.^[115,158] Spectrum 7.1c refers to the same sample as spectrum 7.1b, but the photoelectrons were here detected under an angle of 70° relative to the surface normal. As illustrated in Figure 7.1, this leads to an increased surface sensitivity, i.e., the information depth of the experiment is reduced from ~14 nm (detection along the surface normal) to ~5 nm. The information depth stated above refers to the information depth with respect to the polymer surface and not to the Ca covered surface, where an accurate determination of the information depth is impossible due to the complexity of the interface. The changes of the relative intensities of the two signal components in the spectra 7.1b and 7.1c with the detection angle thus allow us to estimate the depth of the reaction zone. Using the intensities for the reacted and unreacted sulfur and Equation (2.11), a value of 3.1±0.3 nm is obtained. This result is consistent with previous studies, which show a maximum thickness of the reaction zone of ~3 nm upon deposition at room temperature. In order to suppress the reaction between Ca

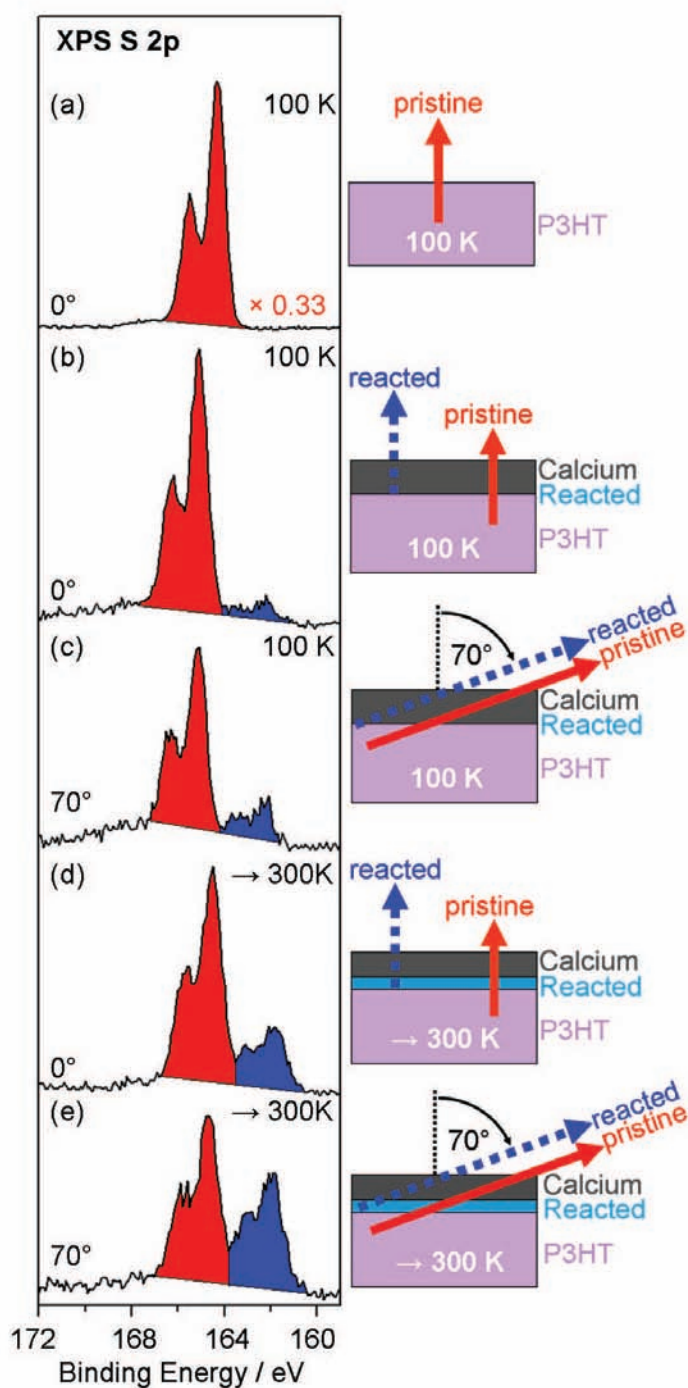


Figure 7.2: XP spectra of the S 2p region: (a) pristine P3HT (normal emission), 12 ML Ca dosed on P3HT at 130 K under 0° (b) and 70° (c) recorded at 130 K, and after warming the sample up to 300 K under 0° (d) and 70° (e).

and P3HT and to form a sharp metal-polymer interface, Ca is vapor-deposited on the polymer cooled to 130 K. The resulting S 2p spectrum is shown in Figure 7.2b. As can be seen, the signal of reacted sulfur (S 2p_{3/2}) at 162.3 eV is now very small and appears only slightly larger in the more surface sensitive 70° detection geometry. This indicates that the reaction zone is very thin, approximately 0.3 nm (note that due to the low intensities, the error bar on this value is quite substantial in size: ±0.2 nm) and that subsurface diffusion and reaction are efficiently suppressed at this temperature.

Now the question arises whether this effect persists after warming up the cold Ca/P3HT interface to 300 K. The answer is given by the S 2p spectrum in Figure 7.2d, which shows some intensity of the signal related to reacted sulfur, but still considerably less than after room temperature deposition. We conclude that deposition at 130 K permanently reduces subsurface diffusion of Ca and its reaction with the polymer. The 70° spectrum 7.2e confirms this conclusion, especially by direct comparison with spectrum Figure 7.1c for deposition at 300 K. The estimated depth of the reaction zone is now only 1.5±0.1 nm compared to ~3.1 nm for room-temperature deposition.

One may naively expect that the damping of the sulfur signal resulting from deposition of a substantial amount of Ca (12 MLE) leads to stronger signal damping than is observed in the spectra. The explanation for this unusual small damping is offered by the LEIS data (see Chapter 5 and Reference [115]), evidencing that the clusters coalesce only at high coverages of approximately 10 ML. This in turn means that after dosing 12 ML Ca, part of the surface are covered only by a very thin layer of Ca, while the thickness of the Ca film exceeds the nominal coverage in other parts. Accordingly, the areas with low local coverage show only very limited signal damping, while the parts of the polymer covered by a thicker Ca show a correspondingly larger attenuation. It can easily be shown that such a morphology leads to reduced damping compared to the case were the material forms a layer of uniform thickness. To illustrate this, an extreme case shall be considered, in which all material is contained in an infinitely tall island with zero lateral extension. The damping will be complete at the point of the island, but zero elsewhere. As the result, the overall damping will be zero at any coverage. In real cases of islands with finite height, the effect will of course be less pronounced, but show the same trend. Another point that may catch the attention of the reader is the small differences between spectra recorded under normal and 70° emission. This effect may too be

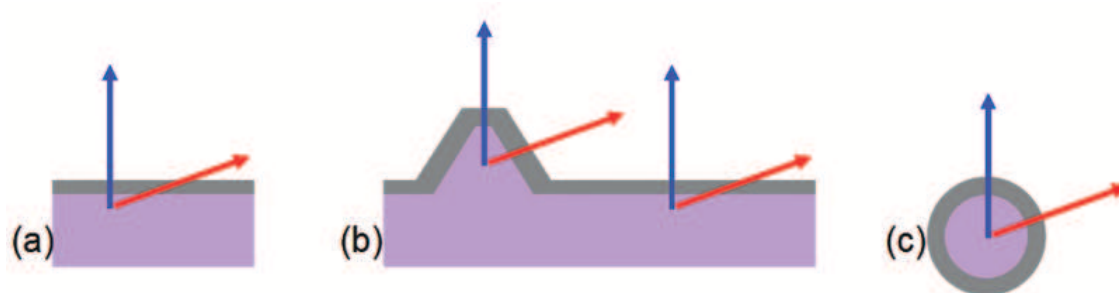


Figure 7.3: Schematic sketch to illustrate the influence of the morphology on the expected damping of the substrate signal for normal (blue arrows) and 70° emission (red arrows). Shown are the situation for a planar layered system (a), a roughened layered system (b) and a core-shell type particle (c).

rationalized considering the morphology of the sample: the influence of an overlayer on the underlying material's signal is usually considered for ideally flat surfaces. In that case, the way through the overlayer is significantly shorter (by a factor of ~ 3) for electrons emitted under normal emission compared to electrons emitted under 70° , such that a large signal dampening of the underlying substrate occurs in the corresponding spectra. This is shown schematically in Figure 7.3a. However, this is an ideal case and for other, more “rough” morphologies, the differences are not as pronounced. The other limiting case would be a spherical, core-shell type particle as depicted in Figure 7.3c. The determination of the thickness of the shell is not possible from the analysis of spectra recorded under different angles, because the apparent thickness of the shell remains unchanged for electrons emitted under different angles. A rough surface, finally, can be considered as an intermediate between both extremes discussed so far – it may or may not lead to a measurably different attenuation of the deeper layer, depending on the respective morphology. For the polymer surface, a certain roughness is to be expected; AFM micrographs of P3HT imply a root mean square (rms) roughness of 0.4 nm.^[115] Therefore, the lack of a pronounced difference in the signal strength between the spectra recorded under normal and 70° emission can be rationalized, especially in conjunction with the point addressed above concerning the overall small damping. Figure 7.4 displays LEIS data recorded for incremental doses of Ca on Au, P3HT at 130 K and P3HT at 300 K. It is obvious from this representation that the Ca dose necessary to create a closed Ca film on top of the substrate is lowest for the Au, followed by P3HT at 130 K; the highest amount of Ca is necessary to completely cover a P3HT surface at 300 K. This is in line with the expectation that diffusion of Ca is hindered on the

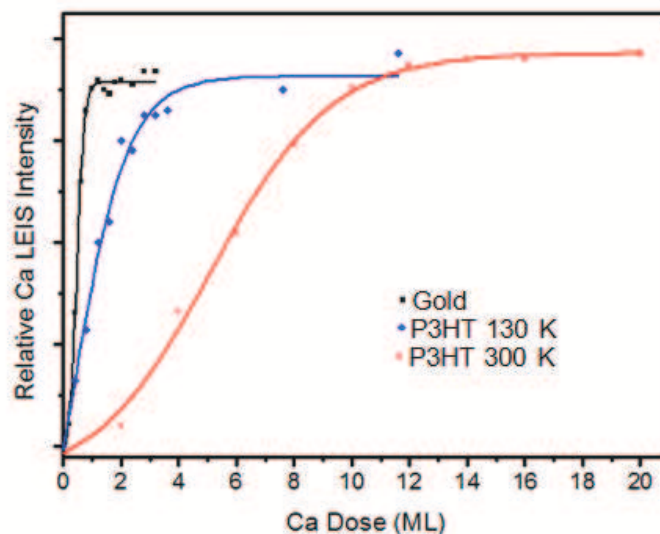


Figure 7.4: Relative LEIS Ca intensity as a function of dose for Ca deposition on Au (black squares), P3HT at 130 K (blue diamonds) and 300 K (red open circles).

P3HT surface held at 130 K and the Ca overlayer therefore forms a closed film at lower coverages compared to a P3HT surface at 300 K. As the sticking probability of Ca on P3HT is supposedly higher at 130 K compared to 300 K, the effect would appear less drastic in a plot of LEIS intensity versus coverage than Figure 7.4 may suggest. However, best comparison between the LEIS data are achieved with the plots as a function of dose, simply because sticking probability data is not available for all three samples. This allows to conjecture that the decrease in thickness of the reacted layer after deposition of Ca at 130 K is not due to lack of available Ca, as the same amount was deposited in both cases (see Figures 7.1 and 7.2).

Further support for this information is provided by the XP spectra of the Ca 2p region shown in Figure 7.5a and 7.5b: the spectra recorded at 130 K after Ca was deposited at the same temperature clearly show the fingerprint of metallic Ca. The high intensity of the satellite at approximately 8.2 eV higher binding energy compared to the Ca 2p_{3/2} peak and the large spin-orbit splitting of 3.8 eV are clear indications for metallic Ca. ^[221,222] Upon warming the sample to 300 K, the spectra 7.5c and 7.5d exhibit another feature at a binding energy approximately 1 eV higher than the feature ascribed to metallic Ca, which is especially visible in the Ca 2p_{3/2} peak. This new feature is ascribed to reacted Ca. Its intensity relative to the signal of metallic Ca is highest in normal emission (0°), confirming that the reacted Ca is indeed below the metallic Ca, i.e., at the interface to the polymer. Especially in

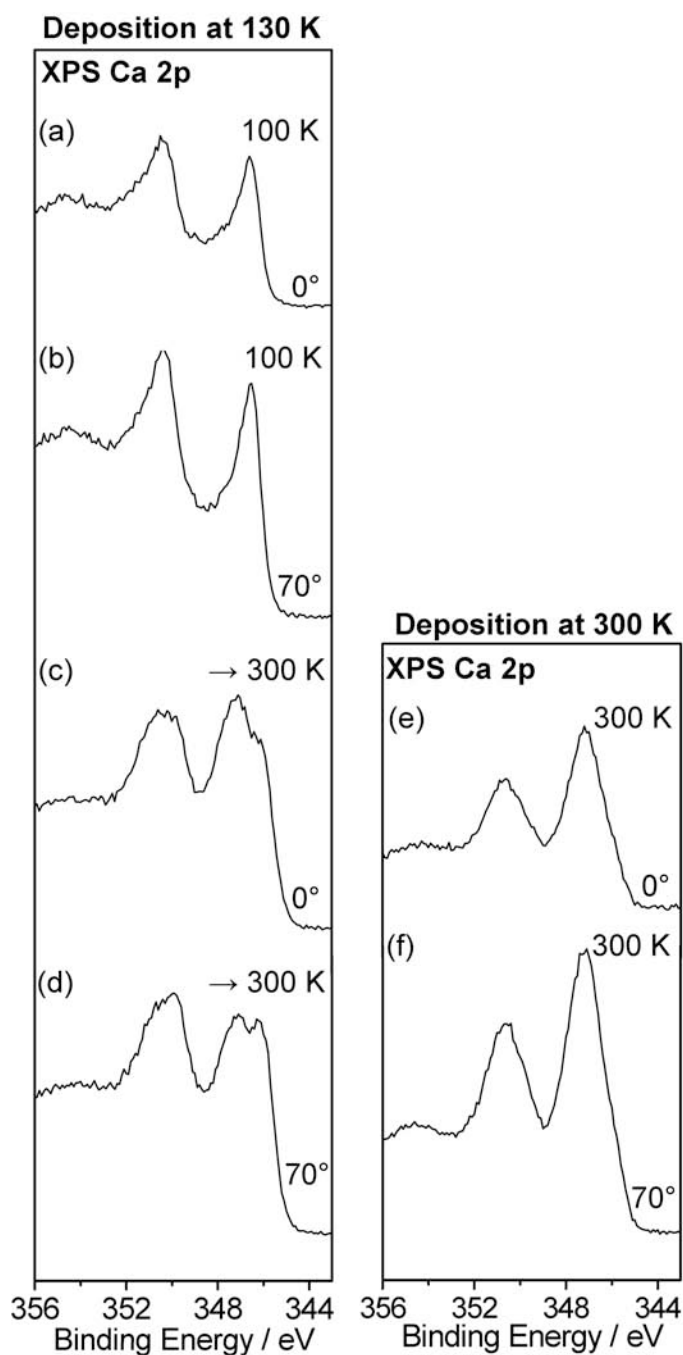


Figure 7.5: XP spectra of the Ca 2p region. On the left side, spectra recorded after Ca deposition at 130 K are displayed: at 130 K under normal (a) and 70° emission (b) and after the sample was warmed up to 300 K under normal (c) and 70° emission (d). On the right side, spectra after Ca deposition at 300 K in normal (e) and 70° (f) emission are shown for comparison.

comparison with the spectra 7.5e and 7.5f recorded after Ca deposition on P3HT at 300 K, it is obvious that a substantial amount of metallic Ca is present in the sample prepared at 130 K, even after heating it up to room temperature. These observations exclude the possibility that the depth of the reacted layer is limited for this preparation route by lack of metallic Ca for further reaction. It shall be noted here that the strong satellite of the Ca $2p_{3/2}$ line significantly affects the shape and even the apparent size of the Ca $2p_{1/2}$ peak – in spectrum 7.5a the corresponding peak height appears even larger than for the Ca $2p_{3/2}$ peak. Therefore, it seems advisable to concentrate on the unperturbed Ca $2p_{3/2}$ peak in the evaluation of the presented spectra.

The LEIS data in Figure 7.4 also supports this notion of availability of metallic Ca not being the limiting factor, as they indicate that the dose of Ca is sufficient to form extensive clusters or even a closed film on top of the polymer. These observations have two important implications. First, they confirm the model that subsurface diffusion occurs predominantly only before Ca clusters have formed on the surface. This is also in agreement with previous observations that the degree of diffusion can be influenced by the deposition rate of the metal, since a high deposition rate is likely to favor cluster formation.^[170] Second, the results presented above strongly suggest to perform metal deposition at low temperatures when the aim is to obtain as sharp a metal-polymer interface with as little subsurface diffusion and reaction as possible.

These findings directly induce the next questions: why is diffusion and reaction not completely prevented by low-temperature deposition (some reaction still occurs when the temperature is raised to 300 K) and what could be done to achieve this? The most likely reason is that the low-temperature deposition of Ca leads initially to the formation of dendritic Ca structures with a large fraction of highly undercoordinated Ca atoms. Such a growth behavior is typical of metal nucleation and growth under extreme non-equilibrium conditions.^[223–226] The undercoordinated metal atoms have a much lower binding energy than regular surface or interface atoms. If the temperature is increased, those undercoordinated Ca atoms can detach easily from the Ca structures and diffuse into the polymer, where they react with the thiophene units. This consideration suggests that there is an optimum substrate temperature during deposition: it should be sufficiently low to suppress diffusion of the Ca atoms into the polymer, but at the same time it should allow for a certain degree of sintering of the Ca structures, such that the amount highly

undercoordinated metal atoms is kept to a minimum. This optimum deposition temperature obviously depends on the polymer as well as the metal. However, it appears likely that knowledge of the energetics of the respective interface formation, e.g., from calorimetric studies, with information on the sintering behavior of the metal deposited (which is known for a large number of relevant metals, already) can be used as an efficient guide determining the optimum deposition temperature rather easily for different interfaces.

7.2 Conclusions

It was shown that the deposition of Ca on P3HT at 130 K results in a sharper interface and less reaction between metal and polymer compared to deposition at 300 K under otherwise identical conditions. The differences in the interface structure and composition persist to a large extent after warming up to room temperature, which makes the approach very interesting for practical applications. In combination with other parameters that influence the interface morphology, such as deposition rate, an optimization of the deposition temperature for individual metal/polymer combinations provides a strong tool for the precise control of chemistry and morphology of metal-polymer interfaces.

8 Ca Adsorption on CN-MEH-PPV

Alike P3HT, poly[2-methoxy-5-(2-ethylhexyloxy)-1,4-(1-cyanovinylene)phenylene] (CN-MEH-PPV) is an interesting material for organic electronic devices. The electroluminescence in the green spectral region (577 nm) renders the material very interesting for the use in OLEDs, where the Ca/polymer interface, again, plays a very important role (compare Chapters 5 to 7).

Apart from its interesting properties with respect to potential applications, CN-MEH-PPV may serve as a good comparison for our studies performed on P3HT. Since it contains two different types of hetero atoms, nitrogen and oxygen, it will allow us to find general trends in the interface formation behavior of Ca and hetero-atom containing, π -conjugated polymers.

The interface formation of Ca vapor-deposited onto CN-MEH-PPV has been studied using the same experimental tools as were used in the previous studies on P3HT: LEIS, atom beam scattering, adsorption calorimetry, and XPS. The samples were prepared very similarly to the routine for the preparation of thin films of P3HT: The polymer is spin coated from a 0.5 % w/w solution in chloroform directly onto the pyroelectric detector sheet for calorimetric studies or onto 0.1 mm thick aluminium foil for XPS investigations.

Due to the complexity of the interface formed and unexpected behaviour of this system, several points could not be elucidated completely, so far. Therefore, the results presented in this chapter are to be viewed as preliminary, as is also pointed out in the summary and outlook (Sections 9.1 and 9.2).

8.1 Results and Discussion

8.1.1 LEIS

In Figure 8.1, the relative Ca LEIS intensity is plotted as a function of Ca coverage for deposition temperatures of 130 K and 300 K, along with a dashed line representing the intensities expected for layer-by-layer growth. One can easily recognize the substantial deviation from layer-by-layer growth for both temperatures; while

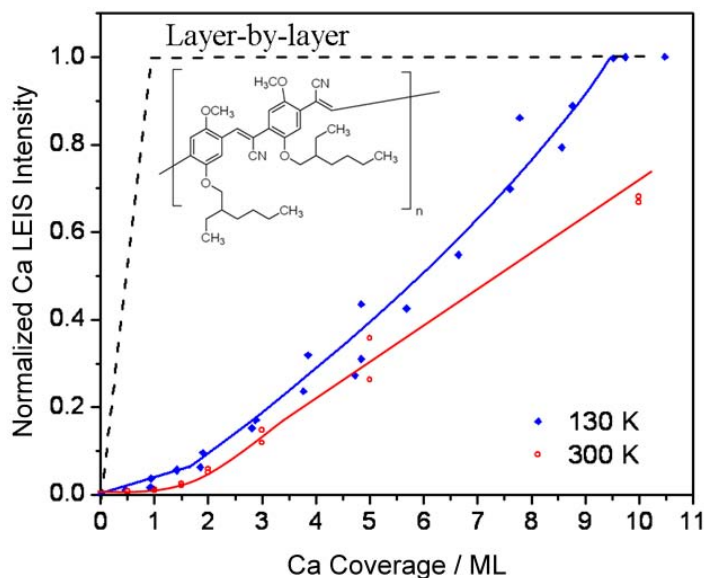


Figure 8.1: Ca LEIS intensity as a function of coverage for Ca deposition at 130 K (blue diamonds) and 300 K (red hollow circles). The solid blue and red lines are only guides for the eye, the trace expected for layer-by-layer growth is indicated by the dashed black line. In the inset, the structure of CN-MEH-PPV is shown.

Ca deposited at 130 K forms a closed layer above a coverage of 9.5 ML, it takes a significantly higher coverage to achieve the same at 300 K. (Unfortunately, the measurements at 300 K were not continued until saturation was reached.) A similar behavior was observed before in the case of Ca deposition on P3HT. Therefore, a very similar interpretation is here proposed: initially, Ca atoms may diffuse into the subsurface region or form islands atop the polymer. These clusters grow in size and form three dimensional particles, which coalesce into a closed film at high coverage, indicative of large heights of the respective particles. This may be intuitively interpreted as an indication that the surface is not very reactive towards Ca, as impinging Ca atoms obviously prefer interaction with other Ca atoms in clusters. Especially in conjunction with the results for differently treated P3HT surfaces (pristine and electron-irradiated), the LEIS results for CN-MEH-PPV suggest a general trend in the growth model: interaction with the species forming the top layer of the polymer surface is rather weak. It appears likely that for both P3HT and CN-MEH-PPV, saturated hydrocarbon chains terminate the surface on the vacuum side. Deposition of Ca at lower temperature increases the density of clusters formed on the surface, which is very likely an effect of the decreased diffusion of impinging Ca atoms. This higher cluster density in turn leads to formation of a closed layer at a

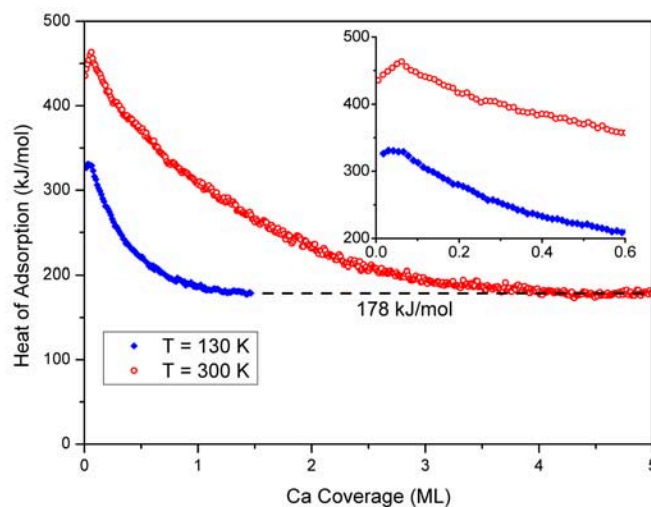


Figure 8.2: Heat of adsorption as a function of Ca coverage for Ca deposition at 130 K (blue diamonds) and 300 K (red hollow circles). The inset displays the low coverage region in more detail.

lower coverage compared to Ca deposition at higher temperatures with accordingly decreased cluster density.

8.1.2 Heats of Adsorption

The heats of adsorption for Ca deposited on CN-MEH-PPV held at 130 K and 300 K, respectively, are shown in Figure 8.2. On the cold polymer (130 K), the initial heat of adsorption amounts to 330 kJ/mol. This value quickly decreases with coverage until the bulk heat of adsorption for Ca (178 kJ/mol) is reached at a coverage of around 1 ML.

In the case of Ca deposition at 300 K, the heat of adsorption curve is significantly different from the one discussed above. The initial heat of adsorption is 430 kJ/mol. It increases up to a value of 460 kJ/mol at 0.1 ML coverage, a change occurring in parallel with the increase in sticking probability. From the maximum heat of adsorption value, the heat of adsorption decreases and finally reaches the bulk heat of sublimation of Ca (178 kJ/mol) at around 4 ML Ca coverage.

The curve for 300 K can be explained with a two-site model, which successfully describes the situation of Ca adsorption on PMMA: except for the very low coverage regime below 0.1 ML, where defect sites seem to play a role adsorbing Ca atoms can either react with the polymer or form/add to 3D Ca particles.^[120] In contrast to Ca adsorption on P3HT (see Chapter 5), the heat of adsorption does not exhibit

a plateau but drops immediately after peaking at approximately 0.1 ML. Such a behavior is a hint that the formation of clusters occurs from the onset of Ca deposition on, because the only explanation for a decreasing heat of adsorption within this model is that the pathway with the lower heat (here: formation of Ca clusters, 178 kJ/mol) plays an increasing role. The fact that cluster formation occurs already at very low coverages makes it difficult to assign a correct heat of formation for the process with the higher heat, because it is unclear how the adsorbing Ca atoms are distributed over the two channels. Therefore, the heat of reaction of the more exothermic process is at least 460 kJ/mol but possibly higher, if cluster formation occurs already at the lowest coverages.

However, based on entropy considerations, it appears unlikely that cluster formation plays a significant role at very low coverages. It is thus reasonable to identify the maximum measured heat of 460 kJ/mol with the more exothermic, reactive pathway. With this assumption, the two-site-model makes it possible to determine the amounts of Ca in each of the two reaction channels from the heat of adsorption curve: the measured heat of adsorption is nothing else but the sum of the two heat of adsorption values assigned to the different pathways weighted with the fraction of Ca atoms adsorbing via either one of the two pathways. The proper analysis of the heat of adsorption curve yields an amount of 1.1 ML Ca that reacts via the reactive route, i.e., exhibiting a heat of adsorption of 460 kJ/mol. As this heat of adsorption must be regarded a lower limit as discussed above, the calculated amount of reacted Ca must be considered an upper limit, accordingly.

In this context, the presence of a plateau for Ca deposition of Ca onto P3HT poses a very significant difference with respect to Ca-deposition on CN-MEH-PPV considered here. On P3HT, the existence of the plateau region made it reasonable to assume that Ca exclusively reacted with S atoms in the polymer up to a coverage of 0.6 ML. Thus, the assignment of the corresponding heat of adsorption and the total amount of reacted Ca was straight. It was found that a higher amount of Ca, 1.6 ML, reacts with P3HT, compared with at most 1.1 ML on CN-MEH-PPV.

While the fraction of Ca atoms adding to clusters increases with coverage, the fraction reacting with the polymer correspondingly decreases. At 4 ML, Ca adds only to islands and eventually to a closed film, as evidenced by the observed heat of adsorption of 178 kJ/mol, which matches the bulk heat of adsorption of Ca. The notion that cluster formation and growth starts out at the very beginning of the experiment also helps to account for the high initial sticking probability compared

to unmodified P3HT, for example (see Section 8.1.3).

Ca deposition at 130 K leads to a lower initial heat of adsorption than deposition at 300 K. On the basis of the two-site model (i.e., assuming that the same processes occur as at 300 K), this indicates that formation of Ca clusters must occur already at the lowest coverages to a significantly larger extent and that the fraction of Ca atoms reacting with the polymer is rather small: only 0.2 ML based on the analysis described above. At this temperature, the heat of sublimation of Ca is reached already at ~ 1.5 ML coverage, indicating that cluster growth outcompetes the reactive pathway much faster in this case, which is in perfect agreement with the interpretation given above and the sticking probability data in Section 8.1.3.

Based on the maximum heat of adsorption value observed, a possible reaction pathway for the interaction between Ca and the polymer is the formation of CaO by cleavage of the ether groups. For comparison with thermodynamic data from the literature, the standard reaction enthalpy for the following reaction was calculated:



This reaction was chosen because it represents the most closely related case for which thermodynamic data are available. It yields a standard reaction enthalpy of 559 kJ/mol. The maximum measured heat of adsorption is 460 kJ/mol, significantly lower than the value obtained in the calculation for the model reaction. This difference may be explained with formation of small CaO clusters. Such small clusters are usually less stable than the respective bulk material, which was assumed in the calculation. In fact, the situation for Ca deposition on P3HT (see Chapter 5) was very similar, only that there CaS clusters were formed there.

8.1.3 Sticking Probability

The sticking probability is displayed as a function of coverage in Figure 8.3. Again, data were recorded for deposition temperatures of 130 K and 300 K. At 130 K, the initial sticking probability for Ca on CN-MEH-PPV amounts to 0.92. It increases monotonously and reaches unity around 1.5 ML. As the Ca film is not closed until a coverage of approximately 9.5 ML according to the LEIS data presented above (see Section 8.1.1), this suggests that a very high number of Ca clusters is formed and, as a result, impinging atoms are efficiently captured even before the surface is completely covered with a Ca film.

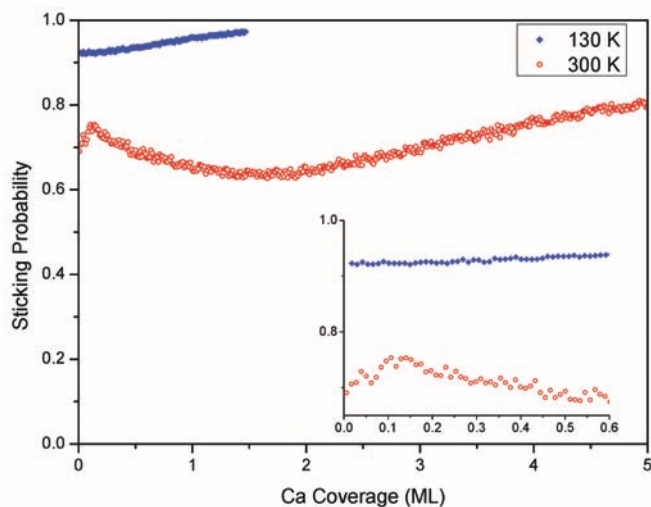


Figure 8.3: Sticking probability for Ca deposition at 130 K (blue diamonds) and 300 K (red open circles). The inset shows the low coverage region in more detail.

The situation is different for Ca deposition at 300 K: from the initial value of 0.69, the sticking probability increases to about 0.75 by 0.1 ML. Then, the sticking probability decreases again until a minimum value of 0.62 is reached at 1.5 ML. After this, the sticking probability slowly increases, again. The simplest model explaining this trace is the following: initially, the impinging Ca atoms are predominantly trapped by defect sites and engage in a reaction with the polymer.

These defect sites seem to act as nucleation sites for Ca clusters, but exhibit a lower sticking probability (note the lower heat of adsorption in this coverage region, as can be seen in the data in Section 8.1.2) than the reactive site for Ca adsorption in the polymer. Their number seems to be quite low, as both the heat of adsorption and the sticking probability peak at a coverage of only 0.1 ML. Beyond this coverage, the sticking probability starts decreasing slightly, presumably because a high fraction of reactive sites on the surface has already reacted and such sites deeper in the polymer are not as readily available. The clusters formed on the surface are not yet large enough to have an impact on the sticking probability until a coverage of about 1.5 ML is reached. Then, their size seems to be large enough to capture an increasing amount of impinging Ca atoms, which leads to an increase in the sticking probability. This interpretation is supported by the heat of adsorption, too.

Although the trace can be explained with a reasonable model, there remains a critical point to discuss: the sticking probability does not reach unity until very

high coverages. (In fact, the measurements were unfortunately not continued until unit sticking probability was reached.) In conjunction with the heat of adsorption data suggesting that Ca is not reacting with the polymer to a significant amount above a coverage of 4 ML, this points to extremely tall Ca islands.

Two interesting aspects shall be discussed in comparison with the sticking probability of Ca on P3HT. First, the initial sticking probability on CN-MEH-PPV is significantly higher than on P3HT. A reasonable explanation is to attribute this to a lower barrier for reaction with the reactive site or an intrinsically higher probability for cluster formation, for example caused by a larger mobility of adsorbed Ca atoms. Second, the decrease in sticking probability at medium coverages (0.1 ML to 1.5 ML) for deposition on CN-MEH-PPV is peculiar. One can think of two effects playing a role in this: the reaction may proceed such that, in order to react, Ca atoms must take a reaction route with a higher activation energy, which in turn would lead to a higher probability for desorption. For example, the two non-equivalent oxygen species in the polymer may exhibit slightly different activation barriers towards formation of CaO and thus contribute to the observed effect. An alternative explanation is that chemical/structural changes lead to weaker bonding of the precursor state. In this context, it is proposed that the formation of CaO makes the polymer more polar and thus creates an energetically unfavourable environment for the non-polar hydrocarbon chains sticking, which consequently protrude out of the surface. An influence of the reaction of Ca with the polymer on the sticking probability was also suggested in the results for P3HT presented in Chapter 5, only that there the resulting change in sticking probability was in the opposite direction, i.e., the sticking probability increased.

8.1.4 X-ray Photoelectron spectroscopy

XPS investigations were performed at 300 K in order to identify the species within the polymer reacting with the dosed Ca. As previous work has shown that the interaction between Ca and carbon atoms in the polymer is only very weak, the focus was put on the hetero atoms. No significant changes could be observed in the N 1s region upon Ca deposition, while the O 1s region shows substantial changes with increasing Ca coverage, as can be seen in Figure 8.4. In the spectrum of the pristine polymer, only one main feature with a binding energy of approximately 534.6 eV is visible. With increasing Ca coverage, a second feature emerges, initially at a binding energy of ~ 533 eV. At still higher coverages, yet another contribution

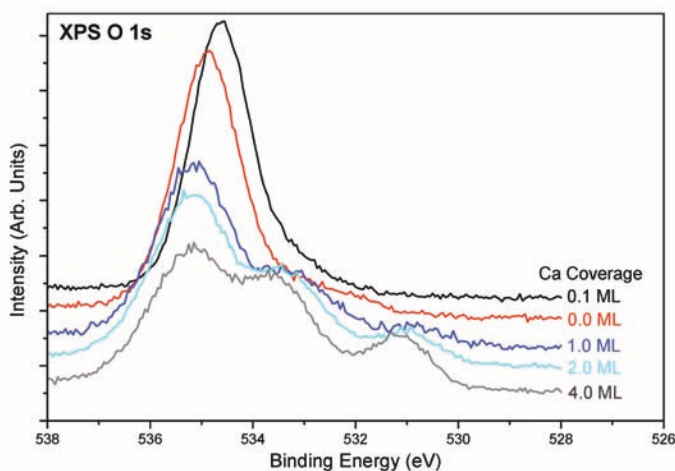


Figure 8.4: XP spectra of the O 1s spectra recorded after incremental doses of Ca onto CN-MEH-PPV at 300 K.

at a binding energy of approximately 531 eV appears in the spectra. This third feature is most likely due to contaminations arising from the residual gas, as the coverage at which this feature emerges is beyond the coverage at which a significant amount of impinging Ca reacts with the polymer according to the heat of adsorption data. In addition, the feature grows dramatically between Ca coverages between 2 ML and 4 ML: in this coverage regime, the dominating process is the growth of Ca islands. This complication demonstrates the difficulties in clearly assigning the reactive species in cases, where similar species may originate from residual gases. For the polymer investigated in Chapters 5 to 7, P3HT, it was much easier to monitor the reaction progress with XPS, as the reactive species in that case was sulfur and therefore a contamination from the background with similar species could be excluded. Nevertheless, combining the heat of adsorption data with the XP spectra presented certainly support the interpretation that the reactive species in CN-MEH-PPV towards Ca is indeed oxygen.

The general shifts observed for all oxygen species are attributed to band bending effects, as they are visible in the C 1s features as well. This effect has also been observed during the formation of similar interfaces, for example the interface between Ca and P3HT presented in Chapters 5 to 7.

8.2 Conclusions

In this chapter, the interface formation between CN-MEH-PPV and Ca (vapor-deposited under UHV conditions) is addressed using LEIS, atomic beam scattering, adsorption calorimetry and XPS. Combining the various experimental results, suggests the following picture of the interface formation process at a substrate temperature of 300 K: apart from a small number of defect sites, impinging Ca atoms may either react with an oxygen atom from the ether groups of the polymer to form CaO or form Ca clusters on the surface. Heat of adsorption and sticking probability suggest that both of these processes are relevant from zero coverage on. However, while the contribution of the reaction with the polymer diminishes with coverages, the respective contribution of cluster growth of Ca on top of the polymer increases. At 4 ML coverage, Ca reacts exclusively with Ca already present on the surface. (However, the surface is not completely covered with Ca yet, as indicated by LEIS, and the low sticking coefficient of ~ 0.8 ML shows that diffusion of Ca atoms on the polymer surface is sufficiently slow that some of the trapped Ca atoms can desorb before they bind to a Ca cluster.) The total amount of Ca that reacts with oxygen within the polymer is estimated to be around 1.5 ML, which implies that diffusion of Ca below the surface occurs.

Ca deposition at 130 K leads to qualitatively very similar results. However, cluster formation occurs immediately (i.e., already at very low coverages) and is greatly enhanced at the expense of reaction with oxygen of the ether groups and correspondingly formation of CaO. This is visible as a greatly reduced heat of adsorption and a markedly higher initial sticking probability. Ultimately, only 0.2 ML of Ca react with the polymer. A comparison of these results with the interface formation between Ca and P3HT shows that there are a number of similarities: the kinetic competition between two reaction pathways, the presence of a specific species within the polymer that is reactive towards Ca adsorption (sulfur and oxygen, respectively). One may also notice that the effect of deposition of Ca at a low substrate temperature generally leads to reduced diffusion below the surface and an increased amount of Ca in clusters on top of the surface in the low coverage regime. The differences are obvious, as well: the energetics of the reaction between Ca atoms and the respective reactive species within the polymer differs substantially in the two cases considered in this work, as well as the total amount of Ca reacting with such reactive sites, 1.1 ML for CN-MEH-PPV compared to 1.6 ML for P3HT (at 300 K).

9 Summary and Outlook

9.1 Summary

The interface formation between Ca and two different semiconducting, π -conjugated polymers, namely poly(3-hexylthiophene) (P3HT) and poly[2-methoxy-5-(2-ethylhexyloxy)-1,4-(1-cyanovinylene)phenylene] (CN-MEH-PPV), was investigated using adsorption microcalorimetry, LEIS, atomic beam scattering and XPS. In addition to the interface formation on pristine, i.e., untreated polymer surfaces, the influence of electron irradiation prior to Ca deposition and of the substrate temperature during deposition was studied.

In the first chapter, adsorption calorimetry is introduced: its development as an important technique for the study of adsorption enthalpies and the most recent technical improvements are briefly reviewed. In comparison with other experimental methods for determining adsorption enthalpies, the great advantage of adsorption microcalorimetry becomes obvious: its applicability to irreversible adsorption systems, which is crucial for the investigation of metal-polymer interfaces.

Despite the tremendous advances on the technical side of adsorption calorimetry, further developments are necessary in order to expand the range of systems that can be studied. Along this line, a number of crucial improvements over existing calorimetry setups, which are a prerequisite for studying the adsorption of large organic molecules on single crystal surfaces, are presented in Chapter 3. Especially the high IR-emissivity of large organic molecules is problematic. A very compact molecular beam source, along with a specially designed optical system, as introduced in Chapter 3, helps solving this problem. All of these improvements are incorporated into the calorimeter currently under construction at the University of Erlangen.

The two polymers are described in detail in Chapter 2, where also the experimental setups used for this work are presented. Due to their outstanding electrical properties paired with good and cost-efficient processability, P3HT and CN-MEH-PPV are employed in organic electronic devices, such as organic solar cells or organic light emitting diodes (OLEDs). The interface between the respective polymers and metallic electrodes is known to be decisive for the device performance. However,

little is known about the interface formation on a fundamental level. The current state of knowledge is summarized in Chapter 4.

These chapters set the stage for the main part of this work, the experimental investigation of two of such important interfaces using adsorption microcalorimetry, delivering the first results concerning the energetics of the interface formation for such systems, and photoelectron spectroscopy: the Ca/P3HT and the Ca/CN-MEH-PPV interface.

The reactive site for the interaction for Ca atoms impinging on a pristine P3HT surface (Chapter 5) appears to be the sulfur in the thiophene ring, as is concluded from a combination of XPS, adsorption calorimetry and theory results. The interaction, in fact, is strong enough that the sulfur atom is abstracted from the thiophene ring under formation of CaS. The overall reaction energy of this process is 405 kJ/mol. As the sticking probability in the low-coverage regime is rather small, initially only 0.35, there obviously exists a substantial activation barrier in this reaction pathway. In spite of this barrier for the reaction of Ca with P3HT, cluster formation as the competing process does not occur at very low coverages. At higher Ca coverages, cluster formation sets in and becomes the predominant process above 3 ML. This is accompanied by an increase in the sticking probability of Ca atoms and a decrease in heat of adsorption. XPS analysis of the depth up to which the sulfur atoms in P3HT react with Ca suggests that this reacted layer reaches a thickness of only 3 nm, irrespective of additional Ca deposition. A closed Ca layer is formed on the surface at a coverage of approximately 11 ML.

In Chapter 6, the effect of electron-irradiation on P3HT and the interface formation with subsequently dosed Ca is discussed. Irradiation of the sample with electrons having a kinetic energy of 100 eV results in hydrogen abstraction from the hexyl chains of the polymer, which is manifested in XP spectra of the C 1s region. The ratio of saturated to unsaturated carbon is changed from 3:2 before irradiation to 1:2 afterwards. This effect does not change the reaction of Ca with the polymer qualitatively. From the results presented in Chapter 5, this behavior was expected, as the Ca atoms react with the thiophene units rather than with the hexyl chains. Even the ultimate reaction depth is not changed with respect to the pristine surface. In contrast, the sticking probability of Ca is dramatically increased to 0.63. This effect is ascribed to a stronger attachment of the adsorption precursor state to C=C double bonds, which are formed as a result of electron-induced hydrogen abstraction. Another parameter that influences the Ca/P3HT interface morphology is the depo-

sition temperature, as was discussed in Chapter 7. Adsorption at low temperatures (130 K) reduces the diffusion of Ca below the surface and the reaction of Ca with S greatly. Heating the sample to room temperature after low-temperature Ca deposition leads to diffusion of Ca atoms into the bulk and reaction with S, but only to a limited extent. The thickness of the reacted layer deduced from XP spectra only amounts to 1.5 nm, which is about 50 % of the thickness observed for deposition at room temperature. So far, this is the first demonstration that a “sharper” interface which is produced at low temperature persists after warming the sample to room temperature. Obviously, the Ca atoms show less tendency to react with the polymer, once they have been incorporated into larger clusters or closed films.

The interface of Ca evaporated onto CN-MEH-PPV is the subject of Chapter 8. Again, it is possible to identify the reactive species in the polymer. In this case, this species proves to be the oxygen of the ether groups. Different from Ca deposition on P3HT, formation of Ca clusters on top of the polymer starts at the very beginning of the interface formation, as the heat of adsorption drops immediately after peaking at approximately 0.1 ML. One of the consequences is that the initial sticking probability is much higher compared to P3HT, which may be due to a lower activation barrier or the existence of two adsorption channels (reaction and cluster formation) even at very low coverages. However, the present results leave some questions unanswered: the LEIS and sticking probability data suggest cluster heights normally considered unreasonable. Here, a more thorough investigation of the morphology of the Ca particles formed on top of the polymer employing scanning electron microscopy or atomic force microscopy as well as additional LEIS experiments will lead to a clearer picture on the situation. Furthermore, although XPS investigations point to oxygen being the reactive species towards adsorption of Ca on CN-MEH-PPV, a concise analysis is obstructed by contaminations arising from residual gas in the analysis chamber in combination with long acquisition times.

Overall, studies on the interfaces of Ca with semiconducting polymers such as P3HT and CN-MEH-PPV demonstrate that such interfaces present very complex systems, indeed: great care must be taken ensure sufficiently good experimental conditions and when interpreting the results.

9.2 Outlook

The study of these two interfaces and different ways to influence these interfaces have led to a wealth of new insights, also with respect to practical applications. Especially for the experimentally more challenging interface, the Ca/CN-MEH-PPV interface, a number of points need further attention. In the meantime, extensive alterations have been made to the X-ray photoelectron spectrometer, including installation of a new electron detector and the connected electronics. These alterations promise significantly faster data acquisition times and therefore additional XPS experiments are expected to deliver a better data set for a more quantitative analysis.

Another field for future work certainly includes the study of other metals deposited on the polymers addressed in this work. Aluminum, which is also a common cathode material in working devices, is a very promising candidate in elucidating the influence of the metal on the interface. In this context, UPS may be used to evaluate the influence on electronic structure of the resulting interfaces and potentially correlate them with the other results presented in this work.

The results obtained so far present a good starting point for investigating a technologically very interesting type of interface: the interface between metals and polymer blends, which are already used in highly efficient devices. However, without a good understanding of interfaces between single component polymers and metals, such interfaces are too complex to be studied successfully.

10 Zusammenfassung und Ausblick

10.1 Zusammenfassung

Die Ausbildung der Grenzschicht zwischen Kalzium und zwei technologisch äußerst interessanten halbleitenden, π -konjugierten Polymeren wurde unter besonderer Berücksichtigung ihrer Energetik und Morphologie untersucht. Dabei kamen Adsorptions-Mikrokalorimetrie, niederenergetische Ionenstreu-spektroskopie (LEIS), Atomstrahlstreuung und Röntgenphotoelektronenspektroskopie (XPS) zum Einsatz. Die Grenzschicht wurde durch Aufdampfen von Kalzium auf die Polymeroberflächen im Vakuum hergestellt. Bei den zwei untersuchten Polymeren handelt es sich um Poly(3-hexylthiophen) (P3HT) und Poly[2-methoxy-5-(2-ethylhexyloxy)-1,4-(1-cyanovinyl)phenyl]. Die Untersuchungen beschränkten sich dabei nicht auf das Studium der entsprechenden Grenzschichten auf den unbehandelten Polymeren; zusätzlich wurden auch der Einfluss von Elektronenbeschuss des Polymers vor dem Aufdampfen und der Einfluss der Substrattemperatur während des Aufdampfens von Kalzium untersucht.

Die Hauptuntersuchungsmethode, Adsorptions-Mikrokalorimetrie, wird in Kapitel 1 vorgestellt. In einem kurzen Abriss der historischen Entwicklung der Methodik werden die wichtigsten technischen Entwicklungen aufgezeigt und die eigentliche Messgröße, die Adsorptionsenthalpie, erläutert. Für die Untersuchung der in dieser Arbeit untersuchten Metall-Polymer-Grenzschichten ist vor allem die Anwendbarkeit von Adsorptions-Mikrokalorimetrie auf irreversible Adsorptionssysteme wichtig. Im Vergleich zu anderen experimentellen Methoden zur Bestimmung der Adsorptionsenthalpie ist dies ein Alleinstellungsmerkmal der hier verwendeten Methode.

Technische Neuentwicklungen haben der Adsorptionskalorimetrie durch die damit verbundene Erschließung neuer, interessanter Systeme in der Vergangenheit ein steigendes wissenschaftliches Interesse verschafft (gemessen an der Zahl der Publikationen je Zeiteinheit). Besonders bedeutend war der Schritt zur Verwendung von einkristallinen Proben. Trotz der gemachten Fortschritte werden weitere experimentelle Verbesserungen immer wieder notwendig, um neuartige Systeme überhaupt untersuchen zu können. Zu dieser Gruppe von Systemen zählt beispielsweise die

Adsorption großer organischer Moleküle auf Einkristallen. Die Problematik dabei ist in der hohen Emissivität der Moleküle im IR-Bereich begründet. Diese führt dazu, dass in kalorimetrischen Experimenten ein erheblicher Teil des Signals durch auf den Detektor treffende Wärmestrahlung hervorgerufen wird. Um diese Probleme zu umgehen, wurde eine sehr kompakte Molekularstrahlquelle mit einem passenden Spiegelsystem, das eine Trennung der adsorptions- und strahlungsinduzierten Signalanteile ermöglicht, entworfen. Diese Entwicklungen werden in Kapitel 3 vorgestellt und sind Teil des in Erlangen im Aufbau befindlichen Adsorptions-Kalorimeters.

Die zwei in dieser Arbeit verwendeten Polymere sowie die verwendeten Apparaturen werden in Kapitel 2 beschrieben. Die Polymere finden aufgrund ihrer elektronischen Eigenschaften, gepaart mit guter Verarbeitbarkeit, Anwendung in elektronischen Bauteilen: P3HT wird in organischen Solarzellen, CN-MEH-PPV in organischen Leuchtdioden (OLEDs) eingesetzt. In solchen Anwendungen spielt gerade die Grenzfläche zwischen den aktiven Materialien – den genannten Polymeren – und den (metallischen) Elektroden eine entscheidende Rolle für die Leistungsfähigkeit der entsprechenden Bauelemente. Trotzdem ist über die elementaren Prozesse bei der Ausbildung dieser Grenzschichten wenig bekannt, insbesondere über deren Energetik. Der aktuelle Forschungsstand diesbezüglich ist in Kapitel 4 zusammengefasst. Diese einführenden Kapitel bilden die Grundlage für den Hauptteil der Arbeit, der experimentellen Untersuchung der Ca/P3HT und Ca/CN-MEH-PPV Grenzschichten. Die hier vorgestellten kalorimetrischen Ergebnisse sind die ersten ihrer Art für solche Systeme und werden durch XPS-, LEIS- und Atomstreuexperimenten ergänzt. Thema von Kapitel 5 ist die Ausbildung der Grenzschicht zwischen Kalzium und unbehandeltem P3HT. Die Untersuchungen zeigen, dass die in Bezug auf die Adsorption von Ca-Atomen reaktive Spezies im Polymer der Schwefel in den Thiophenringen ist. Die Wechselwirkung zwischen Ca- und S-Atomen ist dabei so stark, dass Schwefel unter Bildung von Calciumsulfid (CaS) aus dem Thiophenring abstrahiert wird. Dabei beträgt die Reaktionsenthalpie des Gesamtprozesses 405 kJ/mol. Der mit 0,35 sehr niedrige Haftkoeffizient bei geringer Ca-Bedeckung lässt auf das Vorhandensein einer erheblichen Reaktionsbarriere schließen, die jedoch nicht dazu führt, dass Ca-Cluster gebildet werden. Solche Ca-Cluster treten erst bei höheren Bedeckungen auf und Clusterwachstum wird bei einer Bedeckung oberhalb von 3 ML zum dominierenden Prozess. Mit dieser Verlagerung des vorherrschenden Prozesses gehen eine Verminderung der Adsorptionsenthalpie bis auf 178 kJ/mol (Sublimationsenthalpie von Kalzium) und eine Erhöhung des Haftkoeffizienten einher. Die Dicke der Schicht,

in der Ca-Atome mit Schwefel im Polymer reagieren, kann über eine quantitative Auswertung der XP-Spektren zu 3 nm bestimmt werden. Dieser Wert wird auch vom Verlauf der Adsorptionseenthalpie als Funktion der Ca-Bedeckung gestützt. Oberhalb einer Bedeckung von 11 ML ist schließlich die komplette Polymeroberfläche von einem geschlossenen Ca-Film bedeckt.

In Kapitel 6 werden die Auswirkungen von Elektronenbeschuss (kinetische Energie der Elektronen: 100 eV) von P3HT vor dem Aufdampfen von Kalzium auf die resultierende Grenzschicht diskutiert. Wie XP-Spektren der Kohlenstoffregion deutlich zeigen, resultiert der Elektronenbeschuss des Polymers in einer deutlichen Veränderung des Verhältnisses von gesättigtem zu ungesättigtem Kohlenstoff. Vor der Bestrahlung beträgt dieses Verhältnis 3:2, danach 1:2, was durch partielle Dehydrierung der Hexylketten verursacht wird. Die Reaktion zwischen Kalzium und Schwefel wird durch diese Veränderung nicht beeinträchtigt: die Adsorptionseenthalpie bei geringen Ca-Bedeckungen beträgt auch in diesem Fall 405 kJ/mol und auch die insgesamt mit dem Schwefel reagierende Kalziummenge bleibt mit 1,6 ML unverändert im Vergleich mit unbehandeltem P3HT. Eine deutliche Auswirkung haben die strukturellen Veränderungen infolge des Elektronenbeschusses auf den Haftkoeffizienten: dieser ist mit 0,63 bei niedrigen Bedeckungen deutlich höher im Vergleich mit dem unbehandelten Polymer. Eine Erklärung hierfür ist eine stärkere Wechselwirkung zwischen Ca-Atomen mit den, auf Grund des Elektronenbeschusses gebildeten, C=C Doppelbindungen, als mit den gesättigten Hexylketten.

Die Substrattemperatur während des Aufdampfens ist ein Parameter, der die Morphologie der Ca/P3HT Grenzschicht entscheidend beeinflussen kann, wie in Kapitel 7 dargelegt wird. Aufdampfen von Ca bei tiefen Temperaturen – das P3HT-Substrat wurde auf 130 K abgekühlt – führt zu einer deutlichen Verminderung der Reaktionszone von Ca- und S-Atomen. Selbst das Aufwärmen der Probe führt nur zu einer geringen Verbreiterung dieser Reaktionszone auf 1,5 nm, was in etwa der Hälfte der Dicke entspricht, die beim Raumtemperatur-Experiment auftritt (siehe Kapitel 5). Mit den vorgestellten Ergebnissen wurde erstmals gezeigt, dass sich schärfere Grenzschichten durch eine niedrige Substrattemperatur während des Aufdampfens herstellen lassen, wobei eine deutlich verminderte Ausdehnung der Reaktionszone auch bei anschließender Erwärmung auf Raumtemperatur erhalten bleibt. Offensichtlich ist die Barriere für Ca-Atome, einen bestehenden großen Cluster oder geschlossenen Film wieder zu verlassen um mit S-Atomen reagieren zu können, groß genug, um nennenswerte Reaktionen im Anschluss an das Erwärmen der Probe auf

Raumtemperatur zu verhindern.

Die Ca/CN-MEH-PPV-Grenzschicht ist Gegenstand von Kapitel 8. Wie im Fall von P3HT, gelingt es auch hier die reaktive Spezies in Bezug auf Ca-Adsorption zu finden: der Sauerstoff in den Ethergruppen des Polymers. Anders als bei P3HT deuten die experimentellen Befunde bei CN-MEH-PPV darauf hin, dass Clusterwachstum auf der Polymeroberfläche schon bei sehr niedrigen Bedeckungen einsetzt. Insbesondere der Verlauf der Adsorptionseenthalpie als Funktion der Bedeckung ist ein Indiz für ein frühes Einsetzen der Clusterbildung, da die Adsorptionseenthalpie im Gegensatz zu P3HT kein Plateau zeigt, sondern bei 0.1 ML ein Maximum aufweist und danach abfällt. Dieser Unterschied ist eine mögliche Erklärung für den im Vergleich zu P3HT höheren Haftkoeffizient, speziell bei geringen Bedeckungen. Weitere Faktoren, die den relativ hohen Haftkoeffizienten erklären, sind eine geringere Aktivierungsbarriere und damit verbunden das Vorhandensein zweier Adsorptionskanäle (Reaktion und Clusterbildung) selbst bei niedrigen Bedeckungen. Obwohl die Untersuchungen in einigen Bereichen zu einem guten Verständnis der Situation führen, bleiben andere Sachverhalte noch ungeklärt: so deuten die LEIS- und Haftkoeffizientmessungen auf ungewöhnlich hohe Ca-Partikel hin. Die geschätzte Höhe dieser Partikel ist sogar so groß, dass deren tatsächliche Existenz als fragwürdig erscheinen muss. In diesem Punkt sollten zusätzliche Experimente, beispielsweise mittels Transmissionselektronenmikroskopie (TEM) oder Rasterkraftmikroskopie (AFM), sowie weitere LEIS-Messungen für mehr Klarheit sorgen. Des Weiteren sind auch die XPS-Resultate aufgrund einer Verschmutzung aus dem Restgas noch nicht quantitativ verwertbar. Diese Problematik entsteht vor allem daraus, dass die untersuchte Spezies zum einen nur in relativ geringer Konzentration in der Probe vorhanden ist, was lange Messzeiten bedingt, aber andererseits eine Verschmutzung aus dem Restgas durch eine ähnliche Spezies (Wasser, CO, CO₂) nicht vollständig vermieden werden kann.

Insgesamt verdeutlichen die beiden betrachteten Grenzschichten zwischen Kalzium und P3HT bzw. CN-MEH-PPV sehr gut, wie komplex diese Systeme sind. Große Sorgfalt muss darauf verwendet werden ausreichend gute experimentelle Bedingungen herzustellen (was bei CN-MEH-PPV bisher nur teilweise gelungen ist). Auch müssen die Ergebnisse sorgfältig und vorsichtig interpretiert werden, da belastbare Aussagen meist nur durch Verknüpfung mehrerer Methoden zu erzielen sind.

10.2 Ausblick

Die Untersuchungen der beiden System Ca/P3HT und Ca/CN-MEH-PPV haben zu einer Vielzahl neuer Erkenntnisse geführt, die auch für reale Anwendungen von Bedeutung sind. Allerdings konnten gerade in Bezug auf die Grenzschichtbildung zwischen Kalzium und CN-MEH-PPV nicht alle Fragen geklärt werden, was vor allem auf experimentelle Schwierigkeiten mit diesem System zurückzuführen ist. Aufgrund zwischenzeitlich vorgenommener technischer Verbesserungen am Röntgenspektrometer (neuer Detektor und Elektronik) versprechen erneute Messungen bei deutlich verkürzter Messzeit eine deutlich bessere Datenbasis und werden vermutlich auch eine quantitative Analyse ermöglichen.

Weitere interessante Untersuchungen stellen sicherlich die Grenzschichten zwischen den untersuchten Polymeren und Aluminium dar, da dieses ebenfalls ein gebräuchliches Kathodenmaterial ist und sich gute Vergleichsmöglichkeiten mit den durchgeführten Experimenten ergeben. Um den Einfluss des Metalls auf die jeweilige Grenzschicht besser verstehen zu können bietet sich dabei auch Ultraviolett-Photoelektronenspektroskopie (UPS) an, um eine mögliche Korrelation zwischen elektronischer Struktur und anderen Eigenschaften der Grenzschicht aufzudecken.

Interessant ist mit Sicherheit auch die Ausweitung der untersuchten Grenzschichten auf Polymermischungen als Substrat. Für derartige Untersuchungen ist ein gründliches Verständnis der reinen Komponenten unerlässlich, da die Komplexität eines solchen Systems sonst zu groß wäre.

11 Danksagung

An dieser Stelle möchte ich all denjenigen meinen herzlichsten Dank aussprechen, die mich auf dem Weg zur Promotion während der letzten Jahre begleitet und unterstützt haben.

An vorderster Stelle gilt mein besonderer Dank Herrn Prof. Dr. Hans-Peter Steinrück für die freundliche Aufnahme in seine Arbeitsgruppe und die hervorragende Unterstützung in allen Belangen. Auch Herrn PD Dr. J. Michael Gottfried gilt mein besonderer Dank für die stets konstruktive und sehr fruchtbare Zusammenarbeit und insbesondere dafür, dass er mein Interesse an Adsorptions-Kalorimetrie geweckt hat (wofür er extra ins entfernte Clausthal-Zellerfeld reisen musste).

Meinen Mitstreitern in Sachen Kalorimetrie in Erlangen, Hans-Jörg Drescher und Ole Lytken, danke ich sehr herzlich für die exzellente Zusammenarbeit und die tolle Arbeitsatmosphäre im Labor. Beide haben auch, in verschiedenen Rollen, die verschiedenen Forschungsaufenthalte in Seattle zu einer sehr interessanten und insgesamt angenehmen Erfahrung werden lassen. In diesem Zusammenhang möchte ich mich auch bei den Kooperationspartnern an der University of Washington in Seattle bedanken. Von diesen sind insbesondere Prof. Charles T. Campbell, Dr. Jack H. Baricuatro, Jason Farmer, James Sharp und Dr. Junfa Zhu zu nennen, von denen ich viel gelernt habe. Für die Hilfe bei den durchgeführten XPS-Untersuchungen in Erlangen möchte ich mich bei Yun Bai und Martin Schmid bedanken.

Experimentelle Forschung kommt nicht ohne ein gehöriges Maß an technischem Support aus. Für die Vielzahl der in der mechanischen Werkstatt für das Kalorimeter gebauten Teile bedanke ich mich sehr herzlich bei Herrn Friedhold Wölfel und seinen Mitarbeitern. Bei elektronischen Problemen und der Entwicklung des Verstärkers war ich oft auf Hans-Peter Bäumler angewiesen, dem ich (nicht nur) deshalb zu großem Dank verpflichtet bin. Für seine organisatorische Unterstützung und Hilfe bei allen anderen technischen Problemen möchte ich Herrn Bernd Kress meinen Dank aussprechen.

Für das insgesamt hervorragende Klima innerhalb des Arbeitskreises möchte ich mich bei allen Mitarbeiterinnen und Mitarbeitern bedanken. Neben den bisher be-

reits namentlich erwähnten Personen zeichnen sich dabei vor allem Herr Dr. Christian Papp, Till Cremer, Claudia Kolbeck dadurch aus, dass sie zumindest zeitweise ein Büro mit mir geteilt haben und mich entsprechend intensiver ertragen mussten. Unterstützung habe ich während der Promotion aber nicht nur von Kollegen, sondern auch im privaten Umfeld erfahren. Daher sei an dieser Stelle auch meinen Eltern und meinem Bruder, sowie insbesondere Regine Streber gedankt. Darüber haben insbesondere Ole Lytken (Fotografie), Hans-Jörg Drescher (Filmabende), Hans-Peter Bäuml (Fußball) und die Mitglieder des TTC Neunkirchen (Tischtennis) freundlicherweise dafür gesorgt, dass ich ausreichend Abwechslung von der Arbeit bekommen habe.

List of Figures

1.1	TPD spectra of oxygen on Au(110)-(1 × 2)	7
1.2	Potential energy curves for activated and non-activated desorption . .	9
1.3	Simplified sketch of the apparatus used by Kisliuk	15
1.4	Schematic sketch of a Beeck-type calorimeter	16
1.5	Wedler's calorimeter	18
1.6	Adsorption calorimeter for polycrystalline films	19
1.7	Schematics of the single crystal adsorption calorimeter by Kyser . . .	21
1.8	Single-crystal adsorption calorimeter by King	22
1.9	Schematic of the micromechanical sensor used by Gerber	23
1.10	Schematic view of the apparatus used by Heiz	24
1.11	Schematic of the Campbell-Calorimeter	25
2.1	Photograph of the calorimetry chamber in Campbell's laboratory . .	27
2.2	Schematic of the detector assembly for the study of adsorption on polymers	28
2.3	Schematic diagram of the Knudsen cell and associated atom beam path and optic elements used for laser calibration of the calorimeter .	30
2.4	Detector response to pulses of lead atoms with and without the BaF ₂ window in the beam path	32
2.5	Graphical summary of the course of a calorimetric experiment	36
2.6	The Scienta SES-200 X-ray photoelectron spectrometer	40
2.7	The Knudsen cell type evaporator used for the deposition of calcium on the polymer	41
2.8	Schematic energy diagram (for a metal) for photoelectron spectroscopy	42
2.9	Schematic diagram of an oxide-covered metal investigated by McCaf- ferty and Wightman	45
2.10	Regioregular poly(3-hexylthiophene-2,5-diyl)	47
2.11	Schematic illustration of the layered structure of rr-P3HT	49
2.12	Examples for already available products making use of rr-P3HT . . .	50

2.13	Structure of the repeat unit of CN-MEH-PPV.	51
2.14	Schematic structure of an OLED along with common choice for the materials.	51
3.1	Top-view schematic diagram of the calorimeter	54
3.2	Several views of the main chamber.	56
3.3	CAD drawing of the molecular beam source optimized for large organic molecules.	57
3.4	Central part of the Erlangen single-crystal adsorption microcalorimeter	61
5.1	Sticking probability of Ca on a P3HT film at 300 K	68
5.2	The relative integrated Ca LEIS peak intensity as a function of Ca coverage on P3HT at a sample temperature of 300 K	69
5.3	The differential heat of adsorption of Ca atoms on a rr-P3HT surface as a function of Ca coverage at 300 K	70
5.4	XP spectra of the S 2p region for different Ca coverages on P3HT . .	72
5.5	C 1s XP spectra of Ca adsorbed on P3HT	74
5.6	Normalized integrated intensities for the S 2p and C 1s signals as a function of Ca coverage	75
5.7	Thickness of the reacted P3HT layer vs Ca coverage	83
6.1	Survey XP spectra of P3HT before and after electron-irradiation . . .	90
6.2	XP Spectra of the sulfur region before and after electron irradiation .	91
6.3	XP spectra of the C 1s region before and after electron-irradiation . .	93
6.4	LEIS measurements of Ca on electron-irradiated and pristine P3HT .	94
6.5	Sticking probability of Ca on for the pristine and electron-irradiated P3HT films at 300 K	95
6.6	Sticking probatility of Ca on pristine and electron irradiated P3HT .	96
6.7	The differential heat of adsorption of Ca atoms on electron-irradiated and pristine rr-P3HT surfaces as a function of Ca coverage at 300 K .	98
6.8	Schematic of the kinetic competition between different reaction pathways for impinging Ca atoms on a P3HT surface	100
7.1	AR-XP S 2p spectra of P3HT and Ca on P3HT at 300 K	106
7.2	AR-XP S 2p spectra of pristine P3HT and Ca on P3HT at 130 K and 300 K	108

7.3	Schematic sketch to illustrate the influence of the morphology on the expected damping of the substrate signal	110
7.4	Relative LEIS Ca intensity as a function of dose for Ca deposition on Au and P3HT at 130 K and 300 K	111
7.5	AR-XP spectra of the Ca 2p region at 130 K and 300 K on P3HT . .	112
8.1	Ca LEIS intensity as a function of coverage for Ca deposition on CN-MEH-PPV at 130 K and 300 K	116
8.2	Heat of adsorption as a function of Ca coverage for Ca deposition on CN-MEH-PPV at 130 K and 300 K	117
8.3	Sticking probability for Ca deposition on CN-MEH-PPV at 130 K and 300 K	120
8.4	XP spectra of the O 1s spectra recorded after incremental doses of Ca onto CN-MEH-PPV at 300 K.	122

Bibliography

- [1] Forrest, S. R. Ultrathin organic films grown by organic molecular beam deposition and related techniques. *Chemical Reviews*, **1997**, *97*(6), 1793.
- [2] Kowarik, S.; Gerlach, A.; Schreiber, F. Organic molecular beam deposition: Fundamentals, growth dynamics, and in situ studies. *Journal of Physics Condensed Matter*, **2008**, *20*(18).
- [3] Witte, G.; Wöll, C. Growth of aromatic molecules on solid substrates for applications in organic electronics. *Journal of Materials Research*, **2004**, *19*(7), 1889.
- [4] Klauk, H. *Organic Electronics*. Wiley-VCH, Weinheim, 1 edition, 2006.
- [5] Schwalb, C. H.; Sachs, S.; Marks, M.; Schöll, A.; Reinert, F.; Umbach, E.; Höfer, U. Electron lifetime in a Shockley-type metal-organic interface state. *Physical Review Letters*, **2008**, *101*(14).
- [6] Černý, S. Adsorption microcalorimetry in surface science studies: Sixty years of its development into a modern powerful method. *Surface Science Reports*, **1996**, *26*(1-2), 1.
- [7] Somorjai, G. A. *Chemistry in Two Dimensions: Surfaces*. Cornell University Press, Ithaca, NY, 1981.
- [8] Somorjai, G. A. *Introduction to Surface Chemistry and Catalysis*. Wiley, New York, 1994.
- [9] Ertl, G. *The Nature of the Surface Chemical Bond*. North Holland, Amsterdam, 1979.
- [10] Černý, S. *The Chemical Physics of Solid Surfaces and Heterogeneous Catalysis*, volume 2. Elsevier, Amsterdam, 1983.
- [11] Stuckless, J. T.; Al-Sarraf, N.; Wartnaby, C.; King, D. A. Calorimetric heats of adsorption for CO on nickel single crystal surfaces. *Journal of Chemical Physics*, **1993**, *99*(3), 2202.
- [12] Knor, Z. *Catalysis: Science and Technology*, volume 3. Springer, Berlin, 1982.
- [13] Knor, Z. *Surface and Defect Properties of Solids*, volume 6. Chemical Society, London, 1977.
- [14] Stuckless, J. T.; Frei, N. A.; Campbell, C. T. A novel single-crystal adsorption calorimeter and additions for determining metal adsorption and adhesion energies. *Review of Scientific Instruments*, **1998**, *69*(6), 2427.

-
- [15] Langmuir, I. The evaporation, condensation and reflection of molecules and the mechanism of adsorption. *Physical Review*, **1916**, 8(2), 149.
- [16] Petermann, L. A. Thermal desorption kinetics of chemisorbed gases. *Progress in Surface Science*, **1972**, 3(PART 1), 1.
- [17] King, D. A. Thermal desorption from metal surfaces: A review. *Surface Science*, **1975**, 47(1), 384.
- [18] Menzel, D. *Chemistry and Physics of Solid Surfaces*, volume 4. Springer, Berlin, 1982.
- [19] Woodruff, D. P.; Delchar, T. A. *Modern Techniques in Surface Science*. Cambridge University Press, Cambridge, 1986.
- [20] Kreuzer, H. J.; Payne, S. H. *Dynamics of Gas-Surface Reactions*. Cambridge, 1991.
- [21] Christmann, K. *Introduction to Surface Physical Chemistry*. Springer, New York, 1991.
- [22] Gottfried, J. M.; Schmidt, K. J.; Schroeder, S. L. M.; Christmann, K. Oxygen chemisorption on Au(1 1 0)-(1 x 2) I. Thermal desorption measurements. *Surface Science*, **2003**, 525(1-3), 184.
- [23] Hickmott, T. W.; Ehrlich, G. Structure-sensitive chemisorption: The mechanism of desorption from tungsten. *Journal of Physics and Chemistry of Solids*, **1958**, 5(1-2), 47.
- [24] de Jong, A. M.; Niemantsverdriet, J. W. Thermal desorption analysis: Comparative test of ten commonly applied procedures. *Surface Science*, **1990**, 233(3), 355.
- [25] Redhead, P. A. Thermal desorption of gases. *Vacuum*, **1962**, 12(4), 203.
- [26] Wedler, G. *Lehrbuch der Physikalischen Chemie*. Wiley, Weinheim, 5 edition, 2004.
- [27] Gottfried, J. M. *CO Oxidation over Gold*. Dissertation, FU Berlin, 2004.
- [28] Laidler, K. J. *The world of physical chemistry*. Oxford University Press, Oxford, 1993.
- [29] Stuck, A.; Wartnaby, C. E.; Yeo, Y. Y.; Stuckless, J. T.; Al-Sarraf, N.; King, D. A. An improved single crystal adsorption calorimeter. *Surface Science*, **1996**, 349(2), 229.
- [30] Borroni-Bird, C. E.; King, D. A. An ultrahigh vacuum single crystal adsorption microcalorimeter. *Review of Scientific Instruments*, **1991**, 62(9), 2177.
- [31] Dixon-Warren, S. J.; Kovář, M.; Wartnaby, C. E.; King, D. A. Pyroelectric single crystal adsorption microcalorimetry at low temperatures: oxygen on Ni100. *Surface Science*, **1994**, 307-309(PART A), 16.

- [32] Stuckless, J. T.; Wartnaby, C. E.; Al-Sarraf, N.; Dixon-Warren, S. J. B.; Kovář, M.; King, D. A. Oxygen chemisorption and oxide film growth on Ni100, 110, and 111: Sticking probabilities and microcalorimetric adsorption heats. *Journal of Chemical Physics*, **1997**, *106*(5), 2012.
- [33] Roberts, J. K. The Adsorption of Hydrogen on Tungsten. *Proceedings of the Royal Society London A*, **1935**, *152*, 445–463.
- [34] Roberts, J. K. Some Properties of Adsorbed Films of Oxygen on Tungsten. *Proceedings of the Royal Society London A*, **1935**, *152*, 464–477.
- [35] Roberts, J. K. The Exchange of Energy between Gas Atoms and Solid Surfaces. *Proceedings of the Royal Society London A*, **1930**, *129*, 146–161.
- [36] Kisliuk, P. Calorimetric heat of adsorption-nitrogen on tungsten. *The Journal of Chemical Physics*, **1959**, *31*(6), 1605.
- [37] Roberts, J. K.; Whipp, B. The heat of adsorption of hydrogen on tungsten. *Mathematical Proceedings of the Cambridge Philosophical Society*, **1934**, *30*, 376–379.
- [38] Eley, D. D.; Norton, P. R. Heats of Adsorption on Metal Wires. I. Hydrogen on Polycrystalline Tungsten. *Proceedings of the Royal Society London A*, **1970**, *314*, 301–318.
- [39] Couper, A.; John, C. S. Interaction of diatomic molecules with clean metal wire surfaces. Part 2. - Nitrogen on tungsten. *Journal of the Chemical Society, Faraday Transactions 1: Physical Chemistry in Condensed Phases*, **1977**, *73*, 961.
- [40] Couper, A.; John, C. S. Interaction of diatomic molecules with clean metal wire surfaces. Part 1. - Hydrogen on tungsten. *Journal of the Chemical Society, Faraday Transactions 1: Physical Chemistry in Condensed Phases*, **1977**, *73*, 950.
- [41] Yamazaki, H.; Takeo, O.; Ichiro, K. Calorimetric Heats of Chemisorption of Nitrogen on Tungsten at Higher Temperatures. *Japanes Journal of Applied Physics*, **1971**, *10*, 1105–1105.
- [42] Brown, W. A.; Kose, R.; King, D. A. Femtomole adsorption calorimetry on single-crystal surfaces. *Chemical Reviews*, **1998**, *98*(2), 797.
- [43] Leypunski, O. I. *Acta Physicochimica URSS*, **1935**, *2*, 737.
- [44] Leypunski, O. I. *Acta Physicochimica URSS*, **1936**, *5*, 271.
- [45] de Boer, J. H.; Kraak, H. H. *Recueil des Travaux Chimiques des Pays-Bas*, **1936**, *55*, 941.
- [46] Beeck, O.; Smith, A. E.; Wheeler, A. Catalytic Activity, Crystal Structure and Adsorptive Properties of Evaporated Metal Films. *Proceedings of the Royal Society London A*, **1940**, *177*, 62–90.
- [47] Beeck, O. Catalysis-A challenge to the physicist (As exemplified by the hydrogenation of ethylene over metal catalysts). *Reviews of Modern Physics*, **1945**, *17*(1), 61.

- [48] Wedler, G.; Bröcker, F. J. Die Adsorptionswärme des Wasserstoffs an Nickelfilmen bei 77 K und 273 K und ihr Bezug zu anderen Adsorptionseffekten. *Surface Science*, **1971**, *26*(2), 454.
- [49] Wedler, G.; Fisch, G. The Adsorption States of Hydrogen on Polycrystalline Nickel Surfaces at Different Temperatures. *Berichte der Bunsengesellschaft für Physikalische Chemie*, **1972**, *76*, 1160–1163.
- [50] Wedler, G.; Papp, H.; Schroll, G. Adsorption of carbon monoxide on polycrystalline nickel films. *Surface Science*, **1974**, *44*(2), 463.
- [51] Wedler, G.; Geuss, K. P.; Colb, K. G.; McElhiney, G. Heats of adsorption of hydrogen on polycrystalline iron films. *Applications of Surface Science*, **1978**, *1*(4), 471.
- [52] Wedler, G.; Colb, K. G.; McElhiney, G.; Heinrich, W. An investigation of the interaction of CO with polycrystalline iron films. *Applications of Surface Science*, **1978**, *2*(1), 30.
- [53] Wedler, G.; Colb, K. G.; McElhiney, G.; Heinrich, W. The interaction of hydrogen and carbon monoxide on polycrystalline iron films. *Applications of Surface Science*, **1978**, *2*, 85.
- [54] Brennan, D.; Hayes, F. H. Heat of adsorption of hydrogen on evaporated films of tungsten and of nickel. *Transactions of the Faraday Society*, **1964**, *60*, 589.
- [55] Ehrlich, G.; Hayward, D. O.; Černý, S.; Roberts, M. W.; Wedler, G.; King, D. A.; Brennan, D.; Sachtler, W. M. H.; Roginskii, S. Z.; Holscher, A. A.; Wells, B. R.; Geus, J. W.; Frennet, A.; Ponec, V.; Müller, J.; Haul, R. A. W.; Sing, K. S. W. *Discussions of the Faraday Society*, **1966**, *41*, 102–120.
- [56] Wahba, M.; Kemball, C. Heats of Adsorption of Ammonia and Hydrogen on Metal Films. *Transactions of the Faraday Society*, **1953**, *49*, 1351–1360.
- [57] Brennan, D.; Hayward, D. O.; Trapnell, B. M. W. The Calorimetric Determination of the Heats of Adsorption of Oxygen on Evaporated Metal Films. *Proceedings of the Royal Society London A*, **1960**, *256*, 81–105.
- [58] Wedler, G.; Strothenk, H. Kalorimetrische Messung der differentiellen Chemisorptionswärmen von Wasserstoff an Titanfilmen bei 77 K. *Berichte der Bunsengesellschaft für Physikalische Chemie*, **1966**, *70*, 214–220.
- [59] Zommer, L.; Duś, R.; Randzio, S. L. A modified adsorption microcalorimeter with computerized collection and reduction of the data. *Applied Surface Science*, **1990**, *45*(2), 93.
- [60] Klemperer, D. F.; Stone, F. S. Heats of Adsorption on Evaporated Nickel Films. *Proceedings of the Royal Society London A*, **1958**, *243*, 375–399.
- [61] Wedler, G. Elektronische Wechselwirkung und Adsorptionswärme bei der Chemisorption von Gasen an aufgedampften Metallfilmen I. Adiabatisches Kalorimeter zur gleichzeitigen Messung von Adsorptionswärme und Filmwiderstand. *Zeitschrift für Physikalische Chemie*, **1960**, *24*, 73–86.

- [62] Bröcker, F. J.; Wedler, G. Calorimetric Studies of the Chemisorption and Desorption of Hydrogen on Nickel Films under Ultra High Vacuum Conditions. *Discussions of the Faraday Society*, **1966**, *41*, 87–94.
- [63] Černý, S.; Ponec, V.; Hládek, L. Calorimetric heats of adsorption of hydrogen on molybdenum films. *Journal of Catalysis*, **1966**, *5*(1), 27.
- [64] Hládek, L. A self-balancing and recording a.c. bridge for a Beeck-type adsorption calorimeter. *Journal of Scientific Instruments*, **1965**, *42*(4), 198.
- [65] Beeck, O.; Cole, W. A.; Wheeler, A. Determination of heats of adsorption using metal films. *Discussions of the Faraday Society*, **1950**, *8*, 314.
- [66] Brennan, D.; Hayes, F. H. The Adsorption of Carbon Monoxide on Evaporated Metal Films. *Philosophical Transactions of the Royal Society A*, **1965**, *258*, 347–373.
- [67] Wedler, G.; Bröcker, F. J.; Fisch, G.; Schroll, G. Vergleich der Adsorptionswärme von Wasserstoff und Deuterium an Nickelfilmen. *Zeitschrift für Physikalische Chemie N.F.*, **1971**, *76*, 212–215.
- [68] Ganzmann, I.; Kiessling, W.; Borgmann, D.; Wedler, G. Coadsorption of CO and O₂ on Fe(111). III. Thermal desorption spectroscopy, comparison with adsorption on Fe films and heats of adsorption. *Surface Science*, **1992**, *269-270*(C), 347.
- [69] Wedler, G.; Ganzmann, I.; Borgmann, D. *Berichte der Bunsengesellschaft für Physikalische Chemie*, **1993**, *97*, 293.
- [70] Borgmann, D.; Behner, H.; Pirner, M.; Wedler, G. Adsorption, decomposition, and reaction of acetylene on evaporated iron films. *Langmuir*, **1986**, *2*(3), 261.
- [71] Carley, A. F.; Rassias, S.; Roberts, M. W.; Tang-Han, W. A study of the interaction of nitric oxide with nickel and oxidized nickel surfaces by X-Ray photoelectron spectroscopy. *Journal of Catalysis*, **1979**, *60*(3), 385.
- [72] Johnson, D. W.; Roberts, M. W. Nitrogen chemisorption by iron. *Surface Science*, **1979**, *87*(1), L255.
- [73] Matloob, M. H.; Roberts, M. W. Electron spectroscopic study of nitrogen species adsorbed on copper. *Journal of the Chemical Society, Faraday Transactions 1: Physical Chemistry in Condensed Phases*, **1977**, *73*, 1393.
- [74] Kishi, K.; Roberts, M. W. Adsorption of nitrogen and ammonia by polycrystalline iron surfaces in the temperature range 80-290 K studied by electron spectroscopy. *Surface Science*, **1977**, *62*(1), 252.
- [75] Atkinson, S. J.; Brundle, C. R.; Roberts, M. W. ESCA studies of chemisorption on metals: Carbon monoxide on molybdenum and tungsten films. *Journal of Electron Spectroscopy and Related Phenomena*, **1973**, *2*(1), 105.
- [76] Černý, S.; Ponec, V. Determination of Heat of Adsorption on Clean Solid Surfaces. *Catalysis Reviews: Science and Engineering*, **1968**, *2*(1), 249–322.

- [77] Pluntke, C.; Wedler, G.; Rau, G. Study of consecutive processes by means of adsorption calorimetry. *Surface Science*, **1983**, *134*(1), 145.
- [78] Smutek, M.; Černý, S. *Collection of Czechoslovak Chemical Communications*, **1979**, *44*, 3425.
- [79] Wedler, G. Elektronische Wechselwirkung und Adsorptionswärme bei der Chemisorption von Gasen an aufgedampften Metallfilmen II. Einwirkung von Sauerstoff auf Eisenfilme bei 273 K. *Zeitschrift für Physikalische Chemie*, **1961**, *27*, 388–401.
- [80] Wedler, G.; Strothenk, H. Elektrische und kalorimetrische Messungen am System Titan/Wasserstoff bei 273 K. *Zeitschrift für Physikalische Chemie*, **1966**, *48*, 86–101.
- [81] Wedler, G.; Schroll, G. Differentielle Adsorptionswärmen im System Nickel/Kohlenmonoxid bei 273 K. *Zeitschrift für Physikalische Chemie*, **1973**, *85*, 216.
- [82] Wedler, G.; Papp, H.; Schroll, G. The interaction of hydrogen and carbon monoxide on polycrystalline nickel films at temperatures up to 353 K. *Journal of Catalysis*, **1975**, *38*(1-3), 153.
- [83] Wedler, G.; Borgmann, D.; Geuss, K. P. The adsorption states of nitrogen on polycrystalline iron films. *Surface Science*, **1975**, *47*(2), 592.
- [84] Kovář, M.; Dvořák, L.; Černý, S. Application of pyroelectric properties of LiTaO₃ single crystal to microcalorimetric measurement of the heat of adsorption. *Applied Surface Science*, **1994**, *74*(1), 51.
- [85] Dvořák, L.; Kovář, M.; Černý, S. A new approach to adsorption microcalorimetry based on a LiTaO₃ pyroelectric temperature sensor and a pulsed molecular beam. *Thermochimica Acta*, **1994**, *245*(C), 163.
- [86] Černý, S.; Smutek, M.; Buzek, F. Calorimetric studies of hydrocarbon adsorption on metal films. II. Ethylene, acetylene, propylene, methylacetylene and allene on molybdenum. *Journal of Catalysis*, **1977**, *47*(2), 166.
- [87] Pálfi, S.; Lisowski, W.; Smutek, M.; Černý, S. Calorimetric studies of hydrocarbon adsorption on metal films. V. Hydrocarbons on platinum. *Journal of Catalysis*, **1984**, *88*(2), 300.
- [88] Smutek, M.; Černý, S. Calorimetric studies of hydrocarbon adsorption on metal films. III. Methane, ethane and propane on molybdenum. *Journal of Catalysis*, **1977**, *47*(2), 178.
- [89] Smutek, M.; Černý, S. Calorimetric measurements in the Gd / H₂ system at room temperature. *Thermochimica Acta*, **1985**, *91*(C), 31.
- [90] Černý, S.; Kovář, M. *Collection of Czechoslovak Chemical Communications*, **1988**, *53*, 2412.

- [91] Černý, S.; Smutek, M. Calorimetric measurement of the interaction of propylene, acetylene, and methane with dysprosium films at room temperature. *Journal of Catalysis*, **1990**, *123*(1), 275.
- [92] Bastl, Z.; Černý, S.; Dubský, J. *Studies in Surface Science and Catalysis*, volume 40. Elsevier, Amsterdam, 1987.
- [93] Bastl, Z.; Černý, S.; Kovář, M. Calorimetric and XPS study of the effect of copper on the sorption properties of dysprosium. *Applied Surface Science*, **1993**, *68*(2), 275.
- [94] Bastl, Z.; Černý, S. X-ray photoelectron spectroscopy study of the interaction of carbon monoxide and propylene with dysprosium and yttrium surfaces. *Journal of Alloys and Compounds*, **1991**, *176*(1), 159.
- [95] Bastl, Z.; Černý, S.; Dubský, J. *Communications of the Department of Chemistry of the Bulgarian Academy of Science*, **1989**, *22*, 402.
- [96] Kyser, D. A.; Masel, R. I. Design of a calorimeter capable of measuring heats of adsorption on single-crystal surfaces. *Review of Scientific Instruments*, **1987**, *58*(11), 2141.
- [97] Kyser, D. A.; Masel, R. I. Development of single-crystal adsorption calorimetry. *Journal of Vacuum Science and Technology A*, **1986**, *4*(3), 1431–1432.
- [98] Besenbacher, F.; Stensgaard, I.; Mortensen, K. Adsorption position of deuterium on the Pd(100) surface determined with transmission channeling. *Surface Science*, **1987**, *191*(1-2), 288.
- [99] Stensgaard, I.; Jakobsen, F. Adsorption-site location by transmission channeling: Deuterium on Ni(100). *Physical Review Letters*, **1985**, *54*(7), 711.
- [100] Vattuone, L.; Yeo, Y. Y.; King, D. A. Adatom bond energies and lateral interaction energies from calorimetry: NO, O₂, and N₂ adsorption on Ni100. *Journal of Chemical Physics*, **1996**, *104*(20), 8096–8102.
- [101] Wartnaby, C. E.; Stuck, A.; Yee, Y. Y.; King, D. A. Microcalorimetric heats of adsorption for CO, NO, and oxygen on Pt110. *Journal of Physical Chemistry*, **1996**, *100*(30), 12483–12488.
- [102] Wartnaby, C. E.; Stuck, A.; Yeo, Y. Y.; King, D. A. Calorimetric Measurement of Catalytic Surface-Reaction Heat - CO Oxidation on Pt(110). *Journal of Chemical Physics*, **1995**, *102*(4), 1855–1858.
- [103] Yeo, Y. Y.; Stuck, A.; Wartnaby, C. E.; King, D. A. Microcalorimetric study of ethylene adsorption on the Pt111 surface. *Chemical Physics Letters*, **1996**, *259*(1-2), 28–36.
- [104] Yeo, Y. Y.; Vattuone, L.; King, D. A. Energetics and kinetics of CO and NO adsorption on Pt100: Restructuring and lateral interactions. *Journal of Chemical Physics*, **1996**, *104*(10), 3810–3821.

- [105] Gimzewski, J. K.; Gerber, C.; Meyer, E.; Schlittler, R. R. Observation of a chemical reaction using a micromechanical sensor. *Chemical Physics Letters*, **1994**, *217*(5-6), 589.
- [106] Barnes, J. R.; Stephenson, R. J.; Welland, M. E.; Gerber, C.; Gimzewski, J. K. Photothermal spectroscopy with femtojoule sensitivity using a micromechanical device. *Nature*, **1994**, *372*(6501), 79.
- [107] Barnes, J. R.; Stephenson, R. J.; Woodburn, C. N.; O'Shea, S. J.; Welland, M. E.; Rayment, T.; Gimzewski, J. K.; Gerber, C. A femtojoule calorimeter using micromechanical sensors. *Review of Scientific Instruments*, **1994**, *65*(12), 3793.
- [108] Antonietti, J. M.; Gong, J.; Habibpour, V.; Rottgen, M. A.; Abbet, S.; Harding, C. J.; Arenz, M.; Heiz, U.; Gerber, C. Micromechanical sensor for studying heats of surface reactions, adsorption, and cluster deposition processes. *Review of Scientific Instruments*, **2007**, *78*(5), 054101.
- [109] Ihm, H.; Ajo, H. M.; Gottfried, J. M.; Bera, P.; Campbell, C. T. Calorimetric measurement of the heat of adsorption of benzene on Pt(111). *Journal of Physical Chemistry B*, **2004**, *108*(38), 14627.
- [110] Farmer, J. A.; Campbell, C. T.; Xu, L.; Henkelman, G. Defect sites and their distributions on MgO(100) by Li and Ca adsorption calorimetry. *Journal of the American Chemical Society*, **2009**, *131*(8), 3098.
- [111] Campbell, C. T.; Starr, D. E. Metal adsorption and adhesion energies on MgO(100). *Journal of the American Chemical Society*, **2002**, *124*(31), 9212.
- [112] Lytken, O.; Lew, W.; Campbell, C. T. Catalytic reaction energetics by single crystal adsorption calorimetry: Hydrocarbons on Pt(111). *Chemical Society Reviews*, **2008**, *37*(10), 2172.
- [113] Lytken, O.; Lew, W.; Harris, J. J. W.; Vestergaard, E. K.; Gottfried, J. M.; Campbell, C. T. Energetics of cyclohexene adsorption and reaction on Pt(111) by low-temperature microcalorimetry. *Journal of the American Chemical Society*, **2008**, *130*(31), 10247.
- [114] Gottfried, J. M.; Vestergaard, E. K.; Bera, P.; Campbell, C. T. Heat of adsorption of naphthalene on Pt(111) measured by adsorption calorimetry. *Journal of Physical Chemistry B*, **2006**, *110*(35), 17539.
- [115] Zhu, J.; Bebensee, F.; Hieringer, W.; Zhao, W.; Baricuatro, J. H.; Farmer, J. A.; Bai, Y.; Steinrück, H. P.; Gottfried, J. M.; Campbell, C. T. Formation of the calcium/poly(3-hexylthiophene) interface: Structure and energetics. *Journal of the American Chemical Society*, **2009**, *131*(37), 13498.
- [116] Diaz, S. F.; Zhu, J. F.; Harris, J. J. W.; Goetsch, P.; Merte, L. R.; Campbell, C. T. Heats of adsorption of Pb on pristine and electron-irradiated poly(methyl methacrylate) by microcalorimetry. *Surface Science*, **2005**, *598*(1-3), 22.

- [117] King, D. A.; Wells, M. G. Molecular beam investigation of adsorption kinetics on bulk metal targets: Nitrogen on tungsten. *Surface Science*, **1972**, *29*(2), 454.
- [118] Comsa, G.; David, R. Dynamical parameters of desorbing molecules. *Surface Science Reports*, **1985**, *5*(4), 145.
- [119] Pauls, S. W.; Campbell, C. T. Magic-angle thermal desorption mass spectroscopy. *Surface Science*, **1990**, *226*(3), 250.
- [120] Zhu, J.; Goetsch, P.; Ruzycki, N.; Campbell, C. T. Adsorption energy, growth mode, and sticking probability of Ca on poly(methyl methacrylate) surfaces with and without electron damage. *Journal of the American Chemical Society*, **2007**, *129*(20), 6432.
- [121] Zhu, J.; Farmer, J. A.; Ruzycki, N.; Xu, L.; Campbell, C. T.; Henkelman, G. Calcium adsorption on MgO(100): Energetics, structure, and role of defects. *Journal of the American Chemical Society*, **2008**, *130*(7), 2314.
- [122] Henzler, M.; Göpel, W. *Oberflächenphysik des Festkörpers*. Teubner Verlag, Stuttgart, 2. edition, 1994.
- [123] Ertl, G.; Küppers, J. *Low energy electrons and surface chemistry*. VCH, Weinheim, Federal Republic of Germany; Deerfield Beach, FL, USA, 2nd, completely rev. edition, 1985.
- [124] McCafferty, E.; Wightman, J. P. Determination of the concentration of surface hydroxyl groups on metal oxide films by a quantitative XPS method. *Surface and Interface Analysis*, **1998**, *26*(8), 549.
- [125] Strohmeier, B. R. ESCA method for determining the oxide thickness on aluminum alloys. *Surface and Interface Analysis*, **1990**, *15*(1), 51.
- [126] Patil, A. O.; Heeger, A. J.; Wudl, F. Optical properties of conducting polymers. *Chemical Reviews*, **1988**, *88*(1), 183.
- [127] Roncali, J. Conjugated poly(thiophenes): Synthesis, functionalization, and applications. *Chemical Reviews*, **1992**, *92*(4), 711.
- [128] Chen, T. A.; Wu, X.; Rieke, R. D. Regiocontrolled synthesis of poly(3-alkylthiophenes) mediated by Rieke zinc: Their characterization and solid-state properties. *Journal of the American Chemical Society*, **1995**, *117*(1), 233.
- [129] Sato, M. A.; Tanaka, S.; Kaeriyama, K. Soluble conducting polythiophenes. *Journal of the Chemical Society, Chemical Communications*, **1986**, (11), 873.
- [130] Österholm, J. E.; Laakso, J.; Nyholm, P.; Isotalo, H.; Stubb, H.; Inganäs, O.; Salaneck, W. R. Melt and solution processable poly(3-alkylthiophenes) and their blends. *Synthetic Metals*, **1989**, *28*(1-2), 435.
- [131] Yoshino, K.; Nakajima, S.; Onoda, M.; Sugimoto, R. Electrical and optical properties of poly(3-alkylthiophene). *Synthetic Metals*, **1989**, *28*(1-2), 349.

-
- [132] Jen, K. Y.; Miller, G. G.; Elsenbaumer, R. L. Highly conducting, soluble, and environmentally-stable poly(3-alkylthiophenes). *Journal of the Chemical Society, Chemical Communications*, **1986**, (17), 1346.
- [133] Elsenbaumer, R. L.; Jen, K. Y.; Oboodi, R. Processible and environmentally stable conducting polymers. *Synthetic Metals*, **1986**, 15(2-3), 169.
- [134] Jenekhe, S. A. A class of narrow-band-gap semiconducting polymers. *Nature*, **1986**, 322(6077), 345.
- [135] Chung, T. C.; Kaufman, J. H.; Heeger, A. J.; Wudl, F. Charge storage in doped poly(thiophene): Optical and electrochemical studies. *Physical Review B*, **1984**, 30(2), 702.
- [136] McCullough, R. D. The chemistry of conducting polythiophenes. *Advanced Materials*, **1998**, 10(2), 93.
- [137] Cheng, H. L.; Lin, J. W.; Jang, M. F.; Wu, F. C.; Chou, W. Y.; Chang, M. H.; Chao, C. H. Long-term operations of polymeric thin-film transistors: Electricfield-induced intrachain order and charge transport enhancements of conjugated poly(3-hexylthiophene). *Macromolecules*, **2009**, 42(21), 8251.
- [138] Hugger, S.; Thomann, R.; Heinzl, T.; Thurn-Albrecht, T. Semicrystalline morphology in thin films of poly(3-hexylthiophene). *Colloid and Polymer Science*, **2004**, 282(8), 932.
- [139] Surin, M.; Leclère, P.; Lazzaroni, R.; Yuen, J. D.; Wang, G.; Moses, D.; Heeger, A. J.; Cho, S.; Lee, K. Relationship between the microscopic morphology and the charge transport properties in poly(3-hexylthiophene) field-effect transistors. *Journal of Applied Physics*, **2006**, 100(3).
- [140] Yang, H.; Tae, J. S.; Bao, Z.; Ryu, C. Y. Structural transitions of nanocrystalline domains in regioregular poly(3-hexyl thiophene) thin films. *Journal of Polymer Science, Part B: Polymer Physics*, **2007**, 45(11), 1303.
- [141] Friend, R. H.; Gymer, R. W.; Holmes, A. B.; Burroughes, J. H.; Marks, R. N.; Taliani, C.; Bradley, D. D. C.; Dos Santos, D. A.; Brédas, J. L.; Lögdlund, M.; Salaneck, W. R. Electroluminescence in conjugated polymers. *Nature*, **1999**, 397(6715), 121.
- [142] Cacialli, F.; Marks, R. N.; Friend, R. H.; Zamboni, R.; Taliani, C.; Moratti, S. C.; Holmes, A. B. Electrical and luminescent properties of double-layer oligomeric/polymeric light-emitting diodes. *Synthetic Metals*, **1996**, 76(1-3), 145.
- [143] Baigent, D. R.; Holmes, A. B.; Moratti, S. C.; Friend, R. H. Electroluminescence in conjugated polymers: Excited states in cyano-derivatives of poly(p-phenylenevinylene). *Synthetic Metals*, **1996**, 80(2), 119.
- [144] Baigent, D. R.; May, P. G.; Friend, R. H. Emission characteristics of two-polymer layer electroluminescent devices operating under various duty cycles. *Synthetic Metals*, **1996**, 76(1-3), 149.

- [145] Kraft, A.; Grimsdale, A. C.; Holmes, A. B. Electroluminescent Conjugated Polymers - Seeing Polymers in a New Light. *Angewandte Chemie - International Edition*, **1998**, *37*(4), 402.
- [146] Mitschke, U.; Bäuerle, P. The electroluminescence of organic materials. *Journal of Materials Chemistry*, **2000**, *10*(7), 1471.
- [147] Granström, M.; Petritsch, K.; Arias, A. C.; Lux, A.; Andersson, M. R.; Friend, R. H. Laminated fabrication of polymeric photovoltaic diodes. *Nature*, **1998**, *395*(6699), 257.
- [148] Thompson, B. C.; Kim, Y. G.; McCarley, T. D.; Reynolds, J. R. Soluble narrow band gap and blue propylenedioxythiophene-cyanovinylene polymers as multifunctional materials for photovoltaic and electrochromic applications. *Journal of the American Chemical Society*, **2006**, *128*(39), 12714.
- [149] Li, Y.; Xu, H.; Wu, L.; He, F.; Shen, F.; Liu, L.; Yang, B.; Ma, Y. NMR signal assignment of cis/trans-conformational segments in MEH-CN-PPV. *Journal of Polymer Science, Part B: Polymer Physics*, **2008**, *46*(12), 1105.
- [150] Son, S.; Dodabalapur, A.; Lovinger, A. J.; Galvin, M. E. Luminescence enhancement by the introduction of disorder into poly(p-phenylene vinylene). *Science*, **1995**, *269*(5222), 376.
- [151] Buchner, F.; Flechtner, K.; Bai, Y.; Zillner, E.; Kellner, I.; Steinrück, H. P.; Marbach, H.; Gottfried, J. M. Coordination of iron atoms by tetraphenylporphyrin monolayers and multilayers on Ag(111) and formation of iron-tetraphenylporphyrin. *Journal of Physical Chemistry C*, **2008**, *112*(39), 15458.
- [152] Bai, Y.; Buchner, F.; Wendahl, M. T.; Kellner, I.; Bayer, A.; Steinrück, H. P.; Marbach, H.; Gottfried, J. M. Direct metalation of a phthalocyanine monolayer on Ag(111) with coadsorbed iron atoms. *Journal of Physical Chemistry C*, **2008**, *112*(15), 6087.
- [153] Shubina, T. E.; Marbach, H.; Flechtner, K.; Kretschmann, A.; Jux, N.; Buchner, F.; Steinrück, H. P.; Clark, T.; Gottfried, J. M. Principle and mechanism of direct porphyrin metalation: Joint experimental and theoretical investigation. *Journal of the American Chemical Society*, **2007**, *129*(30), 9476.
- [154] Gottfried, J. M.; Flechtner, K.; Kretschmann, A.; Lukasczyk, T.; Steinrück, H. P. Direct synthesis of a metalloporphyrin complex on a surface. *Journal of the American Chemical Society*, **2006**, *128*(17), 5644.
- [155] Buchner, F.; Seufert, K.; Auwärter, W.; Heim, D.; Barth, J. V.; Flechtner, K.; Gottfried, J. M.; Steinrück, H. P.; Marbach, H. NO-induced reorganization of porphyrin arrays. *ACS Nano*, **2009**, *3*(7), 1789.
- [156] Flechtner, K.; Kretschmann, A.; Steinrück, H. P.; Gottfried, J. M. NO-induced reversible switching of the electronic interaction between a porphyrin-coordinated cobalt ion and a silver surface. *Journal of the American Chemical Society*, **2007**, *129*(40), 12110.

- [157] Thran, A.; Strunskus, T.; Zaporozhchenko, V.; Faupel, F. Evidence of noble metal diffusion in polymers at room temperature and its retardation by a chromium barrier. *Applied Physics Letters*, **2002**, *81*(2), 244–246.
- [158] Bebensee, F.; Zhu, J.; Baricuatro, J. H.; Farmer, J. A.; Bai, Y.; Steinrück, H. P.; Campbell, C. T.; Gottfried, J. M. Interface Formation between Calcium and Electron-Irradiated Poly(3-Hexylthiophene). *Langmuir*, **accepted**.
- [159] Sacher, E.; Pireaux, J.-J.; Kowalczyk, S. P.; of Polymer Chemistry., A. C. S. D. *Metallization of polymers*. American Chemical Society, Washington, D.C, 1990.
- [160] Lachkar, A.; Selmani, A.; Sacher, E. Metallization of polythiophenes II. Interaction of vapor-deposited Cr, V and Ti with poly(3-hexylthiophene) (P3HT). *Synthetic Metals*, **1995**, *72*(1), 73.
- [161] Lachkar, A.; Selmani, A.; Sacher, E.; Leclerc, M.; Mokhliss, R. Metallization of polythiophenes I. Interaction of vapor-deposited Cu, Ag and Au with poly(3-hexylthiophene) (P3HT). *Synthetic Metals*, **1994**, *66*(3), 209.
- [162] Popovici, D.; Piyakis, K.; Meunier, M.; Sacher, E. Angle-resolved x-ray photoelectron spectroscopy comparison of copper/Teflon AF1600 and aluminum/Kapton metal diffusion. *Journal of Applied Physics*, **1998**, *83*(1), 108.
- [163] Tegen, N.; Morton, S. A.; Watts, J. F. Study of poly(ether sulfone)/metal interfaces by high energy x-ray photoelectron spectroscopy and x-ray absorption spectroscopy. *Journal of Vacuum Science and Technology A: Vacuum, Surfaces and Films*, **1997**, *15*(3), 544.
- [164] Koprinarov, I.; Lippitz, A.; Friedrich, J. F.; Unger, W. E. S.; Wöll, C. Surface analysis of DC oxygen plasma treated or chromium evaporated poly(ethylene terephthalate) foils by soft X-ray absorption spectroscopy (NEXAFS). *Polymer*, **1997**, *38*(8), 2005.
- [165] Lippitz, A.; Koprinarov, I.; Friedrich, J. F.; Unger, W. E. S.; Weiss, K.; Wöll, C. Surface analysis of metallized poly(bisphenol A carbonate) films by X-ray absorption spectroscopy (NEXAFS). *Polymer*, **1996**, *37*(14), 3157.
- [166] Pireaux, J. J.; Vermeersch, M.; Grégoire, C.; Thiry, P. A.; Caudano, R.; Clarke, T. C. The aluminum-polyimide interface: An electron-induced vibrational spectroscopy approach. *The Journal of Chemical Physics*, **1988**, *88*(5), 3353.
- [167] Pireaux, J. J.; Thiry, P. A.; Caudano, R.; Pfluger, P. Surface analysis of polyethylene and hexatriacontane by high resolution electron energy loss spectroscopy. *The Journal of Chemical Physics*, **1986**, *84*(11), 6452.
- [168] DiNardo, N. J.; Demuth, J. E.; Clarke, T. C. Electron vibrational spectroscopy of thin polyimide films. *The Journal of Chemical Physics*, **1986**, *85*(11), 6739.
- [169] Sacher, E. *Metallization of Polymers 2*. Kluwer Academic / Plenum Publishers, New York, 2002.

- [170] Strunskus, T.; Zaporojtchenko, V.; Behnke, K.; Von Bechtolsheim, C.; Faupel, F. Tailoring the morphology of metal/polymer interfaces. *Advanced Engineering Materials*, **2000**, *2*(8), 489.
- [171] Léonard, D.; Bertrand, P.; Shi, M. K.; Sacher, E.; Martinu, L. Plasma surface modification of fluoropolymers studied by ToF-SIMS. *Plasmas and Polymers*, **1999**, *4*(2), 97.
- [172] Sandrin, L.; Sacher, E. X-ray photoelectron spectroscopy studies of the evaporated aluminum/corona-treated polyethylene terephthalate interface. *Applied Surface Science*, **1998**, *135*(1-4), 339.
- [173] Popovici, D.; Meunier, M.; Sacher, E. Laser-enhanced gas phase surface modifications of Teflon AF1600 for increased copper adhesion. *Journal of Adhesion*, **1999**, *70*(1), 155.
- [174] Meyer, K.; Schuller, I. K.; Falco, C. M. Thermalization of sputtered atoms. *Journal of Applied Physics*, **1981**, *52*(9), 5803.
- [175] Oechsner, H. Energy distributions in sputtering processes. *Energieverteilungen bei der Festkörperzerstäubung durch Ionenbeschuß*, **1970**, *238*(5), 433.
- [176] Coakley, K. M.; McGehee, M. D. Conjugated polymer photovoltaic cells. *Chemistry of Materials*, **2004**, *16*(23), 4533.
- [177] Garnier, F.; Hajlaoui, R.; Yassar, A.; Srivastava, P. All-polymer field-effect transistor realized by printing techniques. *Science*, **1994**, *265*(5179), 1684.
- [178] Fahlman, M.; Salaneck, W. R. Surfaces and interfaces in polymer-based electronics. *Surface Science*, **2002**, *500*(1-3), 904.
- [179] Salaneck, W. R.; Lögdlund, M.; Fahlman, M.; Greczynski, G.; Kugler, T. *Mater. Sci. Eng.*, **2001**, *34*, 121.
- [180] Reese, M. O.; White, M. S.; Rumbles, G.; Ginley, D. S.; Shaheen, S. E. *Appl. Phys. Lett.*, **2008**, *92*, 053307.
- [181] Reese, M. O.; Morfa, A. J.; White, M. S.; Kopidakis, N.; Shaheen, S. E.; Rumbles, G.; Ginley, D. S. Pathways for the degradation of organic photovoltaic P3HT:PCBM based devices. *Solar Energy Materials and Solar Cells*, **2008**, *92*(7), 746.
- [182] Paci, B.; Generosi, A.; Rossi Albertini, V.; Perfetti, P.; de Bettignies, R.; Sentein, C. Time-resolved morphological study of organic thin film solar cells based on calcium/aluminium cathode material. *Chemical Physics Letters*, **2008**, *461*(1-3), 77.
- [183] Hsieh, S. N.; Kuo, T. Y.; Chong, L. W.; Wen, T. C.; Yang, F. S.; Guo, T. F.; Chung, C. T. *IEEE Photon. Tech. Lett.*, **2009**, *21*, 109.
- [184] Bröms, P.; Birgersson, J.; Johansson, N.; Lögdlund, M.; Salaneck, W. R. Calcium electrodes in polymer LEDs. *Synthetic Metals*, **1995**, *74*(2), 179.

-
- [185] Mikalo, R. P.; Schmeisser, D. Electric contacts on conductive polymers: Sodium on poly(3-hexylthiophene-2,5-diyl). *Synthetic Metals*, **2002**, *127*(1-3), 273.
- [186] Ponjée, M. W. G.; Reijme, M. A.; Langeveld-Voss, B. M. W.; Denier van der Gon, A. W.; Brongersma, H. H. Molecular surface structure of poly(3-hexylthiophene) studied by low energy ion scattering. *Surface Science*, **2002**, *512*(3), 194.
- [187] Gomathi, N.; Neogi, S. Surface modification of polypropylene using argon plasma: Statistical optimization of the process variables. *Applied Surface Science*, **2009**, *255*(17), 7590.
- [188] De Geyter, N.; Morent, R.; Leys, C. Surface characterization of plasma-modified polyethylene by contact angle experiments and ATR-FTIR spectroscopy. *Surface and Interface Analysis*, **2008**, *40*(3-4), 608.
- [189] Kitova, S.; Minchev, M.; Danev, G. Soft plasma treatment of polymer surfaces. *Journal of Optoelectronics and Advanced Materials*, **2005**, *7*(1), 249.
- [190] Tuross, A.; Abdul-Kader, A. M.; Ratajczak, R.; Stonert, A. Modification of UHMWPE by ion, electron and γ -ray irradiation. *Vacuum*, **2009**, *83*(SUPPL.1), S54.
- [191] Massey, S.; Cloutier, P.; Bazin, M.; Sanche, L.; Roy, D. Chemical modification of polystyrene by low-energy (<100 eV) electron irradiation studied by mass spectrometry. *Journal of Applied Polymer Science*, **2008**, *108*(5), 3163.
- [192] Burkert, S.; Kuntzsch, M.; Bellmann, C.; Uhlmann, P.; Stamm, M. Tuning of surface properties of thin polymer films by electron beam treatment. *Applied Surface Science*, **2009**, *255*(12), 6256.
- [193] Mishra, R.; Tripathy, S. P.; Dwivedi, K. K.; Khathing, D. T.; Ghosh, S.; Müller, M.; Fink, D. Effect of electron irradiation on polytetrafluoro ethylene. *Radiation Measurements*, **2003**, *37*(3), 247.
- [194] Zekonyte, J.; Erichsen, J.; Zaporajtchenko, V.; Faupel, F. Mechanisms of argon ion-beam surface modification of polystyrene. *Surface Science*, **2003**, *532-535*, 1040.
- [195] Sahre, K.; Eichhorn, K. J.; Simon, F.; Pleul, D.; Janke, A.; Gerlach, G. Characterization of ion-beam modified polyimide layers. *Surface and Coatings Technology*, **2001**, *139*(2-3), 257.
- [196] Zaporajtchenko, V.; Zekonyte, J.; Faupel, F. Effects of ion beam treatment on atomic and macroscopic adhesion of copper to different polymer materials. *Nuclear Instruments and Methods in Physics Research, Section B: Beam Interactions with Materials and Atoms*, **2007**, *265*(1), 139.
- [197] Bébin, P.; Prud'Homme, R. E. Comparative XPS study of copper, nickel, and aluminum coatings on polymer surfaces. *Chemistry of Materials*, **2003**, *15*(4), 965.
- [198] Smithson, R. L. W.; McClure, D. J.; Evans, D. F. Effects of polymer substrate surface energy on nucleation and growth of evaporated gold films. *Thin Solid Films*, **1997**, *307*(1-2), 110.

- [199] Zaporozhchenko, V.; Zekonyte, J.; Biswas, A.; Faupel, F. Controlled growth of nano-size metal clusters on polymers by using VPD method. *Surface Science*, **2003**, 532-535, 300.
- [200] Lide, D. R. *CRC Handbook of Chemistry and Physics*, **2005**.
- [201] Kisliuk, P. The sticking probabilities of gases chemisorbed on the surfaces of solids. *Journal of Physics and Chemistry of Solids*, **1957**, 3(1-2), 95.
- [202] Andrade, J. D. *Surface and Interfacial Aspects of Biomedical Polymers*, **1985**.
- [203] Ettedgui, E.; Hsieh, B. R.; Gao, Y. Interface formation of metals and poly(p-phenylene vinylene): Surface species and band bending. *Polymers for Advanced Technologies*, **1997**, 8(7), 408.
- [204] Thomson, W. On the equilibrium of vapour at a curved surface of liquid. *Philos. Mag.*, **1871**, 42(2), 448.
- [205] Chase, M. W. J. *J. Phys. Chem. Ref. Data-Monogr.* 9, **1998**, p 1.
- [206] Bharadwaj, R. K.; Boyd, R. H. Small molecule penetrant diffusion in aromatic polyesters: A molecular dynamics simulation study. *Polymer*, **1999**, 40(15), 4229.
- [207] Bahadur, S.; Gong, D.; Anderegg, J. W. Investigation of the influence of CaS, CaO and CaF₂ fillers on the transfer and wear of nylon by microscopy and XPS analysis. *Wear*, **1996**, 197(1-2), 271.
- [208] Franzen, H. F.; Merrick, J.; Umana, M.; Khan, A. S.; Peterson, D. T.; McCreary, J. R.; Thorn, R. J. XPS spectra and crystalline potentials in alkaline-earth chalcogenides and hydrides. *Journal of Electron Spectroscopy and Related Phenomena*, **1977**, 11(4), 439.
- [209] Van Doveren, H.; Verhoeven, J. A. T. H. XPS spectra of Ca, Sr, Ba and their oxides. *Journal of Electron Spectroscopy and Related Phenomena*, **1980**, 21(3), 265.
- [210] Lesiak, B.; Kosinski, A.; Jablonski, A.; Kövér, L.; Tóth, J.; Varga, D.; Cserny, I.; Zagorska, M.; Kulszewicz-Bajer, I.; Gergely, G. Determination of the inelastic mean free path of electrons in polythiophenes using elastic peak electron spectroscopy method. *Applied Surface Science*, **2001**, 174(1), 70.
- [211] Cugola, R.; Giovanella, U.; Di Gianvincenzo, P.; Bertini, F.; Catellani, M.; Luzzati, S. Thermal characterization and annealing effects of polythiophene/fullerene photoactive layers for solar cells. *Thin Solid Films*, **2006**, 511-512, 489.
- [212] Smekal, W.; Werner, W. S. M.; Powell, C. J. Simulation of electron spectra for surface analysis (SESSA): A novel software tool for quantitative Auger-electron spectroscopy and X-ray photoelectron spectroscopy. *Surface and Interface Analysis*, **2005**, 37(11), 1059.
- [213] Werner, W. S. M. Simulation of electron spectra for surface analysis using the partial-intensity approach (PIA). *Surface and Interface Analysis*, **2005**, 37(11), 846.

-
- [214] Murdey, R.; Stuckless, J. T. Calorimetry of polymer metallization: Copper, calcium, and chromium on PMDA-ODA polyimide. *Journal of the American Chemical Society*, **2003**, *125*(13), 3995.
- [215] Campbell, C. T. Ultrathin metal films and particles on oxide surfaces: Structural, electronic and chemisorptive properties. *Surface Science Reports*, **1997**, *27*(1-3), 1.
- [216] Chua, L. L.; Dipankar, M.; Sivaramakrishnan, S.; Gao, X.; Qi, D.; Wee, A. T. S.; Ho, P. K. H. Large damage threshold and small electron escape depth in X-ray absorption spectroscopy of a conjugated polymer thin film. *Langmuir*, **2006**, *22*(20), 8587.
- [217] Ahn, H.; Oblas, D. W.; Whitten, J. E. Electron irradiation of poly(3-hexylthiophene) films. *Macromolecules*, **2004**, *37*(9), 3381.
- [218] Ratcliff, E. L.; Jenkins, J. L.; Nebesny, K.; Armstrong, N. R. Electrodeposited, "textured" poly(3-hexyl-thiophene) (e-P3HT) films for photovoltaic applications. *Chemistry of Materials*, **2008**, *20*(18), 5796.
- [219] Salvati Jr, L.; Hook, T. J.; Gardella Jr, J. A.; Chin, R. L. SURFACE SPECTROSCOPIC STUDIES OF POLY(METHYL METHACRYLATE) (PMMA) AND MODIFIED PMMA SURFACES. *Polymer Engineering and Science*, **1987**, *27*(13), 939.
- [220] Starr, D. E.; Campbell, C. T. Large entropy difference between terrace and step sites on surfaces. *Journal of the American Chemical Society*, **2008**, *130*(23), 7321.
- [221] Demri, B.; HageAli, M.; Moritz, M.; Kahn, J. L.; Muster, D. X-ray photoemission study of the calcium/titanium dioxide interface. *Applied Surface Science*, **1997**, *108*(2), 245–249.
- [222] Sosulnikov, M. I.; Teterin, Y. A. X-ray photoelectron studies of Ca, Sr and Ba and their oxides and carbonates. *Journal of Electron Spectroscopy and Related Phenomena*, **1992**, *59*, 111–126.
- [223] Jing, D. P.; Unal, B.; Qin, F. L.; Yuen, C.; Evans, J. W.; Jenks, C. J.; Sordelet, D. J.; Thiel, P. A. Stranski-Krastanov-like growth of an Ag film on a metallic glass. *Thin Solid Films*, **2009**, *517*(24), 6486–6492.
- [224] Ayyub, P.; Chandra, R.; Taneja, P.; Sharma, A. K.; Pinto, R. Synthesis of nanocrystalline material by sputtering and laser ablation at low temperatures. *Applied Physics A-Materials Science & Processing*, **2001**, *73*(1), 67–73.
- [225] Jiang, X.; Matejicek, J.; Sampath, S. Substrate temperature effects on the splat formation, microstructure development and properties of plasma sprayed coatings Part II: case study for molybdenum. *Materials Science And Engineering A-Structural Materials Properties Microstructure And Processing*, **1999**, *272*(1), 189–198.
- [226] Sampath, S.; Jiang, X. Y.; Matejicek, J.; Leger, A. C.; Vardelle, A. Substrate temperature effects on splat formation, microstructure development and properties of

Bibliography

plasma sprayed coatings Part I: Case study for partially stabilized zirconia. *Materials Science And Engineering A-Structural Materials Properties Microstructure And Processing*, **1999**, 272(1), 181–188.